

Optical diagnostics and modeling of low-temperature laboratory plasmas

Inauguraldissertation

zur

Erlangung des akademischen Grades eines
Doktors der Naturwissenschaften (Dr. rer. nat.)

der

Mathematisch-Naturwissenschaftlichen Fakultät

der

Ernst-Moritz-Arndt-Universität Greifswald

vorgelegt von

Vladimir Sushkov

geboren am 01. Dezember 1978

geboren in Sankt Petersburg, Russland

- Greifswald, 2013 -

Dekan:

Prof. Dr. Klaus Fesser

1. Gutachter:

Prof. Dr. Rainer Hippler

2. Gutachter:

Prof. Dr. Uwe Czarnetzki

Tag der Promotion: 04.04.2014

Das Wahre ist das Ganze. Das Ganze aber ist nur das durch seine Entwicklung sich vollendende Wesen. Es ist von dem Absoluten zu sagen, dass es wesentlich Resultat, dass es erst am Ende das ist, was es in Wahrheit ist; und hierin eben besteht seine Natur, Wirkliches, Subjekt oder Sichselbstwerden zu sein.

Georg Wilhelm Friedrich Hegel

Contents

List of abbreviations	7
1 Introduction	9
1.1 Historical note	9
1.2 Plan of this work	11
2 Methods	13
2.1 Optical methods	13
2.1.1 Preface	13
2.1.2 Escape factor and self-absorption	14
2.2 Aspects and Modeling of laboratory discharges	19
2.2.1 Magnetron	19
2.2.2 RF-discharge	23
3 Results/Publications	25
3.1 Absorption spectroscopy of Pulsed Magnetron Discharge	25
3.1.1 Initial conditions and input parameters	25
3.1.2 Experimental data in view of electronic non-equilibrium	25
3.1.3 Estimation of the electron temperature	28
<i>Article I - Time-resolved tunable diode laser absorption spectroscopy of excited argon and ground-state titanium atoms in pulsed magnetron discharges</i>	<i>30</i>
3.2 Emission spectroscopy of RF discharge	41
<i>Article II - Application of the escape factor method for determination of excited states densities in a low-pressure argon radio-frequency discharge</i>	<i>41</i>
3.3 Fast video recording of a dust particle in a RF sheath	53
3.3.1 Sheath simulations	53
<i>Article III - Behavior of a porous particle in a radiofrequency plasma under pulsed argon ion beam bombardment</i>	<i>55</i>
<i>Article IV - Fourier Analysis of Particle Motion in a Radio Frequency Plasma Under Pulsed Argon Ion Beam Bombardment</i>	<i>75</i>

Bibliography	81
Summary	87
Erklärung	89
Selbständigkeitserklärung	90
Lebenslauf	91
Publications	93
Contributions	95
Acknowledgements	99

List of abbreviations

PMS	Pulsed Magnetron Sputtering
PMD	Pulsed Magnetron Discharge
HiPIMS	High Power Impuls Magnetron Sputtering
HPPIMS	High Power Pulsed Magnetron Sputtering
GEC	Gaseous Electronics Conference
DC	Direct Current
RF	radio frequency
ICP	Inductively Coupled Plasma
CCP	Capacitively Coupled Plasma
TDLAS	Tunable Diode Laser Absorption Spectroscopy
OES	Optical Emission Spectroscopy
EDF	Energy Distribution Function
NEI	Non-Equilibrium of Ionization type
NER	Non-Equilibrium of Recombination type
PIC-MCC	Particle In Cell - Monte Carlo Collisions

Chapter 1

Introduction

1.1 Historical note

Thin film deposition by magnetron sputtering is nowadays a widespread and well-established technique in industrial coating applications. As back long ago as 1930s the properties of the magnetron discharge in cylindrical configuration have been investigated by F M Penning [1] who also proposed to use it for sputtering [2]. Then there was further research of such discharges [3, 4] in 50s and 60s, and in 60s the sputtering application of magnetron discharges comes on stage [5–7]. The magnetic confinement increases the path length of energetic secondary electrons and thereby the number of ionising events by a single electron. This permitted to operate discharges at lower voltages (~ 500 V, instead of kilovolts for conventional dc sputtering discharges [8]) and to reduce the working pressures by an order of magnitude (mTorr-region, instead of 10-100 mTorr typical for unmagnetised discharges [8]), while keeping the deposition rate at acceptable level. Then in 1970s the magnetron sputtering developed rapidly [9, 10], when the *planar* magnetrons [11] and then the *balanced* magnetrons (of planar configuration) have been introduced [12, 13]. The *unbalanced* configuration of the dc planar magnetron was a further major step of the advancement of the technique in 1980s [14–16]. In such devices the outer rings of magnets are strengthened relative to the central pole. By that the electron confinement at the target region is somewhat relaxed and the plasma is extending out to the substrate position. This results in enlarged deposition rate and an additional possibility to control the ion flux to the substrate. The next big advancement was in the beginning of 1990s, when the Pulsed Magnetron Sputtering (PMS) was introduced. The feeding current is pulsed in the mid-frequency range (20-350 kHz [17]) which facilitates the periodic contact between target and plasma electrons. This largely solved the problems associated with arc formation at insulating targets and 'target poisoning' in case of reactive sputtering.

In consequence of these developments a variety of magnetron modifications have become available for the sputter deposition, depending on specification and application. Basically, in many cases it is beneficial to have a high ionisation fraction of the target material coming on to the substrate. It gives better control over the process and improves the film quality. The natural way to increase this fraction is to enhance the

plasma density. The plasma density generally growth with the input target power. But this way of increasing plasma density has its natural limitation because of target melting due to heat load. However, pulsing technique permits to circumvent this hindrance by increasing the peak power while keeping the average power value sufficiently low. This is what the term High Power Pulsed Magnetron Sputtering (HPPIMS) means. In case of very small duty-cycles and proportionally very high peak power the term HiPIMS (High Power Impuls Magnetron Sputtering) is usually used. Some authors tend not to distinguish between this two terms. Further discussion on relation between them can be found in review [18], where HPPIMS is treated as a generic to HiPIMS. The HiPIMS is realized with more or less standard magnetron equipment except for the power supply, which is designed to produce short pulses of power densities up to several kW/cm² at the cathode. Since its emergence in the mid-1990s [19], the HiPIMS have been in focus of intense research. Up to now the considerable understanding of the specific phenomena of discharge physics have been gained. An excellent review paper [18] summerizes the knowledge in the field and describes in details many physical aspects. In our work **Article I** we explain the temporal behavior of certain atomic species in our HiPIMS system by modeling the relevant processes.

Another family of low-pressure discharges, frequently found in industry and in laboratories, is the radio-frequency (rf) discharge. Leaving aside one of the two main types of the rf discharge - the inductively coupled plasma (ICP) - here we go into the the capacitively coupled type (CCP). Similar to magnetrons, the history of CCP rf discharges is also closely connected to sputtering technologies and dates back to the first systematic observations in 1930s [20, 21]. A new stage of research began in the late 40s [22] through 50s [23, 24] as the new advantages in the treatment of insulating materials have been recognized, and by the early 60s there was already a quite advanced knowledge on CCP rf discharges: utilization of frequencies of the order of 10 MHz was shown to be optimal [25] and a quantative understanding of sheath phenomena have been gained [26]. And now these low-pressure discharges found increasingly a widespread application in the semiconductor industry for surface treatment and thin film depostion. The plasma conditions proved to be sensitive to a specific realization of the discharge, and in order to make the results of different research groups comparable, the Gaseous Electronics Conference proposed in 1988 [27] a standartised rf-plasma chamber (GEC-cell). It's also in these years that this type of discharges started to be utilized in the analytical chemistry due to its sputtering action [28]. By the beginning of 90s the fundamentals of rf-specific physics, such as peculiar electron heating mechnisms and sheath dynamics, were more or less completely understood [29], when a new phenomenon came to the focus of research and gave a fresh impetus to application of rf discharges.

The fact is, back in the early 80 s the *Voyager-2* images of the Saturn's rings registered the phenomenon related to the space dusty plasma [31]. In the second half of 80s it emerged that inside the industrial plasma-processing facilities there are forming small dust particles in uncontrolled and undesired manner [32, 33]. And finally, the realization of Coulomb crystals by several research groups in 1994 (for example [34]) triggered off the intensive research in the field related to dusty plasmas. This research assigns the key role to CCP rf discharges, which proved to be a good combination of plasma source

and electrostatic trap due to the rf-sheath. Nowadays the domain of complex plasmas is a well-established field branched out into a wide range of research topics [35]. In our works **Articles III, IV** we consider the behavior of a huge particle in the sheath. The other work **Article II** presents a model for the self-absorption of emitted light, which is used for diagnostics of excited species.

1.2 Plan of this work

The point of the thesis is the linkage of different optical diagnostics with the low-pressure discharges. Such linkage is accomplished by virtue of mathematical and physical models which have been developed as the case may have required. Sometime an optical method had to be put forward, sometime a model for a discharge had to be developed. Hence the structure of the present work. After the present introductory part comes Chapter *Methods*. In its first Section for a start I briefly mention all optical methods involved and then go into some details of one of them - this is the natural completion of the self-absorption diagnostics developed in **Article II**. In the second Section of this Chapter the necessary explanations and additions to the models are given, which were developed for the PMD (pulsed magnetron discharge) and rf-discharges. Then the next *Results/Publications* Chapter contains the results. Because this work is a compilation thesis (eine kumulative Dissertation), the results are mostly represented by the published papers, which in the text are referred to as **Article I, II, etc.**, in total there are 4 articles in this Chapter. Along with the published papers I render also a few further calculations for the sake of completeness of the models, and the PMD experimental data is consistently explained in the perspective of the electronic non-equilibrium.

Chapter 2

Methods

2.1 Optical methods

2.1.1 Preface

Here is only a brief summary of the methods, since all necessary experimental details are given in the corresponding papers and the present work is focused on the interpretation of the data.

The experimental data in this work is based on three types of optical methods:

- *Absorption spectroscopy*
- *Emission spectroscopy*
- *Fast video recording*

The last item - *video recording* - was used for the studies in the field of complex plasmas, while the first two - *absorption* and *emission spectroscopy* - operated within the pristine plasma. The necessary details on modeling of the relevant discharge types are given in Chapter *Results/Publications* and also in Sec.2.2 of the current Chapter. Now we concentrate on the optical methods.

Their advantageous aspect over many other diagnostics (probe diagnostics, mass spectrometry, etc.) is that they are in-situ and nonperturbative at once. This makes them widely-used in general and especially helpful at studying the dynamical objects. Although it is often evident that the object is not disturbed, but some remarks to this point have to be done.

(i) The *absorption spectroscopy* was represented by TDLAS (Tunable Diode-Laser Absorption Spectroscopy) technique. It was done in the well-established arrangement for the time-unresolved measurements [**Article II**] and in a more novel realization for the time-resolved measurements in the PMD [**Article I**]. We checked that it is free from the power saturation effect i.e. the laser intensity was small enough for the measurement to be looked upon as non-disturbing.

(ii) The registration of the emitted light is nonperturbative by its nature. To be precise, when we have light coming out of a plasma chamber - this fact itself has certain effect on the distributions of excited states. In this regard, a plasma chamber with/without optical window is different under otherwise equal conditions. The chamber in work [Article II] was throughout the same. But the article needs to be completed with a few spectroscopic arguments which have been left beyond its scope; they will be articulated now in the coming paragraphs.

(iii) A fast video camera was used to record the movement of a particle [Articles III, IV]. The particle was illuminated by vertically expanded laser sheet and the method is nonperturbative unless the intensity of this laser sheet is strong enough to push off the particle in the direction of light incidence. The time curve of particle position was Fourier-analyzed, but this was not a spectroscopic method in the strict sense, since it didn't employ any wavelength decomposition.

2.1.2 Escape factor and self-absorption

In Article II we describe a spectroscopic method which is based on the self-absorption in the discharge. We apply it for determination of the number densities of $1s$ -states (in Paschen notation) of excited argon atoms. For this purpose, we use many lines from $1s_j - 2p_m$ transition array. Each of those lines was modeled as having simple Doppler-broadened shape. Since it is not as self-evident as it may appear, in this Section I will explore the range of applicability of this assumption and demonstrate that it works good at the conditions of Article II.

First of all, the natural argon consists almost entirely of ^{40}Ar (99.6%), the fractions of ^{36}Ar (0.337%) and ^{38}Ar (0.063%) are small enough to neglect them. Furthermore, since these isotopes are even, they all have nuclear spin $I = 0$. For these reasons we consider argon spectral lines to be free of isotope and hyperfine splitting.

The Doppler-broadening leading to the Gaussian lineshape is by far the most important mechanism at the condition of Article II - the RF-discharge in argon at pressure 2 – 22 Pa and room temperature. But this is not enough to justify the assumption of the pure Gaussian shape. It still may happen that the omission of the other mechanisms gives rise to a significant error. And so, when such *homogeneous* broadening mechanisms like *natural*- and *pressure*-broadening have to be taken into account, the shape of a line is reproduced by the Voigt-profile:

$$k(\nu) = k_0^D \frac{a}{\pi} \int_{-\infty}^{\infty} \frac{\exp(-u^2)}{a^2 + \left[\frac{(\nu - \nu_0)}{\Delta\nu_D} - u \right]^2} du \quad (2.1)$$

where k_0^D is the absorption coefficient associated with pure Doppler-broadening at the central frequency ν_0 . Parameter a stands for the homogeneous mechanisms, giving relative contribution of the Lorenz-broadening $a = \frac{\Delta\nu_L}{2\Delta\nu_D}$, where $\Delta\nu_D$ is the Doppler-width and $\Delta\nu_L = \Delta\nu_n + \Delta\nu_{pr}$ is the sum of the natural and pressure line widths. For

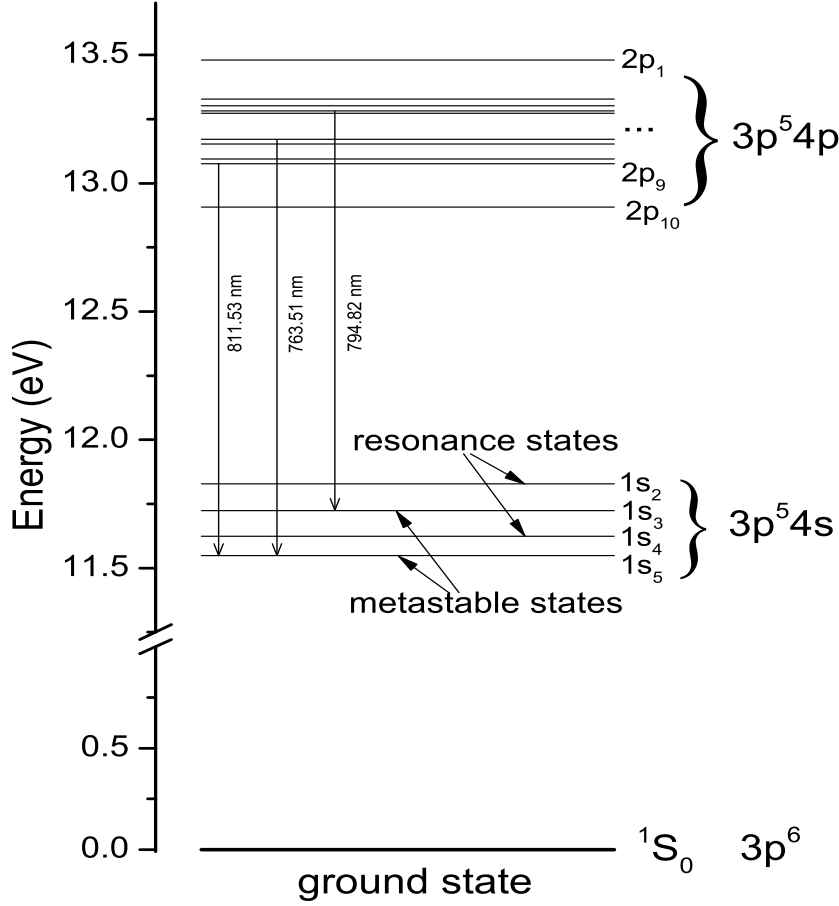


Figure 2.1: The energy scheme shows the ground level and 14 lowest-lying excited levels of argon atom. Also displayed are the transitions discussed in this Section.

convenience we use here

$$\Delta\nu_D = \Delta\nu_D^{FWHM}/2 \ln 2 = \nu_0 \sqrt{\frac{2kT}{mc^2}}. \quad (2.2)$$

The optical cross-section of transition $1s_3 - 2p_4$ ($\lambda_0 = 794.82 \text{ nm}$) is the largest in the whole $1s_j - 2p_m$ array. Yet nevertheless, being the product of the cross-section and the number density of absorbing species, the absorption coefficient is larger for lines which end on $1s_5$ -level, because this state is much more abundant than the other excited states. Transition $1s_5 - 2p_9$ ($\lambda_0 = 811.53 \text{ nm}$) is the strongest among such lines but it was not used in the present study. The strongest of the used ones was $1s_5 - 2p_6$ (763.51 nm). We choose now this line for a small 'case study' and check how the assumption of the pure Doppler profile works.

At $T = 350 \text{ K}$ (the laser-absorption measurements revealed a slight increase in temperature of the excited species) the Doppler-width is $\Delta\nu_D = 5.0 \cdot 10^8 \text{ Hz}$. The natural linewidth of $1s_5 - 2p_6$ transition $\Delta\nu_n$ is evaluated from the lifetimes of these two lev-

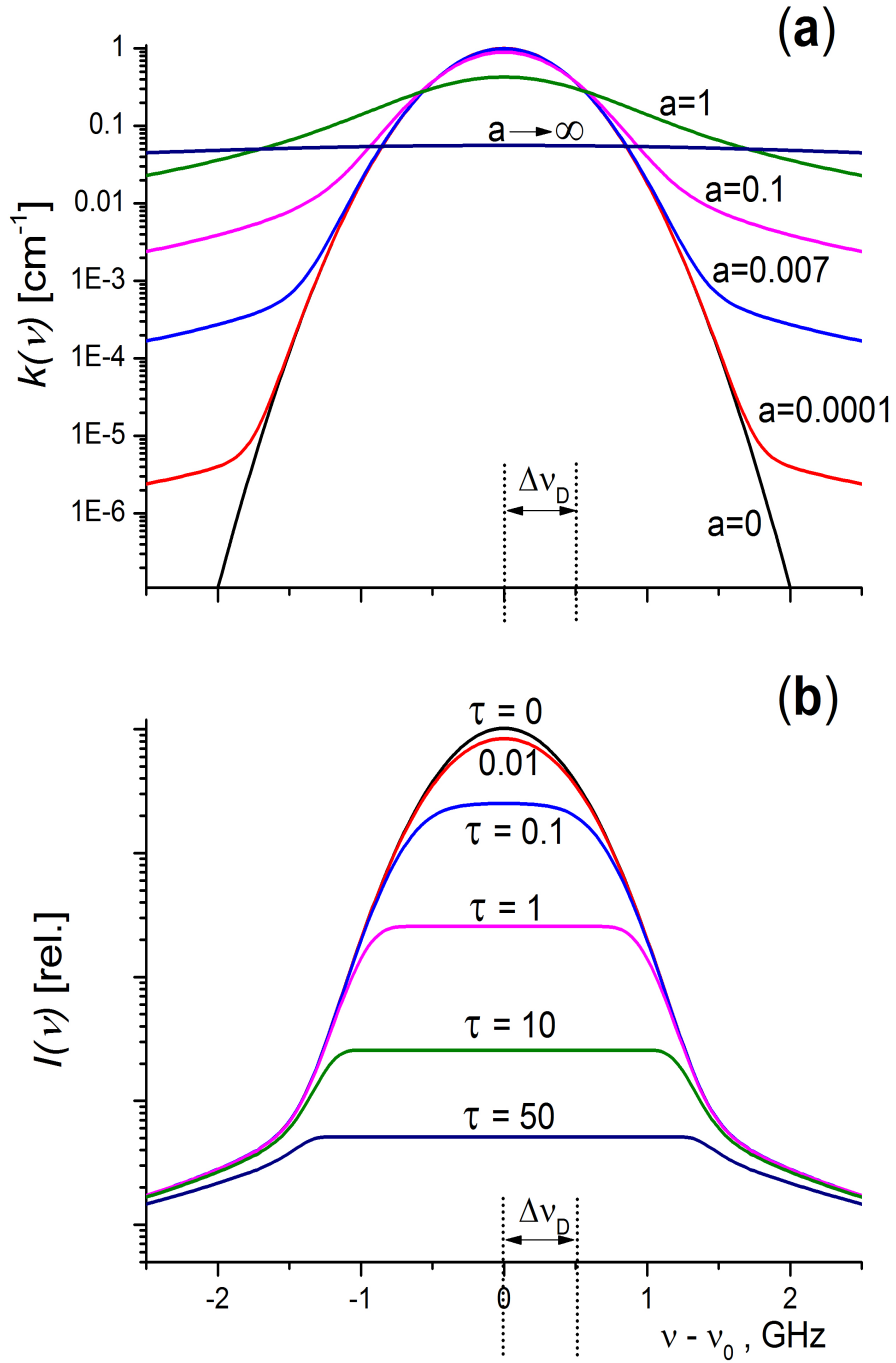


Figure 2.2: The lineshapes. In the upper graph (a) Voigt lineshapes with different values of parameter a are shown; among others - the limiting case of Doppler profile at $a = 0.0$ and the curve of current relevance with $a = 0.007$. In the lower graph (b) the self-absorbed Voigt profiles (with $a = 0.007$) are shown calculated with Eq.2.3 at different opacities $\tau = k(\nu_0)L$. One can observe the characteristic flattening of the profiles in the range of frequencies where the condition $k(\nu)L \gtrsim 0.1$ is true. At larger τ there are two competing strategies for a photon to escape: 1) quasi-diffusion within *the core* or 2) re-emission in *the wing* followed by immediate escape because the plasma column is optically thin there. The latter strategy gains in relative importance with increasing τ .

els. Since the lifetime of the $2p_6$ -level is much shorter than that of $1s_5$ -state and is determined by the sum of a few possible radiative decay channel the natural linewidth is $\Delta\nu_n = (A_{1s5-2p6} + A_{1s4-2p6} + A_{1s2-2p6})/2\pi = 5.5 \cdot 10^6$ Hz. The experimentally determined coefficient for pressure (collisional) broadening can be found in [36], where $2\gamma/N = 2.4 \cdot 10^{-20} \text{ cm}^{-1}\text{cm}^3$. For the pressure $p = 10$ Pa (the middle of our working range) this yields $\Delta\nu_{pr} = 1.5 \cdot 10^6$ Hz and the Voigt-parameter takes the value $a = 0.007$. The collisional broadening becomes equal to the natural one at $p \sim 35$ Pa, and at 3300 Pa (25 Torr) it comes up with the Doppler-width.

A family of Voigt-lineshapes generated by different values of parameter a is shown in Fig. 2.2(a). With $a = 0.007$ the central part of the line (*the core*) is indistinguishable from a pure Gaussian, but outside the limits $\nu - \nu_0 \approx \pm 3\Delta\nu$ *the wings* fall off much more slowly due to the contribution of Lorentzian part. Such a lineshape automatically guarantees that the pure-Doppler assumption works good in the optically-thin plasmas, but optically thick regimes require special consideration. In the latter case *the core* is strongly reabsorbed and *the wings* start to play more important role, which is increasing with growing opacity τ . When the contribution of *the wings* becomes noticeable then the pure-Doppler line assumption underestimates the rate of radiation escape from the discharge.

To illustrate the effect of self-absorption it is appropriate to consider the following integral

$$I(\nu) = \int_0^L E(\nu) e^{-k(\nu)x} dx . \quad (2.3)$$

It gives the amount of radiation coming out at frequency ν from a homogeneous plasma column of length L and allows for self-absorption in the column. The spectral intensity of the emission line is represented by $E(\nu)$, the functions $E(\nu)$ and $k(\nu)$ have identical lineshapes but are different in units and magnitudes. Fig. 2.2(b) shows the results of calculation with Eq. 2.3 for the Voigt profile at various opacities $\tau = k(\nu_0)L$.

One can see how with increasing opacity the whole profile shrinks, but the subsidence is more pronounced in *the core* than in *the wings*, and this makes the latter's relative contribution grow. This effect is additionally illustrated in Fig.2.3, where the behavior of the relative contributions of *the core* and *the wings* are compared for the Voigt and Doppler lineshapes.

For the Voigt profile *the wings'* contribution is much larger and comes up with *the core* at $\tau \sim 100$. This means the complete failure of the pure-Doppler assumption at the point.

The maximum value (at our experimental conditions) $\tau \sim 10$ for the 763.51 nm line implies that the Doppler profile would underestimate the radiation transport by 10%. Since this particular transition was the strongest which we used, the other transitions were characterized by smaller opacities and 10% sets up therefore the limiting value for the error associated with the pure-Doppler assumption. Interestingly, this limitation results primarily from the natural broadening.

In this way the emission spectra data was brought to connection with the model. We chose 10 lines from altogether 30 of $2p - 1s$ transitions array and got the densities of

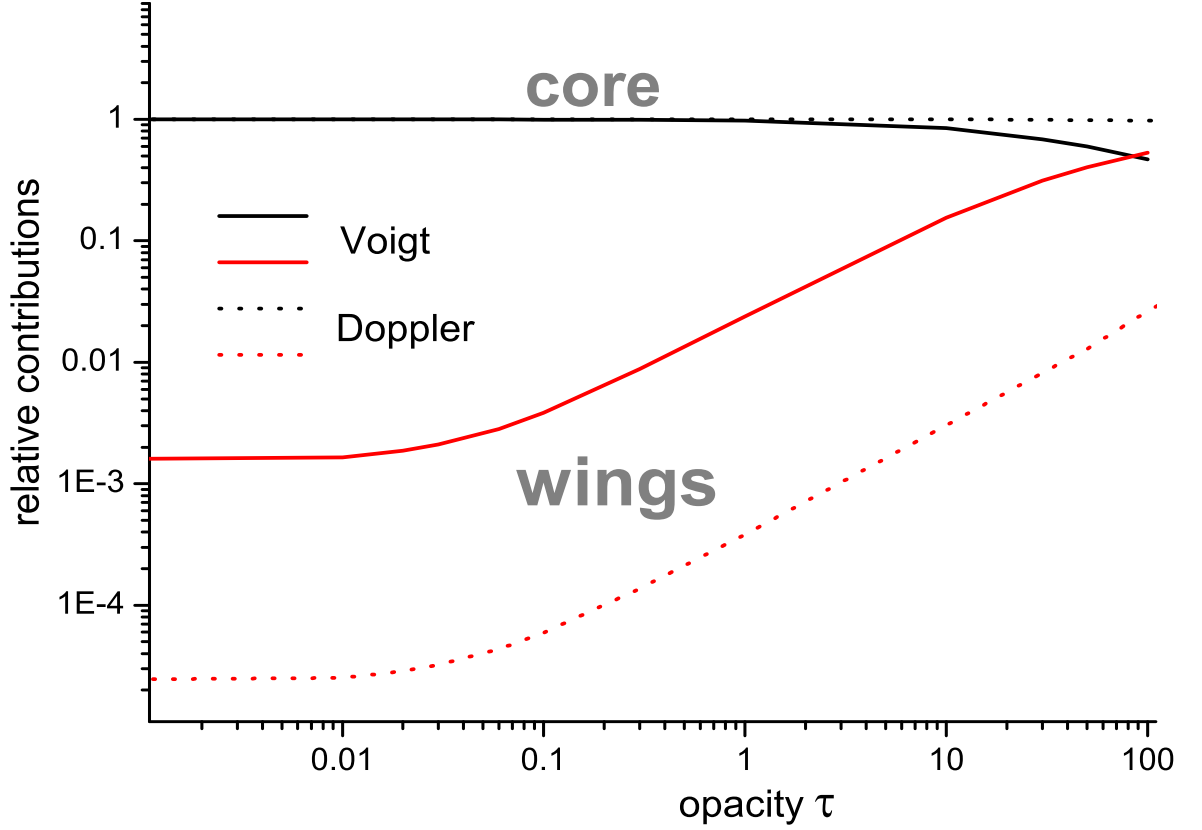


Figure 2.3: The contributions of the *core* and the *wings* to the total radiation transport. In order to clarify the difference between the Voigt and the Doppler *wings*, their contributions are calculated as a self-absorbed line (Fig.2.2(b)) integrated over frequencies beyond the region $[\nu_0 - 3\nu_D; \nu_0 + 3\nu_D]$, the *core* is accordingly evaluated by integration within this interval.

1s-states. The mathematical procedure of handling the data and using the least-square method is given in some detail in **Article II**.

The number densities found in this work display proportions typical for situations with smaller electron densities $n_e \sim 10^9 \text{cm}^{-3}$. At higher plasma densities analogous proportions tend to equilibrium values like in the case of PMD ($n_e \sim 10^{11} \text{cm}^{-3}$) examined in the next Section. In the present case of lower plasma density the metastable state reach higher population due to the reduced collisional losses. In the mean time, the reduced intermixing between 1s-states cannot keep them in equilibrium with each other. This leads to a large separation in populations, because the resonant state additionally has a strong destruction channel through the radiative decay.

2.2 Aspects and Modeling of laboratory discharges

2.2.1 Magnetron

General remarks

The excited atoms form an integral part of the whole physical picture of a discharge, being involved in a wide range of interactions. The detailed understanding of the mechanisms which govern the behavior of this species enables that they can be used as a sensitive diagnostic tool. In this regard, the two lowest-lying excited levels of argon atom are best suited for such diagnostics.

In order to accurately and self-consistently model the population of a given atomic state, in a non-equilibrium non-stationary plasma it is indispensable to employ a whole set of many other excited states, in a way similar to the one in work [37]. Alternatively, the physics behind the observed phenomena can be as well elucidated by relatively simple models, when the self-consistency condition is no longer strictly demanded. In this case *simple* means using reasonable simplifying assumptions and retaining only limited number of the most important processes.

The behavior of excited states is essentially the result of collisional inelastic processes and gas dynamics. Due to complexity of discharge phenomena (gas rarefaction, hot electrons, etc.) a simple quantitative modeling of the active phase would require a lot of free parameters to assume. Whereas in the afterglow phase it's enough to handle the integral electron characteristics - number density n_e and temperature T_e . The rest depends on the collisional characteristics known a priori, the number of important electron-induced mechanisms being limited through the reduced T_e .

For this reasons we focus on the modeling of $1s_5$ - and $1s_4$ -states in the afterglow of the HiPIMS discharge. We solve the balance equations for these two states, and the results are presented in **Article I**. The balance equation is differential equation for the time-derivative of a number density in the general form

$$\frac{dn}{dt} = \sum_k G_k - \sum_j L_j , \quad (2.4)$$

where G_k are the rates of gain process and L_j are the loss rates. Now in the next section we take a closer look at these processes.

The collisional processes

Since HiPIMS represents a low-pressure discharge with high electron number density, the kinetics of the excited states is dominated by inelastic atom-electron collisions while atom-atom collisions primarily bring about just the elastic temperature equilibration. Here we discuss in more detail these electronic interactions, which provide ground for the crucial assumptions in **Article I**.

Our considerations and arguments deal with the populations of the lowest-excited states of argon belonging to $3p^54s$ -configuration. Though calculations have been made

for both metastable $1s_5$ and resonance $1s_4$ states, we will mainly refer to the metastables for illustration.

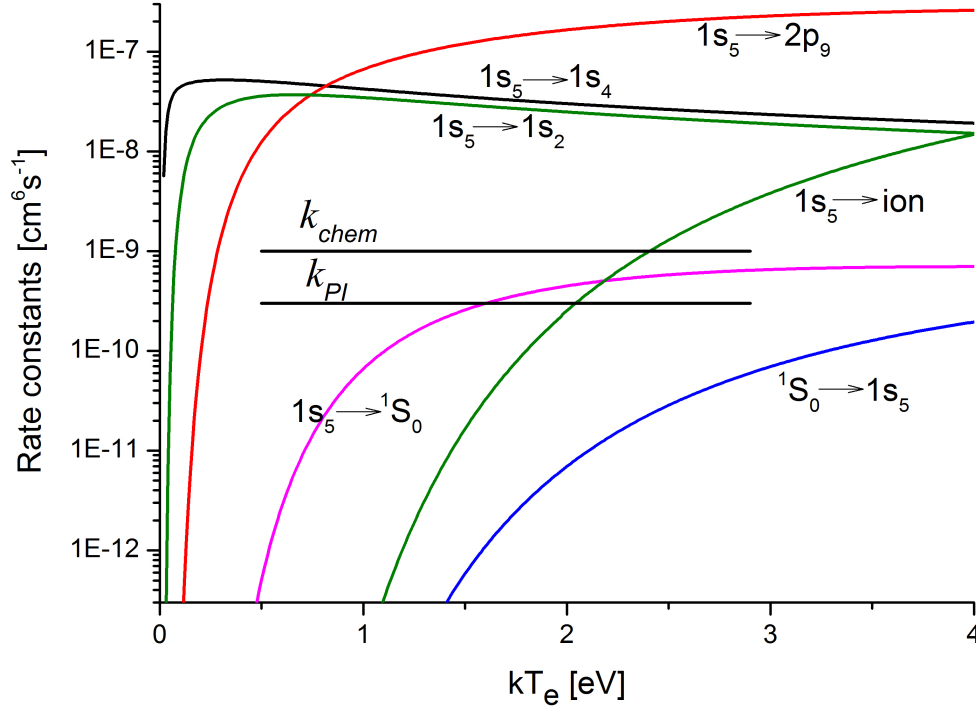


Figure 2.4: The rate constants for collisional processes used in the model. The values for the electron-impact rates were calculated using Maxwellian EDF from the cross-sections given in [38] for the $1s_j$ - $1s_k$ and $1s_j$ - $2p_m$ processes, in [39] for the ground state-metastable transition (the reversed process evaluated by means of the detailed balance condition from the direct excitation) and in [40] for the ionisation out of metastable state. For comparison also plotted are the values of chemoinisation k_{chem} [41] and Penning ionisation k_{PI} [42] rate constants.

Apart from very few processes - radiation decay for the resonance atoms and diffusion of metastables in the late afterglow - no other can compete in rates with the interactions driven by electron collisions. Such non-electronic processes like chemo- and Penning ionisation are of minor importance. The Penning ionisation of the sputtered material by metastable/resonant atoms may play an important role in the overall ionisation of the this material (at least in other types of magnetron sputtering discharges [43]). The rate of this process k_{PI} , however, is at least two orders of magnitude smaller than the electron-collision rates as can be seen in Fig.2.4. Given the fact that the number densities of electrons and sputtered atoms are comparable in magnitude we find that the role of Penning ionisation as destruction channel for the metastables is marginal. The rate

constant for chemionisation k_{chem} is somewhat higher, but in view of the larger electron density (by order of magnitude higher than that of metastables) the loss due to this mechanism is also negligible in the total losses.

For 1s-atoms the dominant destruction and population processes are the transitions to and from the other excited states. At electron temperatures typical for the afterglow regime ($kT_e < 2$ eV) such mechanisms like ionisation out of metastable state or excitation from the ground state amount to very little in the total balance (see Fig.2.4). The kinetics of 1s-states is determined by strong intermixing between 1s-sublevels as well as by collisional coupling to 2p-manifold. Due to the long-range dipole interaction the cross-sections for this $3p^54s - 3p^54p$ electron-impact transitions are vastly superior to those for other possible $3p^54s - 3p^5nl$ transitions [44]. Speaking of the metastable 1s₅-state in particular, the largest cross-section is to the 2p₉-level, which is also a pure L-S triplet state (3D_3) like the metastable itself. It makes about the half of the total cross-section for transitions to 2p-manifold, and the rest half is essentially made of 2p₁₀-, 2p₈- and 2p₆- transitions [38]. As Fig.2.4 shows, at somewhat higher T_e the 1s - 2p processes may play dominant role and in our case are responsible for the steep downfall of the metastables in the early afterglow. I chose the collisional interaction $k_{1s5 \rightarrow 2p9}^e(T_e)$ to represent all ten 1s₅ - p_j transitions, this rate constant is multiplied by a numerical coefficient to be fitted. The intermixing of 1s₅- and 1s₄-states was explicitly included in the model. As for the interactions with other 1s-states, their influence was neglected either because the states were assumed to be in equilibrium with the metastable level or the corresponding losses were much smaller than other processes (at lower $kT_e < 0.25$ eV in the late afterglow $k_{1s5 \rightarrow 1s2}^e(T_e) \ll k_{1s5 \rightarrow 1s4}^e(T_e)$).

Regimes of electronic non-equilibrium

Under equilibrium conditions, for any pair of atomic states E_j and E_k with densities n_j and n_k the *population flux* $j \rightarrow k$ induced by electron collisions $n_j n_e k_{jk}^e(T_e)$ is equal to the analogous flux of the inverse process $n_k n_e k_{kj}^e(T_e)$, entailing the Boltzmann relation for the populations

$$n_k/g_k = n_j/g_j \cdot \exp(-(E_j - E_k)/kT_e) . \quad (2.5)$$

When the populations do not fulfill this relation, the fluxes are not equal and the net difference between them $n_k n_e k_{jk}^e(T_e) - n_j n_e k_{kj}^e(T_e)$ is acting to compensate the departure from the relation.

The low-pressure discharges embody non-equilibrium plasmas. Various practical realizations of the non-equilibrium usually fall within two general types. In the active phase of a discharge the upper level of a given pair of states are commonly underpopulated in terms of Eq.2.5, then it is said to be in the *non-equilibrium of ionisation type* (NEI). The other way round, in afterglows the upper states are overpopulated, and this qualifies the *non-equilibrium of recombination type* (NER). These two types of non-equilibrium determine different regimes of exchange in populations between excited states.

When we speak of the lowest-lying states like the metastable and the resonance, it is helpful to consider the electron-impact interactions with all higher-lying levels. Then it

proves that this interaction leads to the net loss in case of NEI

$$\sum_{k>j}^n n_k n_e k_{kj}^e(T_e) - n_j n_e k_{jk}^e(T_e) < 0 , \quad (2.6)$$

while, on the contrary, this flux is positive in the NER regime.

The equilibrium value of electrons density at a given T_e is determined by the Saha equation, which we will use later in Sec.3.1.2

$$\frac{n_e n_i}{n_a} = \frac{(2\pi m_e)^{3/2}}{h^3} \frac{2G_i}{G_a} T_e^{3/2} \exp\left(-\frac{E_i}{kT_e}\right) , \quad (2.7)$$

with G_a and G_i being the statistical sums for the atom and the ion, respectively.

As kT_e goes far below 1.5 eV the non-equilibrium is increasingly of recombination type (NER), and electron collisions lead to effective population of the metastable level instead of destruction, giving rise to the afterglow peak at $t \approx 1.3$ ms. This process can be accounted for by a term which gives the global recombination rate. A recombination event is not a simple elementary act. It is a result of sequence of inelastic processes, starting from the initial capture by an ion of an electron with formation of a highly-excited atomic state. This weakly bound state can be easily re-ionised by a thermal electron or drift further down in the energy space to the lower binding states. Drifting to the states with smaller reionisation probability is then determinative for the global rate of recombination which describes the population the low-lying excited states. In **Articles I** we compare two alternative recombination terms. The first for the collisional-radiative stabilization is the well established expression with electron-dependent scaling [45]

$$\sim n_e^3 / T_e^{9/2} , \quad (2.8)$$

while the second for the microfield-limited stabilization depends on the electron parameters as

$$\sim n_e^{7/3} / T_e^2 . \quad (2.9)$$

It is inferred from the rate of recombination to a single state of the principal quantum number n : $\rho_n = C n_e^2 n_{ion} n^4 (1 - \exp(-E_n/kT_e))(g_n/g_{ion}g_e)$ [46]. Such rates are summed up for all states which lie below the principal number $n = p_m$ given by the microfield limit [47]. The result of this summation[†] is the scaling law Eq.2.9 as long as holds $p_m^2 kT_e \gg E_i$. The *recombination flux* given by these expressions is assumed to go through the resonance and metastable states and is shared between them with effective weight factors a_r and a_m which were adjustable parameters in the simulations of **Article I**.

[†]Y.Celik, *Private Communication*

2.2.2 RF-discharge

The experiments in **Articles II-IV** have been made in RF-discharges. In **Article III** and **Article IV** the video records of a dust particle's oscillatory movement in the sheath were taken and analyzed. It was necessary to develop a sheath model to be able to explain the behavior of the dust particle. In the coming paragraphs I describe the model whose full description was omitted in the papers.

Floating body in the rf-sheath

From the point of view of discharge physics a floating body and the powered electrode in a highly-asymmetric RF-discharge are very similar at least in one respect - in the way how the floating potential V_f and the negative dc-bias V_{dc} appear. In both cases the condition of equality of the collected electronic I_e and ionic I_i currents have to be fulfilled.

Yet, what makes them different is that the electrode's potential is controlled externally. This essentially determines the sheath dynamics and the properties of electronic and ionic components. The electron and ion concentrations are necessary in order to calculate the potential of a floating object at a given position.

A high-voltage sheath is a near-electrode zone with failed quasineutrality. Due to uncompensated space charge a strong electric field is present in this region. In a bottom electrode configuration this field can make negatively charged particles levitate, acting against the gravitational force. In the following considerations we refer to a larger particle, which was of radius $r \approx 130 \mu\text{m}$ in our specific case. Because this size is comparable with the Debye-screening length, the relations between floating potential and charge, charge and electric force are more complicated as in a usual case of very small particles (see formulas (8, 14) in **Article III**).

The zero point $x = 0$ is set at the plasma-sheath boundary, thus the cathode surface is at $x = d$. At a given position x in the sheath, the flux of electrons due to the thermal-chaotic movement is $1/4 n_e(x) \bar{v}_e$ where \bar{v}_e is the mean thermal velocity. For a particle of area $4\pi r^2$ charged to the potential V_f the collected current of thermal electrons is

$$I_e = \pi r^2 n_e(x) \bar{v}_e \exp \frac{V_f}{kT_e} \quad (2.10)$$

The movement of ions in the sheath is dominated by the directed velocity component $u_i(x)$. This directionality is responsible for the effective collection area of πr^2 . If we take the orbit-motion limited cross-section for the ion capture, we come the following expression for the ion current onto the particle

$$I_i = \pi r^2 n_i(x) u_i(x) \left(1 - \frac{e_0 V_f}{m_i u_i(x)/2} \right) \quad (2.11)$$

where m_i is the ion mass and e_0 is the positive elementary charge. From the balance of both currents

$$\pi r^2 n_e(x) \bar{v}_e \exp \frac{V_f}{kT_e} = \pi r^2 n_i(x) u_i(x) \left(1 - \frac{e_0 V_f}{m_i u_i(x)/2} \right) \quad (2.12)$$

the floating potential $V_f(x)$ can be determined. Note that since $n_e(0) = n_i(0)$, the resulting floating potential does not depend on the magnitude of the plasma density, it is determined by the relative profiles $n_e(x)/n_e(0)$ and $n_i(x)/n_i(0)$ which are the same for different boundary values $n_e(0)$.

The estimations from the the magnitudes of the charged particles fluxes show that it needs a lot (at least a few tens) of rf-periods to charge/discharge our particle, which is big enough to carry charge of at least several millions negative elementary charges). So, the particle's behavior was modeled as movement of a large constant charge in the averaged sheath environment.

In the frame of a simple self-consistent model the electron density $n_e(x)$ is given by

$$n_e(x) = n_e(0) \exp \frac{eV_s(x)}{kT_e} I_0 \left(\frac{eV_s(x)}{kT_e} \frac{V_{rf}}{V_{dc}} \right) \quad (2.13)$$

where I_0 stays for the zeroth-order modified Bessel function of the first kind, $V_s(x)$ is the dc-potential in the sheath (with respect to the plasma potential), V_{dc} is the total voltage drop through the sheath $V_{dc} = V_s(d)$, V_{rf} is the voltage amplitude of the rf-component. The Bessel-factor in this expression is responsible for the "rf-enhanced" electron density, arising from the averaging over sheath dynamics. This density decreases much more slowly as it would do just in a static potential V_s . The amplitudes V_{dc} and V_{rf} are related by a transcendental equation, which allows one to evaluate V_{rf} when V_{dc} is known

$$\frac{eV_{dc}}{kT_e} = \frac{eV_f(0)}{kT_e} - \ln I_0 \left(\frac{eV_{rf}}{kT_e} \right). \quad (2.14)$$

The ions do not feel the oscillating part of the potential, they essentially move in the time-averaged static field. Without collisions in the sheath the ion flux is conserved $n_i(x)u_i(x) = n_i(0)u_i(0)$ with $u_i(0) = v_B$ being the Bohm velocity. The ion velocity $u_i(x)$ is changing due to free acceleration in the electric field and density $n_i(x)$ is then determined by $u_i(x)$ and boundary conditions. These expressions need to be modified when there are ion-neutral collisions in the sheath. Engaging the ion momentum continuity equation, one can show [48] that in a weakly collisional regime $n_i(x) = n_i^{\lambda_i=\infty}(x) F^{-1/2}(x)$ and $u_i(x) = v_B F^{1/2}(x)$, where $F(x)$ is given by

$$F(x) = \exp \left(\frac{-\pi}{\lambda_i} x \right) - \frac{e_0 V_s(x)}{m_i v_B^2/2} + \frac{-\pi}{\lambda_i m_i v_B^2/2} \exp \left(\frac{-\pi}{\lambda_i} x \right) \int_0^x e_0 V_s(y) \exp \left(\frac{\pi}{\lambda_i} y \right) dy. \quad (2.15)$$

The simulations of ion and electron density profiles are illustrated later in Sec.3.3.1.

We also examined the effect of secondary electrons released by ion bombardment of the electrode. Even though their flux is small (determined by coefficient $\gamma_i \approx 0.05$ [49]), due to high energies they easily overcome the potential barrier of V_f . Now less thermal electrons are needed to equilibrate the ion current and this effect makes the floating potential more negative. It is seen in the results shown in Sec.3.3.1.

Chapter 3

Results/Publications

3.1 Absorption spectroscopy of Pulsed Magnetron Discharge

3.1.1 Initial conditions and input parameters

The time-dependent balance equations 2.4 need to be supplied by the initial conditions in order to be solved in the frame of the initial value problem. For this purpose we took the data at pressure $p = 4$ Pa and pulse duration $t = 200 \mu s$, see Fig.3.1. The experimental number densities at the time point where the pulse ends were used as initial values, and then the balance equations were solved for the afterglow phase using the Mathcad software.

The initial value of the electron temperature was somewhat arbitrarily chosen to be $kT_e^0 = 3$ eV. In fact, it could as well be 2 eV - this would cause only a slight change in the rest fitting parameters; however, initial values below $kT_e^0 = 1$ eV could not provide reasonable fit to the experimental data. We can also try to get an estimate for kT_e^0 from the drop of the derivative curve, see part 3.1.3 for details. This estimation yields a value around 1.4 eV.

The time-curve of electron concentration was taken from the Langmuir-probe measurements, which belonged to the series of experiments described in [50]. The temperature T_e was modeled assuming exponential decay and a plateau value in the end. As is common, the meaning of T_e is that it is the *effective* temperature. Yet still, owing to high electrons density in HiPIMS, the electron-electron collisions provide an efficient equilibration mechanism leading to a Maxwell-like distribution function (EDF) [51] at least in the region of kinetic energies up to a few electron-volts which is employed in the most important processes of the afterglow.

The results of the simulations are found in **Article I**.

3.1.2 Experimental data in view of electronic non-equilibrium

Now we are going to exemplify the speculations of Sec.2.2.1 concerning different regimes of non-equilibrium for the present case of HiPIMS discharge. For this purpose we com-

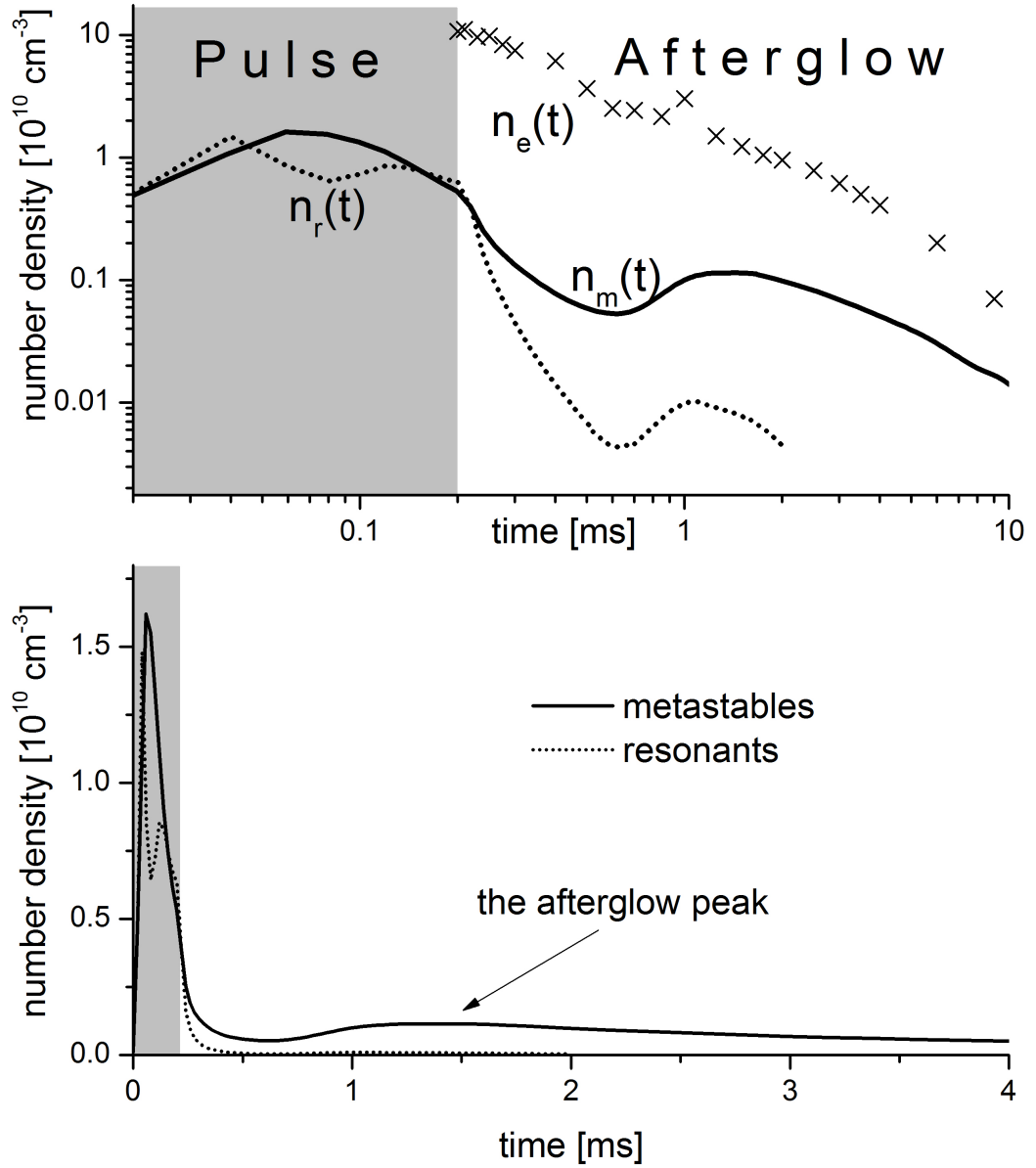


Figure 3.1: Densities of the resonance $n_r(t)$ and metastable $n_m(t)$ states in a HiPIMS discharge, measured with time-resolved TDLAS technique; also shown is the electron number density $n_e(t)$ (available only for afterglow). The gray region marks the active phase of discharge.

	ACTIVE PHASE		AFTERGLOW	
	equilibrium with $kT_e=2$ eV	experiment	equilibrium with $kT_e=0.2$ eV	experiment
$n_m[cm^{-3}]$	$3.5 \cdot 10^{13}$	$\sim 10^{10}$	$\ll 1$	$10^8 - 10^9$
$n_e[cm^{-3}]$	$0.3 \cdot 10^{18}$	$10^{11} - 10^{12}$	$0.2 \cdot 10^2$	$10^9 - 10^{10}$

Table 3.1: Comparison of the equilibrium values of n_m and n_e to those observed in the experiment. The equilibrium values are estimated using Eq. 2.5 and 3.1, the experimental values are visualized in Fig.(3.1)

pare the actual and equilibrium values of metastable n_m and electron n_e densities.

The statistical sum for atoms is taken as $G_a = 1$ because the lowest excited level is far from the ground state $E_m = 11.55$ eV $\gg kT_e$ and for ions $G_i = 6$ given the fact that the two lowest states with degeneracy 4 and 2 are separated in energy by 0.177 eV and the energy 13.48 eV of the third level is large [52]. Making use of the conventional assumptions (three-component plasma, $n_e = n_i$, $n_e \ll n_a$) and evaluating the numerical factor in formula (2.7), we finally arrive at the expression which gives an estimate for the equilibrium plasma density

$$n_e \approx 3 \cdot 10^{11} N_a^{1/2} (kT_e)^{3/4} \exp\left(\frac{E_i}{2kT_e}\right). \quad (3.1)$$

We can learn from Table 3.1 that the number densities n_m and n_e in the active phase of discharge are fairly underpopulated with respect to the equilibrium, and contrariwise in the afterglow they are too abundant. For the illustration purposes I picked $kT_e = 2$ eV to represent the active phase and $kT_e = 0.2$ eV - the afterglow. We can see that the difference between the experimental n_m , n_e and the corresponding equilibrium values are typically many orders of magnitude. This is a good demonstration of the statement that NEI occurs in the active phase and NER in the afterglow. The abrupt drop of the electron temperature T_e in the early afterglow causes transition between these regimes. The experimental data corresponds to equilibrium parameters at $kT_e \sim 0.4 \div 1.0$ eV. When energy gaps between the excited states meet the condition $\Delta E \ll kT_e$ and the population dynamics of these closely lying levels is dominated by electron-induced transitions, then the ratio of the densities is expected to be not far from the equilibrium ratio given by Eq.2.5. Such is the case with the states from 1s-manifold. When we look at the experimental data in Fig.3.1 we see that in the active phase of discharge the number densities n_m and n_r are comparable in magnitude, because they are brought near to equilibrium value of $n_r/n_m = 3/5 \exp(-0.076/kT_e)$ through intermixing by electron collisions. At a certain time point in the early afterglow these two levels decouple and the resonance-state curve rapidly drops off; at this time point ($\sim 30 \mu s$ after switching off) the loss due to radiation decay overtakes in the balance equation for the resonance

state.

The concept of NEI and NER regimes is useful when we describe the interaction of the metastable and resonance levels with the populations of the ten 2p-states. At NEI (active phase and early afterglow) the p-states are underpopulated with respect to s-states, the collisional transfer from s- to p-states is more intensive than the inversed process which results in the effective destruction of s-states. As was said above, this interaction have been lump-sum represented by $k_{1s5 \rightarrow 2p9}^e(T_e)$. For a good fit of the experimental data the effective destruction coefficient of $0.5k_{1s5 \rightarrow 2p9}^e$ was needed in the initial phase of the afterglow. This implies underpopulation of p -levels by factor 4.0. Soon after the begin of afterglow the NEI gives way to NER-regime when 1-s states are effectively populated through interaction with 2p-states which in turn are populated by the recombination flux. Our calculation showed that both formulas could be used to represent the recombination. In our case the expression with collisional-radiative scaling (2.8) matched slightly better with the absolute values, but the expressions (2.8) and (2.9) are anyway very sensitive to the input characteristics of electrons.

Further results see in **Article I**.

3.1.3 Estimation of the electron temperature

The time derivative $dn_m(t)/dt$ jumps at the point of pulse termination, see Fig.3.2. We attribute this jump to the 'switching off' of the excitation processes from the ground state due to a fast change in electron temperature ΔT_e . This population process, characterized by the rate constant $k_{gm}^e(T_e)$, has sharp T_e -dependences and is strong enough to produce the jump effect. As soon as the process is identified we can estimate the electron temperature T_e from the magnitude of this jump ΔK . Since we assume that the rates of other processes as well as the electron density n_e do not change during this short time interval ($\sim 30\mu s$), we can write

$$\Delta K = \frac{dn_m(t_1)}{dt} - \frac{dn_m(0)}{dt} = N_{gas}n_e k_{gm}^e(T_e^0) - N_{gas}n_e k_{gm}^e(T_e^0 - \Delta T) \quad (3.2)$$

$$k_{gm}^e(T_e^0) - k_{gm}^e(T_e^0 - \Delta T) \approx \frac{\Delta K}{N_{gas}n_e}, \quad (3.3)$$

where $T_e^0 = T_e(t = 200\mu s)$ is the initial electron temperature which drops by ΔT_e during the dip.

It can be easily shown that the rate constant of any threshold-type process can be well approximated by an expression of the functional form $(a + bT_e) \exp(-E_{thresh}/kT_e)$. It ensures, amongst other things, an exponential decrease at $kT_e \ll E_{thresh}$. With the rate constant k_{gm}^e ($E_{thresh} = E_m = 11.55$ eV) this decrease results in a much smaller

If the cross-section is represented by a linear function which is zero and then starts to increase at certain threshold value of argument $\sigma(\epsilon) = c_{th}(\epsilon - \epsilon_{thres})$, then the exact result of averaging of the product $\langle \sigma(\epsilon)v \rangle \equiv k(T)$ over a Maxwellian distribution function is $k(T) = c_{th}(\epsilon_{thres} + 2kT) \exp(-\epsilon_{thres}/kT)$. Accordingly, such a T-dependance is appropriate also in case of a realistic cross-section so long as holds $kT \ll \epsilon_{thres}$.

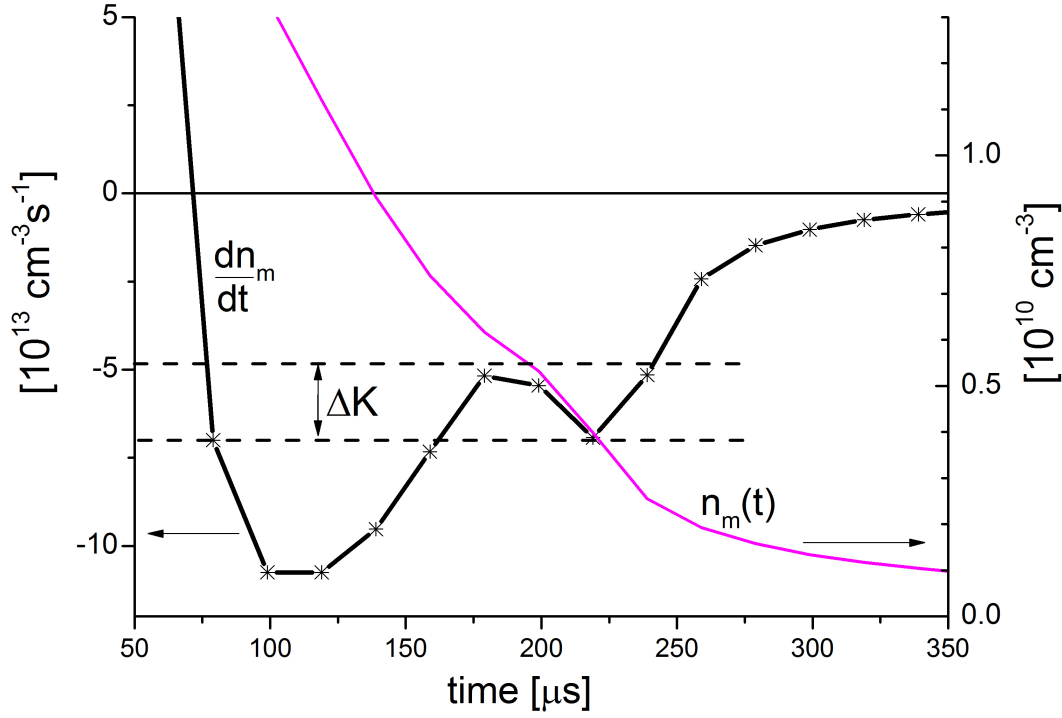


Figure 3.2: The experimental curve of metastables and its time-derivative. Shown is the time interval surrounding the pulse - afterglow transition. For a short time immediately after pulse termination the decrease is accelerated, which is distinctly seen in the course of the derivative plot.

magnitude of $k_{gm}^e(T_{e0} - \Delta T)$ than $k_{gm}^e(T_e^0)$ - with temperature drop ΔT of only 25% of the initial value T_e^0

$$k_{gm}^e(T_e^0)/k_{gm}^e(T_e^0 - 0.25T_e^0) \approx 7, \quad (3.4)$$

where $T_e^0 = 2.0$ eV (at lower T_e^0 the effect is even more pronounced). Therefore, assuming $k_{gm}^e(T_e^0) \gg k_{gm}^e(T_e^0 - \Delta T)$ we can omit the second term in the LHS of Eq.(3.3):

$$k_{exc}(T_{e0}) \approx \frac{\Delta K}{N_{gas}n_e} \quad (3.5)$$

Resolving this equation for the electron temperature, we obtain $T_e^0 \approx 1.3$ eV. The analogous estimation from the variation of the resonance state's density yields $T_e^0 \approx 1.5$ eV.

Article I

Time-resolved tunable diode laser absorption spectroscopy of excited argon and ground-state titanium atoms in pulsed magnetron discharges

Time-resolved tunable diode laser absorption spectroscopy of excited argon and ground-state titanium atoms in pulsed magnetron discharges

V Sushkov¹, H T Do^{1,3}, M Cada², Z Hubicka² and R Hippler¹

¹ Institut für Physik, Ernst-Moritz-Arndt-Universität Greifswald, Felix-Hausdorff-Str. 6, 17489 Greifswald, Germany

² Institute of Physics, Academy of Science of the Czech Republic, Na Slovance 2, 182 21 Praha 8, Czech Republic

E-mail: hippler@physik.uni-greifswald.de

Received 10 April 2012, in final form 18 October 2012

Published 29 November 2012

Online at stacks.iop.org/PSST/22/015002

Abstract

Time-resolved investigations of excited argon atom density and temperature and ground-state titanium atom density during high-power impulse magnetron sputtering (HiPIMS, repetition frequency 100 Hz) and direct current pulsed magnetron (repetition frequency 2.5 kHz) discharges (PMDs) in argon employing a titanium target were performed. Atom density and temperature were measured with the help of tunable diode laser absorption spectroscopy. Excited argon atoms form during the discharge pulse and again by three-body electron ion recombination in the afterglow. Similarly, the temperature of excited (metastable) argon atoms rises during the plasma *on* phase and again during the afterglow. The observed temporal evolution of the temperature is faster than expected from thermal conductivity considerations, which is taken as an indication that metastable and ground-state argon atoms are not in thermal equilibrium. The time dependence of titanium atoms can be explained by recombination and diffusion. The results provide new insights into the physics of PMDs.

(Some figures may appear in colour only in the online journal)

1. Introduction

Pulsed discharges are versatile tools to investigate transient plasma phenomena and are useful for many technical applications. Magnetron discharges operating at pressures of typically 1–10 Pa are frequently employed for deposition of thin solid films [1]. A particular variant is the high-power impulse magnetron sputtering (HiPIMS) discharge where the peak power typically exceeds the time-averaged power by two orders of magnitude [2–8]. Plasma densities can reach peak values of about 10^{19} m^{-3} and the total ionization degree may be as high as a few per cent, with the ionization degree of sputtered atoms even reaching values close to 100%. This results in

high ion fluxes and thereby may influence the physical and bio-chemical properties of the deposited films [9–11].

Tunable diode laser absorption spectroscopy (TDLAS) is a modern technique to investigate the heavy particle dynamics in various environments. TDLAS of metastable argon atoms has been used to investigate the kinetics of fast electrons in various discharge configurations [12–16] and to monitor the kinetic energy (temperature) of heavy particles in the plasma, deduced from the Doppler profile of the absorption line [17–21]. Recently, the density of metastable neon atoms in a complex neon plasma with immersed dust particles [22] and the density of metastable atoms in an argon/acetylene plasma with plasma-polymerized dust particles have been analyzed [23]. The kinetics of argon metastables in the afterglow of a pulsed complex plasma have also been investigated [24],

³ Present address: Institute of Physics, Vietnam Academy of Science and Technology, 10 Dao Tan Street, Hanoi, Vietnam.

but with the assumption that the gas temperature remains constant during the pulse which, as we shall see below, is not always justified. More recently, argon metastable density and temperature measurements during HiPIMS discharges were reported by Vitelaru *et al* [25].

In this paper we report time-resolved TDLAS measurements of excited argon and of ground-state titanium atoms in a pulsed magnetron discharge (PMD). Excited argon atoms form in the discharge by various processes including electron-impact excitation, neutralization of energetic argon atoms at surfaces, and by ion recombination in the gas phase. Measurements of both the density and the temperature of argon metastable atoms shedding new light on the relative importance of the various processes in sputtering discharges are reported. Titanium atoms are formed by sputtering of the cathode material and the temporal evolution of the titanium atom density was investigated.

2. Experimental set-up

The experiment was performed in an ultra-high vacuum chamber with a diameter of 35 cm and a length of 19 cm which was continuously pumped by a turbo-molecular pump (pumping speed 220 l s^{-1}) backed by a combination of roots and rotary vane pumps. After achieving a base pressure better than 10^{-5} Pa , the chamber was filled with argon to an operating pressure of 4–20 Pa. The gas flow rate was set to 10–60 sccm of argon. A Lesker Torus planar balanced magnetron equipped with a 5 cm diameter titanium target with a typical purity of 99.7% was employed [26].

The PMD was driven with the help of a dedicated HiPIMS power supply. The HiPIMS supply comprises a commercial dc power supply (Advanced Energy MDX-1 K, $U_{\text{max}} = 1.5 \text{ kV}$, $I_{\text{max}} = 1 \text{ A}$) and a home-built power switch unit based on charging a large capacitor during the idle part of the pulse. The power switch unit was capable of drawing up to 200 A. A ballast resistor of 5.5Ω incorporated into the power switch unit stabilized the discharge current. The repetition frequency of the pulsed discharge was kept at 100 Hz in the HiPIMS mode and at 2.5 kHz in the PMD mode; the active plasma pulse time during the experiments was set to 50, 100 or $200 \mu\text{s}$ (duty cycle 0.5%, 1%, or 2%) in HiPIMS and to $100 \mu\text{s}$ (duty cycle 25%) in PMD mode, respectively. Mean discharge currents were set to $I_D = 50\text{--}100 \text{ mA}$ and $50\text{--}500 \text{ mA}$ in HiPIMS and PMD mode, respectively. The corresponding peak current density was approximately $250\text{--}500 \text{ mA cm}^{-2}$ and $10\text{--}100 \text{ mA cm}^{-2}$ in HiPIMS and PMD mode, respectively. The waveforms before and behind the ballast resistor were monitored by two identical $\times 100$ voltage probes (Tektronix P5100) and recorded with a digital oscilloscope (Agilent DSO7104B). Subsequently, the current waveforms were numerically calculated from the recorded voltage waveforms according to Ohm's law.

Time-resolved light absorption spectroscopy was performed with the help of a tunable diode laser (TDL). The single mode diode laser (Toptica DL100) is equipped with an external cavity. The spectral band width (about a few MHz) is much smaller than the width the absorption profile (about a few GHz) in a low-pressure glow discharge. The TDL light

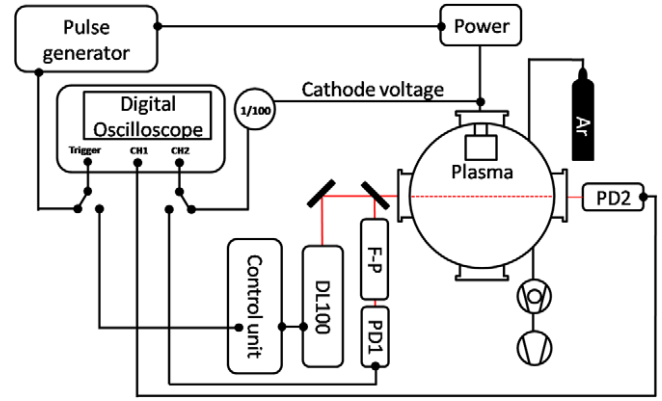


Figure 1. Experimental set-up (schematic).

beam is split into two parts with a beam splitter. The first beam is guided to a confocal Fabry–Pérot (FP) interferometer (1 GHz free spectral range) and detected with the first photodiode (PD1) to perform a calibration of the laser frequency scan. The second beam is launched into the discharge chamber where it passes parallel to the target and is detected on the opposite side of the chamber with the second photodiode (PD2) (figure 1). Measurements were carried out at a distance of 7 cm from the cathode. Two different laser diodes were employed. The ‘red’ diode laser was used for the argon $1s_4\text{--}2p_7$ and $1s_5\text{--}2p_9$ transitions (in Paschen’s notation) with a center wavelength of $\lambda = 810.37 \text{ nm}$ and 811.53 nm , respectively [27]. The ‘blue’ diode laser was set to the titanium $3d^2 4s^2\text{--}3d^2 4s 4p$ transition at $\lambda = 398.18 \text{ nm}$ [27]. Measurements were carried out at sufficiently low laser powers where saturation effects are small ($< 5\%$).

Absorption spectroscopy is based on the Beer–Lambert law

$$I(\nu) = I_0(\nu) \exp[-\kappa(\nu)l], \quad (1)$$

where the absorption coefficient $\kappa(\nu)$ can be expressed as

$$\kappa(\nu) = \kappa_0 \exp \left[-4 \ln 2 \left(\frac{\nu - \nu_0}{\Delta \nu_D} \right)^2 \right]. \quad (2)$$

$I(\nu)$ and $I_0(\nu)$ are the measured light intensities at frequency ν with and without absorbing atoms, respectively, $\kappa_0 \equiv \kappa(\nu_0)$ is the absorption coefficient in the center of the profile, l is the absorption length and $\Delta \nu_D$ is the Doppler width which relates to the gas temperature T of the absorbing species [20, 21]

$$T = \frac{\lambda_0^2 m_a}{8k \ln 2} \Delta \nu_D^2, \quad (3)$$

where m_a is the atomic mass of the investigated species, k is the Boltzmann constant and λ_0 is the center wavelength of the investigated transition. Equation (2) is valid in the case of a low-pressure (density) plasma when the line shape is controlled by Doppler-broadening.

For given $\kappa(\nu_0)$ and $\Delta \nu_D$ one can calculate the atom density as

$$n_m = \frac{8\pi \epsilon_0 m_e c}{e_0^2 f \lambda_0 l} \sqrt{\frac{2kT}{\pi m_a}} \kappa_0, \quad (4)$$

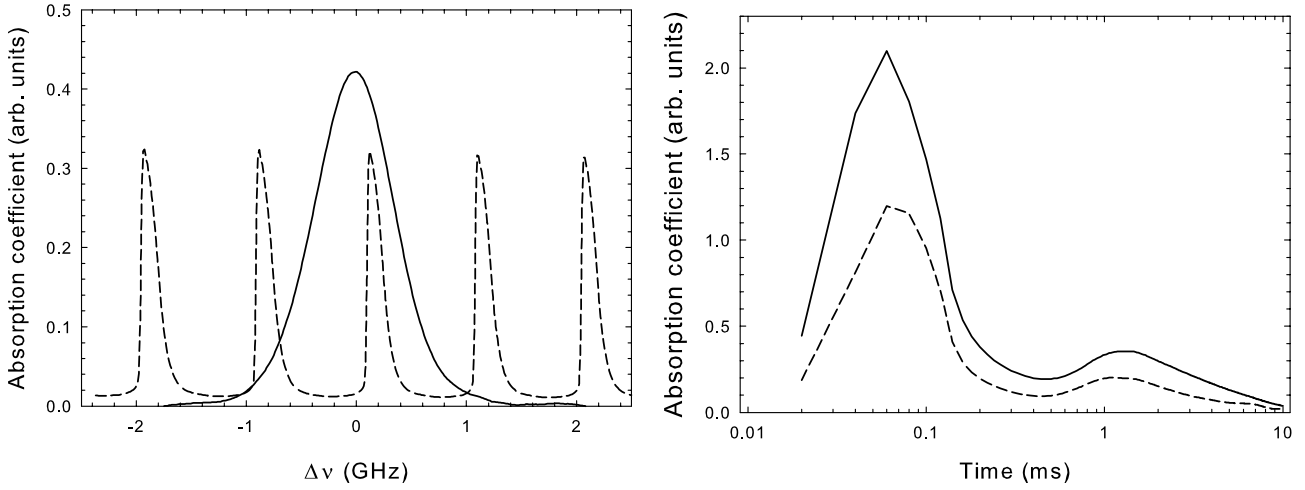


Figure 2. Left: FP-transmission signal (dashed line) with 1 GHz peak separation and time-averaged absorption coefficient (solid line) in PMD mode (pressure: 4 Pa, peak (mean) discharge current: 2 A (500 mA), Ti target). Right: time-resolved absorption coefficient at the center (solid line) and at the wing (dashed line) of the absorption profile. Data taken in HiPIMS mode (pressure 4 Pa, peak (mean) discharge current 8 A (80 mA), Ti target).

where ε_0 is the dielectric constant, c is the speed of light, m_e and e_0 are electron mass and charge, respectively, and f is the optical oscillator strength for the investigated transition. It should be kept in mind, however, that the reported densities are line-of-sight-averaged over the full observation length (40 cm). Assuming a Gaussian density profile with a full width at half maximum of 15 cm the estimated local density in the chamber center is about 2.5 times larger than the values below.

Under stationary conditions, the Doppler width $\Delta\nu_D$ is usually extracted by performing a full frequency scan of the Doppler profile (figure 2). In our experimental set-up this takes about 1 ms which is insufficient to record a full frequency scan, however. Fortunately, for a Doppler profile, knowing the absorption coefficients at two different frequencies is enough to rebuild the full profile. Time-resolved measurements were hence performed at only two frequencies ν_0 and ν_1 in the center and in the wing, respectively, of the absorption profile. The time-resolved temperature $T(t)$ and density $n_m(t)$ are evaluated from the measured absorption coefficients $\kappa_0 \equiv \kappa(\nu_0)$ and $\kappa_1 \equiv \kappa(\nu_1)$ (figure 2),

$$T(t) = \frac{\lambda_0^2 m_a}{2k} \frac{(\nu_1 - \nu_0)^2}{\ln(\kappa_0(t)/\kappa_1(t))} \quad (5)$$

and

$$n_m(t) = 4\sqrt{\pi} \frac{\varepsilon_0 m_e c}{e_0^2 f} \frac{|\nu_1 - \nu_0|}{\sqrt{\ln(\kappa_0(t)/\kappa_1(t))}} \kappa_0(t). \quad (6)$$

The yet unknown frequency difference $|\nu_1 - \nu_0|$ is obtained with the help of the time-averaged metastable density $\langle n_m \rangle$ obtained by integration of equation (6) over the pulse period t_p . It is evaluated as

$$\langle n_m \rangle t_p = 4\sqrt{\pi} \frac{\varepsilon_0 m_e c}{e_0^2 f} |\nu_1 - \nu_0| \int_0^{t_p} \frac{\kappa_0(t)}{\ln(\kappa_0(t)/\kappa_1(t))} dt, \quad (7)$$

from which we obtain

$$|\nu_1 - \nu_0| = \frac{e_0^2 f}{4\sqrt{\pi} \varepsilon_0 m_e c} \langle n_m \rangle t_p \left(\int_0^{t_p} \frac{\kappa_0(t)}{\ln(\kappa_0(t)/\kappa_1(t))} dt \right)^{-1}. \quad (8)$$

Making use of $\langle n_m \rangle$ from time-averaged measurement one can easily calculate $|\nu_1 - \nu_0|$.

In order to get the time-resolved metastable density and temperature it is, hence, necessary to measure five quantities: $I(\nu_0)$, $I_0(\nu_0)$, $I(\nu_1)$, $I_0(\nu_1)$ and the time-averaged density $\langle n_m \rangle$. For the time-averaged density measurements, the laser frequency was scanned around the line center and averaged over 8000 samples. Figure 2 shows an example of the absorption line profile together with the FP transmission signal. The frequency scale was calibrated using the transmission peaks of the FP etalon [23]. The time-averaged metastable density was deduced from the measured absorption coefficient with the help of equation (4).

In order to obtain the remaining four quantities, the laser was first run in the scan mode and the magnetron plasma in dc mode. The oscilloscope was triggered by the DL 100 control unit. The absorption profile from the dc magnetron plasma was used to set the laser wavelength to either the center (maximum absorption) or to the wing of the profile. After the laser wavelength was set, the laser intensity transmitted by the dc magnetron plasma was measured (I_{dc}). The plasma was then turned off to detect the laser intensity without plasma ($I_0(\nu)$).

The plasma was subsequently fired at the plasma conditions of interest. The oscilloscope was triggered by the pulse generator which also triggers the pulsed plasma. The cathode voltage was monitored with the help of a high-voltage probe connected to the second channel of the oscilloscope. In the time-resolved studies, the photo diode (PD2) signal is the sum of the transmitted light from the laser ($I(\nu)$) and the light emitted by the plasma (I_{pl}). In order to obtain $I(\nu)$ the plasma-emitted light I_{pl} was obtained from a measurement without laser and subtracted from the measured total ($I(\nu) + I_{pl}$) intensity.

After completion of the time-resolved measurement both reference values $I_0(\nu)$ and I_{dc} were recorded again. We only kept those time-resolved measurements for which the reference values before and after the measurement differed by less than

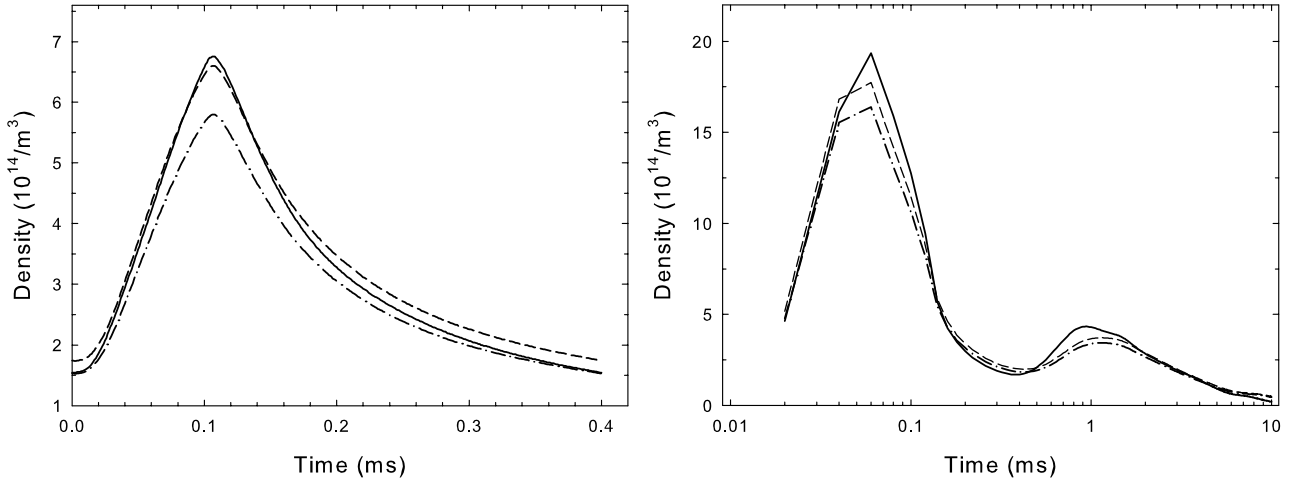


Figure 3. Comparison of calculated metastable densities making use of time-resolved temperature (solid line), time-averaged temperature (dashed line) and room temperature (dashed–dotted line) in PMD (left) and HiPIMS (right) mode.

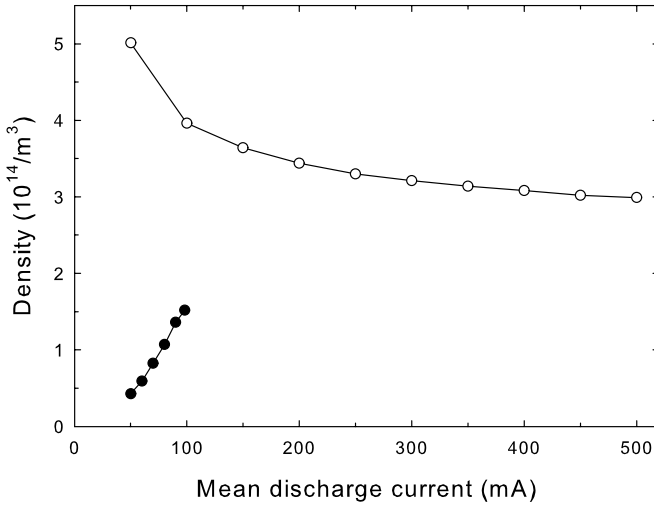


Figure 4. Time-averaged metastable density in (PMD \circ) and HiPIMS (\bullet) discharge versus with mean discharge current. Pulse width 0.1 ms. PMD: pulse frequency 2.5 kHz, duty cycle 25%; HiPIMS: pulse frequency 100 Hz, duty cycle 1%.

1% to ensure that the laser wavelength had not changed during the measurement.

In order to illustrate the influence of the atom temperature on the evaluation of the atom density, we compare in figure 3 the metastable atom densities obtained by making use of the measured time-resolved temperature, the measured time-averaged temperature or the room temperature for the case of (a) pulsed magnetron and (b) HiPIMS discharges with each other. Noted differences are smaller than 30% and, in most cases, less than 15%. Hence, for many applications the time-averaged temperature can be employed to calculate the atom density with acceptable error.

3. Results and discussion

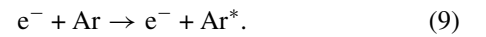
The time-averaged density of metastable argon atoms at a pressure of 4 Pa as a function of the mean discharge current is shown in figure 4. Two sets of measurements are displayed

which were obtained with the PMD and the HiPIMS discharge mode. The time-averaged density displays an opposite behavior in both discharge modes. The metastable density decreases with discharge current in PMD but increases in HiPIMS.

3.1. Argon metastable density

Time-resolved results for the PMD mode are shown in figure 5. Results for a pulse width of 0.1 ms, repetition frequency 2500 Hz (duty cycle 25%), and for three different mean discharge currents (100, 250 and 500 mA) are displayed. The metastable argon density shows a pronounced modulation with time. It monotonically increases during the plasma *on* phase, reaches a maximum shortly after the plasma is switched off, which is followed by a gradual decrease. The modulation is most pronounced for the largest and least pronounced for the smallest mean discharge current. This implies that both the excitation and the de-excitation rate increase with mean discharge current. The cycle-integrated (time-averaged) mean metastable density shows little variation and a decreasing tendency with mean discharge current, see also figure 4.

In order to understand the behavior of the argon metastable density, the relevant excitation and de-excitation channels have to be taken into account. In the plasma *on* phase, the main production mechanism of metastable argon atoms (Ar^*) is direct excitation from the ground state by electron (e^-) impact,



The time evolution of the metastable argon density n_m may be expressed as

$$\frac{dn_m(t)}{dt} = k_1 n_e n_{\text{Ar}} - k_2 n_e n_m \quad (10)$$

where k_1 and k_2 are the reaction rates for excitation and de-excitation, respectively, n_e is the electron density, and n_{Ar} is the argon (gas) density. Equation (10) has the solution

$$n_m(t) = \frac{k_1}{k_2} n_{\text{Ar}} + \left(n_m(0) - \frac{k_1}{k_2} n_{\text{Ar}} \right) \exp(-k_2 n_e t), \quad (11)$$

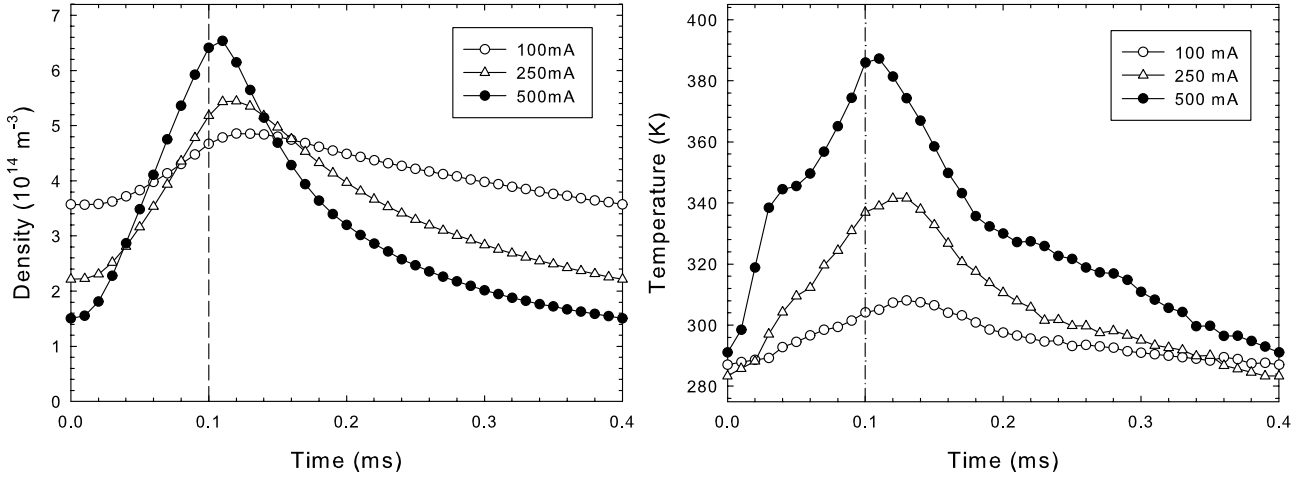


Figure 5. Time-resolved metastable density (left) and temperature (right) in the PMD at different peak (mean) discharge currents: 0.4 A (100 mA, ○), 1 A (250 mA, △) and 2 A (500 mA, ●). Gas pressure 4 Pa, pulse width 0.1 ms, pulse frequency 2.5 kHz, duty cycle 25%, Ti target.

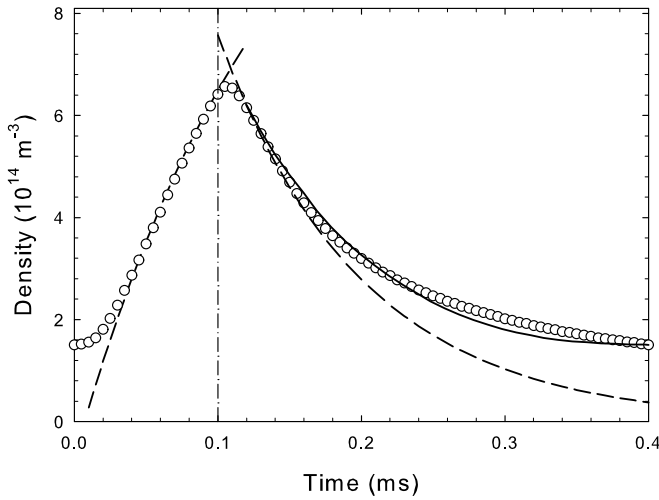


Figure 6. Time-resolved metastable density in the PMD for a peak (mean) discharge current of 2 A (500 mA, ○). Dashed lines correspond to equation (11) with constant excitation and de-excitation rates. The solid line is obtained with a time-dependent de-excitation rate (see text). Gas pressure 4 Pa, pulse width 0.1 ms, pulse frequency 2.5 kHz, duty cycle 25%, Ti target.

where it has been assumed that neither n_e , k_1 , nor k_2 depend on time t . Equation (11) yields a linear increase with time ($\propto k_1 n_{Ar}$) if $k_2 n_m \ll k_1 n_{Ar}$. The predicted time dependence is displayed in figure 6; it agrees reasonably well in the plasma *on* period with the PMD experiment except for some discrepancy in the ignition phase which is taken into account by a delayed onset (delay time 0.025 ms). The fair agreement may be taken as confirmation of a largely time-independent excitation rate $k_1 n_e$. The electron temperature-dependent rate constant k_1 for excitation from the ground state was evaluated from the cross sections given by Khakoo *et al* [28]. We used a time-independent rate constant $k_1 = 9 \times 10^{-11} \text{ cm}^3 \text{ s}^{-1}$ corresponding to an electron temperature $T_e = 3 \text{ eV}$. The approximately linear increase further is an indication that de-excitation is not very significant during the *on* time.

In the afterglow or plasma *off* phase we have $k_1 = 0$ and equation (10) predicts an exponential decay with a time

constant given by k_2 . As is evident from figure 6, the predicted time dependence is in poor agreement with experiment. The discrepancy can be traced back to a time-dependent de-excitation rate k_2 . There are at least three reasons why k_2 is time-dependent. First of all, de-excitation of argon metastables is (partly) due to collisions with electrons which is governed by a reaction rate $k_{dex} = \langle \sigma_{dex} n_e v_e \rangle$. Since both electron density n_e and velocity v_e decrease in the afterglow the de-excitation rate will also decrease. In addition, as the electron density increases the de-excitation rate is faster with increasing discharge current. Secondly, electron ion recombination may enhance the metastable argon density and thereby either slow-down or even invert the decrease in the metastable density (see below). Thirdly, diffusion should lead to a faster decrease in metastable atoms. A simple estimate of the diffusion length Δx based on [1]

$$\Delta x = \sqrt{2Dt} \quad (12)$$

yields $\Delta x \approx 1.4 \text{ cm}$ which is small compared with the plasma dimensions. Here $D = 2.48 \times 10^3 \text{ cm}^2 \text{ s}^{-1}$ is the diffusion coefficient of argon at 4 Pa [29]. Hence, the diffusion time is long in comparison with the pulse period (0.4 ms) and the associated changes due to diffusion of the metastable atom density should be small in the time regime $t \lesssim 0.4 \text{ ms}$.

The solid line in figure 6 represents simulation results with a time-dependent de-excitation rate k_2 [30, 31]. The simulation utilizes time-dependent electron density and temperature derived from experiment [26]. A much better agreement with experiment in the plasma *off* phase is noted. Details of the simulation are given below in connection with our HiPIMS results.

The time-resolved results for the HiPIMS discharge mode are displayed in figures 7 and 8. The argon metastable density is significantly larger compared with the PMD results; it features a double-peak structure where the first maximum occurring during the pulse is followed by a second maximum in the afterglow. Both regimes are well separated from each other. The first maximum during the pulse is caused by electron-impact excitation of argon atoms. In order to explain the decrease in the metastable density already during

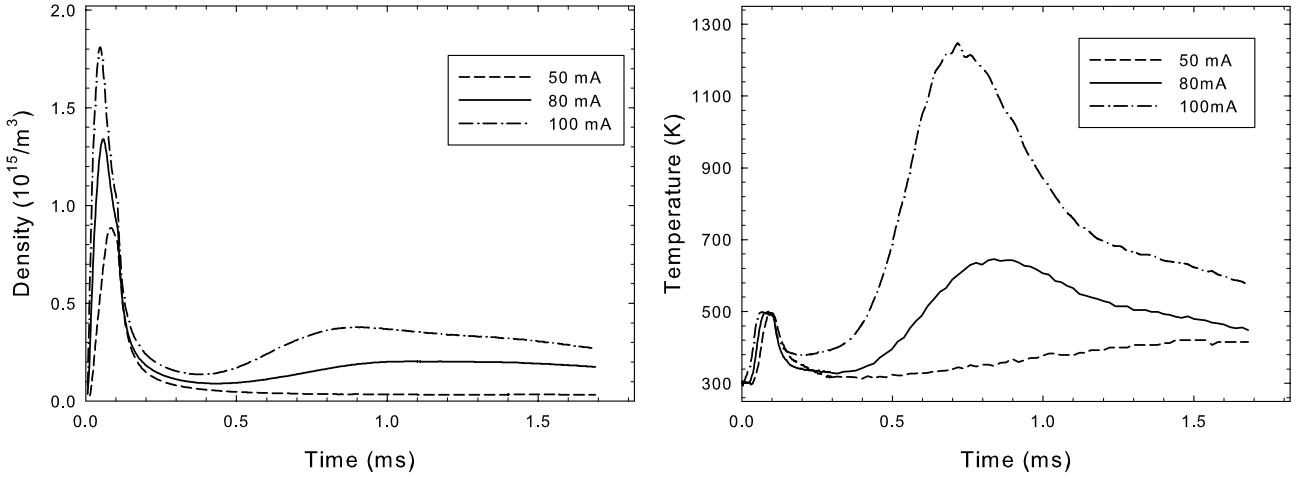


Figure 7. Time-resolved metastable density (left) and temperature (right) in HiPIMS mode at mean (peak) discharge currents of 50 mA (5 A), 80 mA (8 A), and 100 mA (10 A). Gas pressure 4 Pa. Pulse frequency 100 Hz, duty cycle 1%, Ti target.

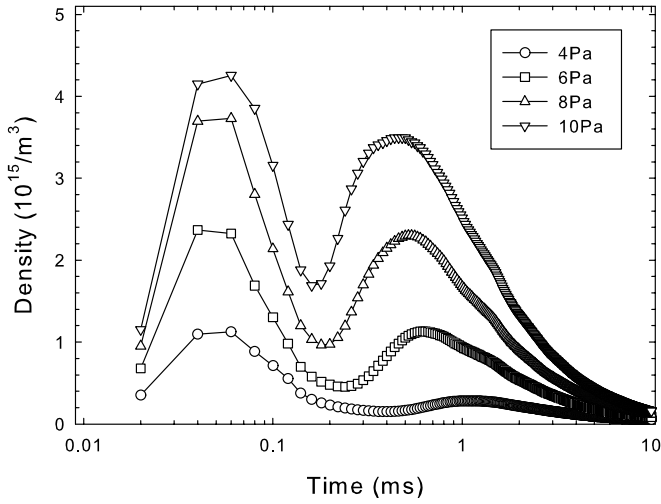


Figure 8. Time-resolved metastable density in HiPIMS mode at different gas pressures. Peak (mean) discharge current 5 A (50 mA). Pulse frequency 100 Hz, duty cycle 1%, Ti target.

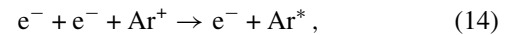
the pulse several processes have been discussed, in particular electron-impact excitation to higher states and electron-impact ionization of metastable argon atoms [25]. In addition one has to take the liberation (sputtering) of titanium atoms into account which may give rise to Penning ionization, leading to the mutual de-excitation of metastable atoms and the ionization of Ti atoms, e.g. $\text{Ar}^* + \text{Ti} \rightarrow \text{Ar} + \text{Ti}^+ + \text{e}^-$ [25]. Here we propose an additional mechanism which could play a role. Previous experiments have shown that an increasing metal atom density leads to a narrowing of the electron density distribution function by depletion of high-energy electrons and thereby to a lower electron temperature [32–36]. It is related to the lower ionization potential of Ti (6.82 eV [27]) compared to Ar (15.76 eV [27]) which requires a lower electron temperature to maintain the discharge at the same discharge current. The position of the first maximum during the pulse thus eventually marks the transition from an argon-burning to a titanium-burning discharge. The transition occurs once a critical Ti density is reached. The time for reaching this

critical density depends on the peak current. As the density of sputtered Ti atoms increases with discharge current, this transition and, hence, the position of the first maximum occurs earlier. As is shown in figure 7, the position of the maximum shifts from 85 μs at a peak current of 5 A to 60 μs and 50 μs for peak currents of 8 A and 10 A, respectively. Other effects such as gas rarefaction [37] resulting in a pronounced variation of the electron temperature may also contribute to the observed decrease in the metastable density. We believe, however, that these effects are not as important here due to the relatively large distance of the observation region from the cathode.

The rapidly decreasing metastable density in the afterglow after the plasma is switched off is largely caused by de-excitation due to electron impact. The following second maximum in the afterglow can be explained by electron-ion recombination either due to dissociative recombination of molecular argon ions



or by three-body recombination



giving rise to the formation of excited argon atoms (Ar^*) which eventually decay to the metastable state [30, 31, 38, 39]. As electron-ion recombination is more likely for *cold* electrons [30, 40, 41], the (roughly exponential) cooling of electrons with a typical time constant of about 100 μs [7, 33] is responsible for the delayed onset of the metastable formation by electron-ion recombination in the afterglow.

The aforementioned effects can be taken into account by a suitable modification of equation (10) which now reads

$$\frac{dn_m(t)}{dt} = k_1 n_e n_{\text{Ar}} - k_2 n_e n_m + k_3 n_e n_r - \frac{D_{\text{Ar}}}{\Lambda^2} n_m + a_m f_{\text{rec}} \quad (15)$$

where $k_1 \simeq 0$ in the afterglow. The dominant loss channel in the afterglow is excitation transfer to energetically nearby states, in particular to the $1s_4$ and $1s_2$ levels, and to the $4p$ -manifold. Excitation transfer from the resonant $1s_4$ state

(density n_r) is taken into account. The electron temperature-dependent rate constants were evaluated from cross sections calculated by Bartschat and Zeeman [42]. Ionization of metastable atoms [43], due to larger energy transfer required, is a relatively unlikely process under the investigated conditions and was not taken into account. Diffusion of metastable argon atoms (diffusion constant $D_{Ar} = 0.992/p \times 10^4 \text{ Pa cm}^2 \text{ s}^{-1}$ [29], where p is the gas pressure, $L \approx 10 \text{ cm}$ is the estimated length of the plasma column, and $\Lambda = L/\pi$) and electron ion recombination are taken into account. In our case of large electron densities the dominant recombination channel is three-body electron–electron–ion recombination (equation (14)) while dissociative recombination (equation (13)) does not play an important role here. The recombination probability [40]

$$f_{\text{rec}} = 2.3 \times 10^{-15} \times \frac{n_e^{2.33}}{T_e^2} \quad (\text{cm}^{-3} \text{ s}^{-1}) \quad (16)$$

with a recombination factor $a_m \simeq 0.075$ was employed in the simulation. Likewise we use

$$f_{\text{rec}} = 1.2 \times 10^{-26} \times \frac{n_e^3}{T_e^{4.5}} \quad (\text{cm}^{-3} \text{ s}^{-1}), \quad (17)$$

which differs by a factor of 2.3 from the original expression [41], and where T_e is the electron temperature in electron-volts (eV). The temporal behavior of the electron number density $n_e(t)$ was taken from the experiment [26]. For the electron temperature $T_e(t)$ we assumed

$$T_e(t) = T_1 \exp(-t/\tau_1) + T_0, \quad (18)$$

with $T_0 = 0.028 \text{ eV}$, $T_1 = 2.0 \text{ eV}$ and $\tau = 0.107 \text{ ms}$.

The rapidly decreasing metastable density is predominantly caused by electron collision-induced excitation transfer to energetically near-by excited states, in particular, to the $1s_4$ and $1s_2$ states. Recent theoretical cross sections [42] were used to evaluate the reaction rate k_2 . Simulation results based on these assumptions are displayed in figure 9 and agree well with experiment.

In addition, simulations were carried out for excitation of the $1s_4$ resonance state of argon. This state has a natural life time of 8.6 ns and can decay by photon emission to the ground state [44]. The temporal behavior of this state's density n_r can be expressed as

$$\frac{dn_r(t)}{dt} = k'_1 n_e n_{Ar} + k'_2 n_e n_m - A \theta n_r - k'_3 n_e n_r - \frac{D_{Ar}}{\Lambda^2} n_r + a_r f_{\text{rec}} \quad (19)$$

where we have $k'_1 \simeq 0$ in the plasma *off* phase. Its time dependence is to a large extent governed by radiative decay being responsible for the rapidly decreasing density during the first 0.3 ms in the afterglow and by excitation transfer to the near-by excited levels including the $1s_5$ metastable state. $A = 1.2 \times 10^8 \text{ s}^{-1}$ [44] is the radiative transition rate, $\theta = 1.1 \times 10^{-4}$ (at 4 Pa) is the escape factor which accounts for the trapping of the emitted resonance light [45], and $a_r \simeq 0.26$.

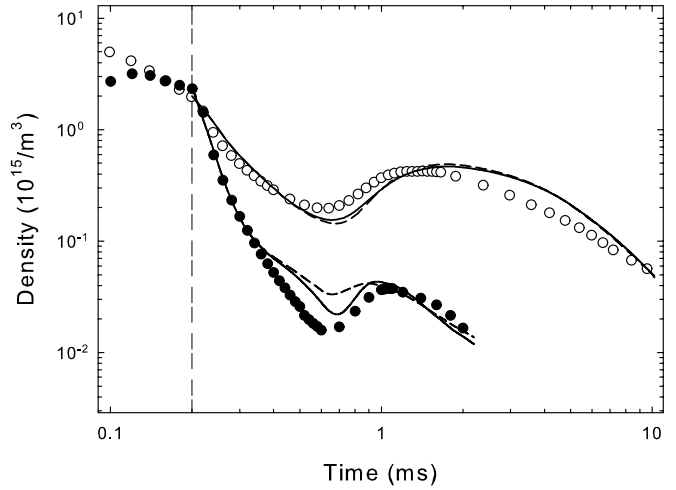


Figure 9. Time-resolved metastable and resonant state density in the HiPIMS discharge. Experimental results for the argon metastable ($1s_5$) and the argon resonance ($1s_4$) states are compared with simulations based on equation (15) employing three-body recombination given by equation (17) (solid lines) or by equation (16) (dashed line). Pulse frequency 100 Hz, pulse width 200 μs , duty cycle 2%, peak discharge current 7.5 A, gas pressure 4 Pa, Ti target.

3.2. Argon metastable temperature

The time-resolved metastable temperature during the PMD is displayed in figure 5. The argon temperature rises during the pulse and decreases in the afterglow. The rising temperature in the plasma *on* phase can be explained by the heating of the plasma due to ions, the energy released by sputtered atoms, and due to fast neutralized argon ions reflected by the cathode. For example, plasma ions lose a certain fraction of their kinetic energy through collisions in the plasma sheath in front of the cathode. The average kinetic energy of a sputtered atom amounts to several eV; this energy is converted by collisions with gas atoms into an increase in the gas temperature. A certain fraction of Ar^+ ions impinging on the cathode may be back-scattered as neutralized atoms in an excited (including a metastable) state [46]. The noted temperature increase during the plasma *on* phase amounts to about 20 K, 50 K and 100 K for peak (mean) discharge currents of 0.4 A (100 mA), 1 A (250 mA), and 2 A (500 mA), respectively, and thus is linearly dependent on the discharge current.

The metastable temperature displays a fast decrease during the plasma *off* phase with a characteristic time of about 0.12 ms. In order to estimate the time evolution of the argon metastable temperature T_m we use

$$\frac{\partial T_m}{\partial t} = -\alpha \frac{\partial^2 T_m}{\partial x^2} \approx -\frac{\alpha}{\Lambda^2} T_m \quad (20)$$

where $\alpha = \lambda_{\text{th}} n^{-1} c_p^{-1}$ is the thermal diffusivity, $\lambda_{\text{th}} = 0.0177 \text{ W (mK)}^{-1}$ is the thermal conductivity of argon at $T = 300 \text{ K}$ [47], n is the gas density, and c_p is the heat capacity. Making use of a constant α the solution of equation (20) is an exponential decay with a time constant given by $\tau = \Lambda^2/\alpha$. Under the present experimental conditions we obtain $\tau \simeq 2.1 \text{ ms}$, which is significantly larger

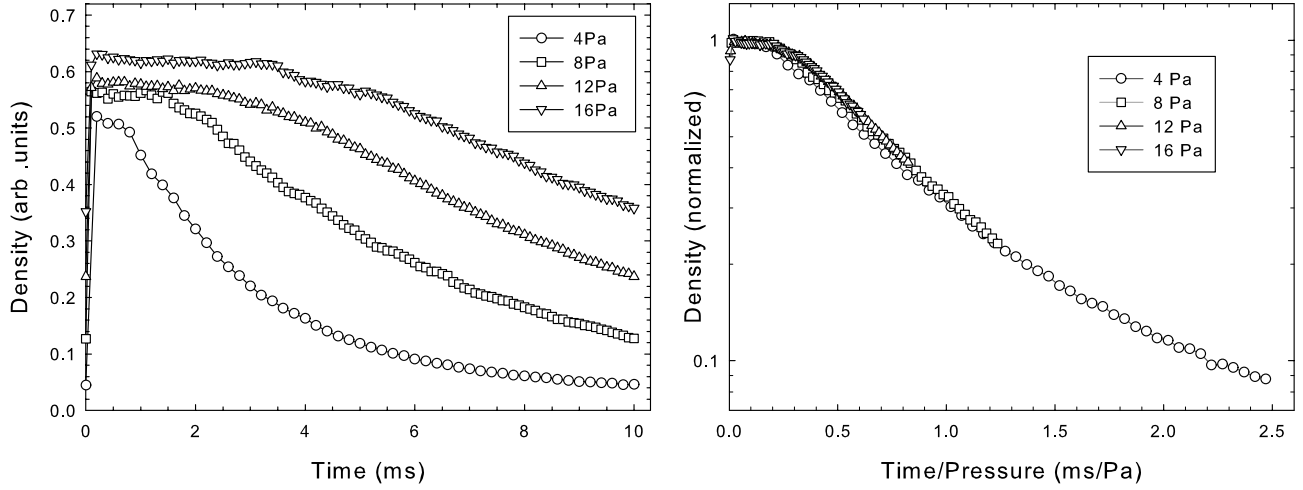


Figure 10. Time-resolved titanium density in the HiPIMS discharge at different pressures of 4, 8, 12 and 16 Pa versus time (left) and versus time divided by pressure (right). Pulse frequency 100 Hz, pulse width 0.2 ms, duty cycle 2%, peak discharge current 7.5 A, Ti target.

than our experimental result of $\tau \approx 0.12$ ms. The large difference can be taken as indication that metastable argon atoms are not in thermal equilibrium with the surrounding gas. For example, fast metastable atoms are likely to be produced by charge exchange of fast reflected argon ions at the cathode or by ion recombination in the gas. If so, the metastable temperature could be larger than the surrounding gas temperature T_g , i.e. $T_m > T_g$. The noted decrease in the metastable atom temperature could be the result of excitation transfer between fast (hot) metastable atoms (Ar_f^*) and slow (cold) ground-state atoms (Ar_s), i.e.



where s and f indicate slow and fast atoms, respectively. This could lead to a much faster temperature decrease than via elastic collisions only. In order to facilitate the observed temperature decrease on a time scale $\tau \approx 0.12$ ms an energy transfer cross section $\sigma_E \gtrsim 2 \times 10^{-20} \text{ m}^2$ is required. Cross sections of this size have been observed in *near-resonant* energy transfer collisions, e.g., in $\text{Ar}^* + \text{Kr}$ collisions, with a cross section $\sigma_E \approx 10^{-20} \text{ m}^2$ [48]. A more than twice as large cross section for the *resonant* energy transfer in $\text{Ar}^* + \text{Ar}$ collisions thus appears realistic.

The time-resolved argon metastable temperature during HiPIMS is displayed in figure 7. The time dependence features a double-peak structure quite similar to the temporal evolution of the metastable density. However, the relative increases are quite different. The temperature displays a moderate increase of about 200 K during the plasma *on* phase followed by a fast decrease in the afterglow and a subsequent pronounced increase whose maximum value and time of appearance strongly depends on the discharge current. The present result is in reasonable agreement with findings of Vitelraru *et al* [25] who observe a pronounced temperature increase to more than 1500 K, albeit on a shorter time scale. Noted quantitative differences are attributed to the different experimental details regarding peak current and distance to the cathode where the measurements were taking place. The first rise correlates with the increase in the Ar metastable density; it is presumably

caused by the heating of the plasma due to ions, fast neutralized argon ions reflected by the cathode, and the energy released by sputtered atoms. It is noted that the metastable temperature similar to the behaviour of the metastable density reaches its maximum of about 500 K already during the pulse. Again, this reflects the transition from an argon-burning to a titanium-burning discharge with a lower electron temperature resulting in a ceasing metastable production. The decreasing temperature at the end of the plasma *on* phase and in the early afterglow follows the decreasing metastable density. Again, the observed temperature decrease is much faster than predicted by equation (20).

The second temperature rise during the afterglow reflects the ion recombination effect. The exact heating mechanism is not clear, however. It appears that ions are not fully thermalized and, as a consequence, the metastable atoms forming from these ions by recombination thus attain a higher temperature compared with the surrounding gas atoms. The subsequent temperature decrease with a time scale of 0.3–0.5 ms is slower than before but still much faster than predicted by equation (20).

3.3. Titanium density

The time-resolved results for the titanium density during the HiPIMS discharge are shown in figure 10. The titanium density displays a steep increase during the pulse and remains approximately constant for several milliseconds after the plasma is switched off. There is a delayed onset of the Ti density which is larger than compared with the Ar metastable case. The delay time amounts to about 40 μs and 60 μs at 4 Pa and 16 Pa, respectively, and thus shows a tendency to increase with gas pressure. As the measurements are performed about 7 cm from the cathode, the delay reflects the propagation of Ti atoms from the cathode to the observation region.

The time evolution of the titanium atom density n_{Ti} may be expressed as

$$\frac{dn_{\text{Ti}}(t)}{dt} = k_{\text{Ti}} - \frac{D_{\text{Ti}}}{\Lambda^2} n_{\text{Ti}} + a_{\text{Ti}} f_{\text{rec}}. \quad (22)$$

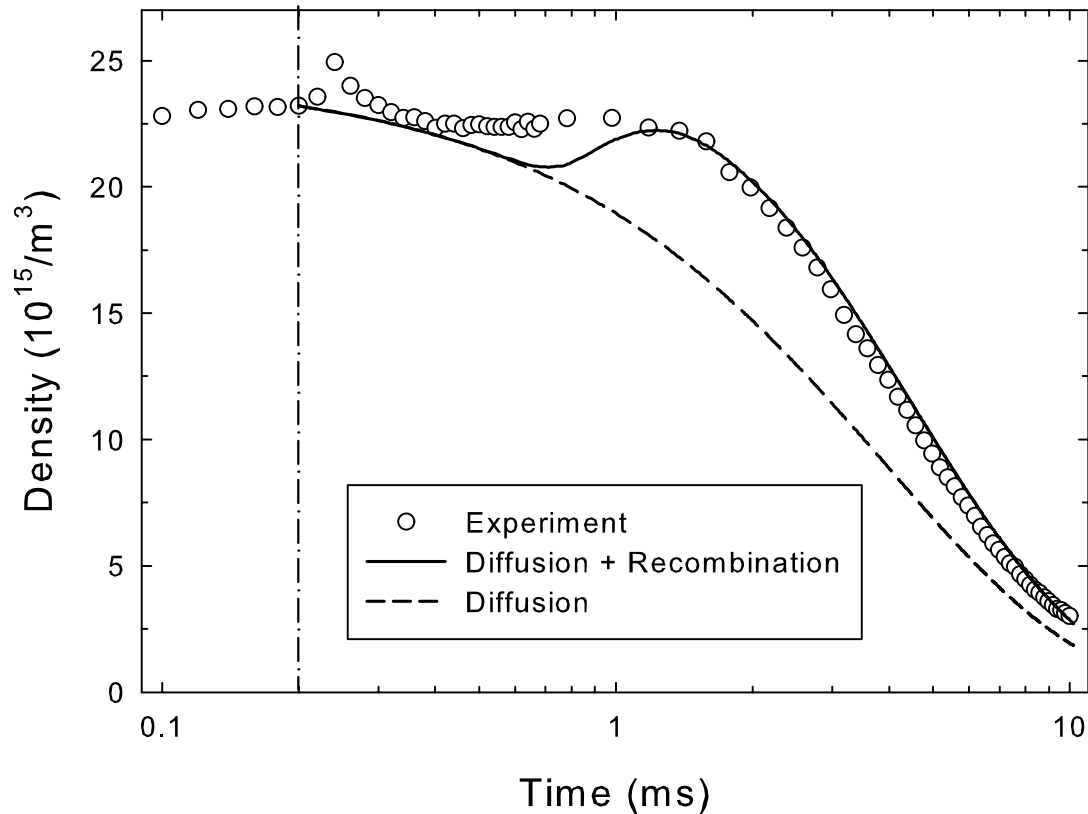


Figure 11. Time-resolved titanium density in the HiPIMS discharge at 4 Pa in comparison with simulations based on equation (22) taking only diffusion (dashed line) and diffusion and recombination into account. Pulse frequency 100 Hz, pulse width 0.2 ms, duty cycle 2%, peak discharge current 7.5 A, Ti target.

For the sake of clarity, only the most important processes are included in the equation. These are the formation of free titanium atoms by sputtering (rate constant k_{Ti}) and by electron-ion recombination (recombination factor $a_{\text{Ti}} = 0.72$), and loss of titanium atoms by diffusion. We made use of a diffusion coefficient $D_{\text{Ti}} = 1.03/p \times 10^4 \text{ Pa cm}^2 \text{ s}^{-1}$ which is close to the diffusion coefficient for Ar but differs by 20% from the diffusion coefficient reported in [49]. In the afterglow $k_{\text{Ti}} = 0$ and only diffusion and recombination processes have to be considered.

Simulation results are displayed in figure 11. Fair agreement with the experimental data is noted. Obviously, a large number of neutral Ti atoms are formed in the afterglow via recombination of Ti^+ ions. Recombination is most pronounced between 0.5 and 1.5 ms when the electron temperature has dropped to small values and the electron density is still high. Afterward, the time evolution of the Ti density is dominated by diffusion. Keeping in mind that the diffusion coefficient D is inversely proportional to the pressure p , it is evident from equation (12) that the diffusion length Δx is a function of time divided by pressure. When plotted in such a fashion, the measured Ti densities at different pressures fall on a universal curve (figure 10).

4. Conclusions

Time-resolved tunable diode laser absorption spectroscopy has been employed to investigate the excited argon atom

density and temperature and titanium atom density in pulsed (PMD, HiPIMS) deposition plasmas. The argon metastable density displays a double-peak structure with a first peak in the plasma *on* phase and a second peak in the afterglow. The measurements reveal the importance of electron-ion recombination processes in the afterglow plasma. Simulations results indicate that three-body recombination and diffusion are the dominant processes in the afterglow plasma. A pronounced increase in the argon metastable temperature in the afterglow is also noted. It is attributed to electron ion recombination.

Acknowledgments

Helpful discussions with Dr V Stranak and Dipl. Phys. S Drache are gratefully acknowledged. The work was supported by the Deutsche Forschungsgemeinschaft through SFB/TR 24 and by the Czech Science Foundation through GACR P205/11/0386 and P108/12/2104.

References

- [1] Kashtanov P V, Smirnov B M and Hippler R 2007 *Phys. Usp.* **50** 455–88
- [2] Anders A 2011 *Surf. Coat. Technol.* **205** S1–9
- [3] Kouznetsov V, Macak K, Schneider J M, Helmersson U and Petrov I 1999 *Surf. Coat. Technol.* **122** 290
- [4] Helmersson U, Lattemann M, Bohlmark J, Ehiasarian A P and Gudmundsson J T 2006 *Thin Solid Films* **513** 1

- [5] Sarakinos K, Alami J and Konstantinidis S 2010 *Surf. Coat. Technol.* **204** 1661
- [6] Ehiasarian A P, Wen J G and Petrov I 2007 *J. Appl. Phys.* **101** 054301
- [7] Stranak V, Drache S, Cada M, Hubicka Z, Tichy M and Hippler R 2011 *Contrib. Plasma Phys.* **51** 237–45
- [8] Gudmundsson J T, Brenning N, Lundin D and Helmersson U 2012 *J. Vac. Sci. Technol. A* **30** 030801
- [9] Samuelsson M, Lundin D, Sarakinos K, Bjorefors F, Walivaara B, Ljungcantz H and Helmersson U 2012 *J. Vac. Sci. Technol. A* **30** 031507
- [10] Stranak V, Wulff H, Bogdanowicz R, Drache S, Hubicka Z, Cada M, Tichy M and Hippler R 2011 *Eur. Phys. J. D* **64** 427–35
- [11] Stranak V, Wulff H, Rebl H, Zietz C, Arndt K, Bogdanowicz R, Nebe B, Bader R, Podbielski A, Hubicka Z and Hippler R 2011 *Mater. Sci. Eng. C* **31** 1512–19
- [12] Tochikubo F, Petrovic Z Lj, Kakuta S, Nakano N and Makabe T 1994 *Japan. J. Appl. Phys.* **33** 4271
- [13] Moshkalyov S M, Steen P G, Gomez S and Graham W 1999 *Appl. Phys. Lett.* **75** 328
- [14] Siefert S, Sands B L and Ganguly B N 2006 *Appl. Phys. Lett.* **89** 011502
- [15] Baguer N, Bogaerts A, Donko Z, Gijbels R and Sadeghi N 2005 *J. Appl. Phys.* **97** 123305
- [16] Vitelaru C, Poucques L de, Minea T M and G Popa 2011 *J. Appl. Phys.* **109** 053307
- [17] Cunge G, Ramos R, Vempaire D, Touzeau M and Sadeghi N 2009 *J. Vac. Sci. Technol. A* **27** 471
- [18] Engeln R, Mazouffre S, Vankan P, Schram D C and Sadeghi N 2001 *Plasma Sources Sci. Technol.* **10** 595
- [19] Clarenbach B, Lorenz B, Kramer M and Sadeghi N 2003 *Plasma Sources Sci. Technol.* **12** 345
- [20] Wolter M, Do H T, Steffen S and Hippler R 2005 *J. Phys. D: Appl. Phys.* **38** 2390–5
- [21] Olejnick J, Do H T, Hubicka Z, Hippler R and Jastrabik L 2006 *Japan. J. Appl. Phys.* **45** 8090–4
- [22] Do H T, Kersten H and Hippler R 2008 *New J. Phys.* **10** 053010
- [23] Do H T, Sushkov V and Hippler R 2009 *New J. Phys.* **11** 033020
- [24] Stefanovic I, Sadeghi N and Winter J 2010 *J. Phys. D: Appl. Phys.* **43** 152003
- [25] Vitelaru C, Lundin D, Stancu G D, Brenning N, Betagne J and Minea T 2012 *Plasma Sources Sci. Technol.* **21** 025010
- [26] Cada M, Hubicka Z, Adamek P, Kluson J and Jastrabik L 2011 *Surf. Coat. Technol.* **205** S317
- [27] Ralchenko Y, Kramida A E, Reader J and NIST ASD Team 2011 *NIST Atomic Spectra Database* (ver. 4.1.0) (Gaithersburg, MD: NIST) <http://physics.nist.gov/asd>
- [28] Khakoo M A *et al* 2004 *J. Phys. B* **37** 247
- [29] Tachibana K 1986 *Phys. Rev. A* **34** 1007
- [30] Bogaerts A 2007 *J. Anal. At. Spectrom.* **22** 502
- [31] Bogaerts A, Gijbels R and Vlcek J 1998 *J. Appl. Phys.* **84** 121
- [32] Hippler R, Wrehde S, Stranak V, Zhigalov O, Steffen H, Tichy M, Quaas M and Wulff H 2005 *Contrib. Plasma Phys.* **45** 348
- [33] Drache S, Stranak V, Herrendorf A-P, Cada M, Hubicka Z, Tichy M and Hippler R 2012 Time-resolved Langmuir probe investigation of hybrid high power impulse magnetron sputtering discharges *Vacuum* *in press*
- [34] Gudmundsson J T, Sigurjonsson P, Larsson P, Lundin D and Helmersson U 2009 *J. Appl. Phys.* **105** 123302
- [35] Ehiasarian A P, Vetushka A, Gonzalvo A Y, Sáfrán G, Székely L and Barna P B 2011 *J. Appl. Phys.* **109** 104314
- [36] Poolcharuansin P and Bradley J W 2010 *Plasma Sources Sci. Technol.* **19** 025010
- [37] Lundin D, Brenning N, Jädernäs D, Larsson P, Wallin E, Lattemann M, Raadu M A and Helmersson U 2009 *Plasma Sources Sci. Technol.* **18** 045008
- [38] Bogaerts A, Gijbels R and Jackson G P 2003 *J. Anal. At. Spectrom.* **18** 533
- [39] Nafarizal N, Takada N and Sasaki K 2008 *J. Phys. D: Appl. Phys.* **41** 035206
- [40] Celik Y, Tsankov Ts V, Aramaki M, Yoshimura Sh, Luggenhölscher D and Czarnetzki U 2012 *Phys. Rev. E* **85** 056401
- [41] Biberman L M, Vorob'ev V S, Vorob'ev V S and Yakubov I T 1987 *Kinetics of Nonequilibrium Low-temperature Plasmas* (New York: Consultants Bureau)
- [42] Bartschat K and Zeman V 1999 *Phys. Rev. A* **59** R2552
- [43] Raadu M A, Axnäs I, Gudmundsson J T, Huo C and Brenning N 2011 *Plasma Sources Sci. Technol.* **20** 065007
- [44] Lawrence G M 1968 *Phys. Rev. A* **175** 40
- [45] Lawler J E and Curry J J 1998 *J. Phys. D: Appl. Phys.* **31** 33235
- [46] Kolev I and Bogaerts A 2008 *J. Appl. Phys.* **104** 093301
- [47] Hoshino T, Mito K, Nagashima A and Miyata M 1986 *Int. J. Thermophys.* **7** 647
- [48] Piper L G, Setser D W and Clyne M A A 1975 *J. Chem. Phys.* **63** 5018
- [49] Ohebsian D, Sadeghi N, Trassy C and Mermet J M 1980 *Opt. Commun.* **32** 81

3.2 Emission spectroscopy of RF discharge

Article II

Application of the escape factor method for determination of excited states densities in a low-pressure argon radio-frequency discharge

Application of the escape factor method for determination of excited states densities in a low-pressure argon radio-frequency discharge

V. P. Sushkov*, H. T. Do, and R. Hippler

Institut für Physik, Ernst-Moritz-Arndt-Universität Greifswald, Felix-Hausdorff-Str. 6, 17489 Greifswald, Germany

Received 06 December 2012, revised 24 April 2013, accepted 25 April 2013

Published online 16 August 2013

Key words Escape factor, rf discharge in argon, metastable state, emission spectroscopy, TDLAS.

Reabsorption of the emitted light in the plasma volume has recently been used for density measurements of the lower level of optical transition by interpretation of emission spectra employing the escape factor concept. Following this idea, we apply this method to a radio-frequency argon discharge. By revising the theoretical background, the impact of different assumptions on excited species spatial distributions is investigated. Comparing with $1s_5$ and $1s_4$ concentrations obtained with laser absorption spectroscopy, the range of applicability of those assumptions is analyzed at different discharge parameters.

© 2013 WILEY-VCH Verlag GmbH & Co. KGaA, Weinheim

1 Introduction

The phenomenon of self-absorption has been known in plasma physics for a long time, see, for example [1] where it was quantified for spectroscopic measurements. The two milestone works [2] and [3] appearing in 1947 laid the foundation for the new approach which is proved to be adequate and successful within a broad range of radiation transport problems. The integro-differential Holstein-Biberman equation coupled to balance equations for excited states allows for a determination of spatial profiles in a self-consistent manner. This was followed by extensive developments in the field, the series of articles by van Trigt [4] being a landmark in the analytical treatment, and the articles by Apruzese [5–7] giving an example of the applied calculations. The concept of *escape factor* came into existence and became well-grounded in terms of the new understanding. To a considerable extent it was summarized and put into order in the works by Irons [8]. The book on radiation trapping [9] published 1998 presents a comprehensive study of the approaches in the field associated with the Holstein-Biberman equation and contains an exhaustive list of the literature.

As soon as a good model describing the interaction of radiation and populations of excited species is available, one can use spectroscopic measurements as a tool to determine the populations. Our study is motivated by our interest to investigate metastable atomic species in argon-containing plasmas.

The role of metastable atoms in noble gas discharges is a subject of considerable research interest due to many reasons. To name only few of them, these atoms have fundamental importance from the point of view of discharge sustaining, kinetics of excited species, and influence on the electron distribution function. In gas mixtures, the collisions with metastables cause large range of reactions, including Penning ionization and chemical transformations. Due to sensitivity to plasma parameters, the population of metastables can be used as a diagnostic tool, for example, indicating the presence of dust particles [10].

The experimental determination of the metastables number density is therefore essential in many issues of practical and theoretical concern. There are several types of optical methods which are commonly used for such measurements. These include laser absorption spectroscopy, broadband absorption, self-absorption, and laser-induced fluorescence [11–13]. The other group of methods is based on interpretation of emission spectra, what can be done in two ways. The first option is to combine the emission spectrum with plasma modeling (for

* Corresponding author. E-mail: sushkov@physik.uni-greifswald.de

example, corona or collisional-radiative model). In this case the outcome depends on the quality of the model and the input rate coefficient data [14]. The other approach is to utilize the reabsorption of emission lines. Description of this phenomenon employs the *escape factor* and does not need any plasma model. It only needs the population of the lower state of corresponding optical transition to be high enough to provide a traceable optical thickness.

The latter approach is in the focus of the present paper. In our work, to a large extent, we follow the procedure recently introduced in the work [15]. In that paper, the column number densities of the four lowest excited states were obtained, but there was no comparison done with other independent method. It was done in the work [16] for the case of pressure dependence in argon and neon ICP discharges. Our modification of the method differences more in form, rather than in fundamental content. A related procedure was also used in [17] for a more specific task to estimate the degree of self-absorption on 811.53 nm argon line. When using a novel technique, the benchmarking by comparison with an independent method is of particular importance. In our work, using TDLAS (tunable diode laser absorption spectroscopy) data as reference, we compare this two methods for the pressure and power dependences in radio-frequency argon discharge. By revising the theoretical background of the escape factor calculation, we make further investigation into the role of assumptions dealing with spatial profiles of the excited species. We provide here useful expressions for some reference cases. A good study on the topic can be found in [18], but we do ours in somewhat different way, simpler but more manageable and not restricted to high opacity asymptotics.

In the next section we revise and summarize the theoretical approach of escape factor calculation tailored to the needs of spectroscopy and consider some application aspects. This is followed by presentation of the experimental set-up and a short description of the TDLAS method. In section 4 both techniques are compared and results are discussed.

2 Method

2.1 Emission spectroscopy

The *reabsorption* of own light is taking place in a discharge when the correspondent optical thickness is not negligible. In the emission spectra this effect makes line intensity I additionally depend on the lower state density n_l of an optical transition. When this dependence is properly quantified, the reabsorption can be utilized to determine the density n_l .

The optical depth of a plasma can be conveniently characterized by the *opacity parameter* $\tau = l k_0 = l n_l \sigma_0$, with l the plasma length, $k_0 = k(\nu_0)$ the absorption coefficient in the line center, and $\sigma_0 = \sigma(\nu_0)$ the corresponding absorption cross-section. the opacity parameter τ is proportional to n_l .

The reabsorption can be accounted for by the *escape factor* $\theta(\tau)$, when for the emission line holds

$$I \propto \theta(\tau) A n_u.$$

A is the Einstein coefficient for spontaneous emission, and n_u is the number density of the upper level. The escape factor takes values in the interval $[0; 1]$. For high opacities θ is close to zero, while in the optically thin regime $\theta \rightarrow 1$.

As is shown hereafter, the ratios of the *escape factors* for different lines can be determined experimentally. From this data, once $\theta(n_l)$ is known as function of n_l , it is possible to deduce the densities of the lower state. The specific relation between θ and n_l depends also on spatial density profiles (both lower and upper levels). This we discuss in detail below.

2.2 The essence of the method

Experimental determination of the escape factors is based on a simple trick. Let us consider two lines with intensities I_1 and I_2 which share a common upper level with density n_u . Then the following relation holds for the intensity ratio I_1/I_2

$$\frac{I_1}{I_2} = \frac{C_1 A_1 n_u \theta_1}{C_2 A_2 n_u \theta_2} = C_{12} \frac{A_1 \theta_1(n_{l1})}{A_2 \theta_2(n_{l2})} \quad (1)$$

$$\frac{\theta_2}{\theta_1} = C_{12} \frac{I_1 A_1}{I_2 A_2}. \quad (2)$$

Line ratio (1) depends on ratios of the respective spontaneous coefficients and escape factors, and on the relative detection efficiency $C_{12} = C_1/C_2$, which accounts for the wavelength dependent transmission of the detection system and the quantum efficiency of the CCD camera. Expression (2) is the basis for determination of escape factors. In practice, one has to consider several such line ratios in order to get the necessary amount of equations. This number has to be no smaller than the total amount of the unknowns, which are actually the densities of the lower states, rather than the escape factors. Then one can solve the equation system by the least-squares minimization procedure.

2.3 The escape factor

Now we outline in brief how we calculate θ as function of n_l .

Treating it as *transmission factor*, averaged over the volume and weighted with the solid angle and emission intensity profile, we start from the general expression for the *transmission factor*

$$T(\rho) = \int_0^\infty E(\nu) \exp(-k(\nu)\rho) d\nu, \quad (3)$$

This quantity shows how much the initial photon flux of spectral content $E(\nu)$ is reduced after having traveled distance ρ through the absorbing medium. We take the emission line shape for function $E(\nu)$. The upper limit of our working pressure range being 25 Pa, we can reasonably assume pure Doppler-broadening for the profiles of emission and absorption lines. On the basis that functions $E(\nu)$ and $k(\nu)$ have exactly the same Gaussian shape they are inserted in the integral (3), and after some transformations and substitution one finally comes to the expression

$$T(\rho) = \frac{1}{k_0 \rho \sqrt{\pi}} \int_0^{k_0 \rho} \frac{\exp(-y)}{\sqrt{\ln(k_0 \rho) - \ln(y)}} dy. \quad (4)$$

For large opacities $k_0 \rho$, one can get from (4) the asymptotic behavior $T(\rho) \approx 1/(k_0 \rho \sqrt{\pi \ln(k_0 \rho)})$ which holds fairly well starting from $k_0 \rho \gtrsim 3$.

2.3.1 Three limiting cases by averaging

We consider systems of cylindrical symmetry with line-of-sight observations in a plane perpendicular to the symmetry axis. All plasma properties depend on the radial coordinate r only (zero at center, R - total radius).

Since local emission is controlled by the upper-state density $n_u(r)$ and absorption - by the lower-state density $n_l(r)$, the result of proper averaging of *transmission factor* depends on the spatial distribution of these states. Emission $E(\nu)$ in expression (3) must be weighted with $n_u(r)$ and the absorption coefficient is now a function of r : $k(\nu, r) = n_l(r) \sigma(\nu)$. To advance further, we carry out the averaging in three important cases, which establish a framework in the current analysis.

Case 1. The intuitively clear 'quick and dirty' approximation would be to set $\rho = R$ and $k_0 = \bar{n}_l \sigma_0$ in the expression (4)

$$\theta_1 \approx T(k_0 R) = \frac{1}{k_0 R \sqrt{\pi}} \int_0^{k_0 R} \frac{\exp(-y)}{\sqrt{\ln(k_0 R) - \ln(y)}} dy, \quad (5)$$

where \bar{n}_l is the line-of-sight average of $n_l(r)$. As shown in the Appendix, this approach corresponds to the case when the upper state is localized at the center and the lower state is spatially uniform.

Case 2. The opposite extreme case, when the lower state atoms are localized at the center and the upper state density is constant in the plane of symmetry, is characterized by the following escape factor (see Appendix)

$$\theta_2 \approx \frac{1}{2}(1 + T(2k_0R)) . \quad (6)$$

This expression does not tend to zero for large optical depth, since the entire absorption takes place in the center, and the light emerging in-between the center and the detector is traveling freely.

Case 3. The shape of the profile is arbitrary, but exactly the same for both the lower and upper states. In this case one arrives at the following expression (see Appendix for details)

$$\theta_3 = \frac{1}{k_0R\sqrt{\pi}} \int_0^{2k_0R} \exp(-y) \sqrt{\ln(2k_0R) - \ln y} dy . \quad (7)$$

Notice that in all those cases the opacity of the whole plasma column is $\tau = 2k_0R$.

In the literature, simple approximation for the escape factor is frequently quoted, coming originally from the work [19]

$$\theta_4(\tau) = \frac{2 - \exp(-10^{-3}\tau)}{1 + \tau} . \quad (8)$$

For $\tau < 10^2$ this reduces to a still simpler function: $\theta(\tau) = 1/(1 + \tau)$.

All these four θ -functions are compared in figure 1. In contrast to typical problems with strong trapping of resonant radiation, our range of interest is rather $\tau \sim 1$ (at our conditions we have $0.03 < \tau < 3$). As can be seen, all the curves converge well at low opacities. The curve for *case 3* and for approximation θ_4 are close to each other over the whole range of opacity shown.

A priori the assumption of *case 3* seems to be the most reasonable. But we will make calculations with other *cases* as well. Since one of our goals is to explore the uncertainty of the model imposed by the freedom in choosing one or another spatial profile, we use *cases 1* and *2* as extremes which point at the limits of this freedom.

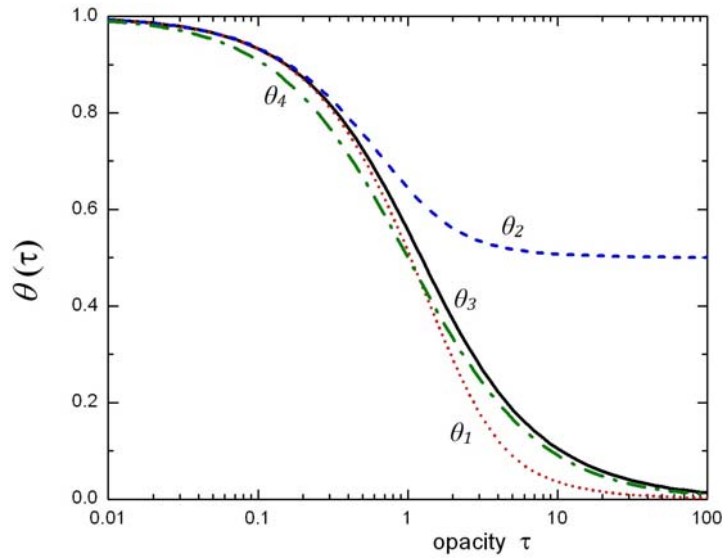


Fig. 1 Escape factor, calculated using expression (7) - solid line, (5)- dotted line, (6) - dashed line, and (8) - dashed-dotted.

2.3.2 Temperature dependence

Temperature T of the excited species is one of the parameters in the model. This temperature is not expected to differ much from that of the background gas. Anyway, it's experimental value was readily available from the

analysis of the TDLAS absorption profiles. In most cases it did not display perceptible variations, so a fixed value T_0 was assumed then for such model calculations. But the results can be easily temperature-corrected if multiplied by the factor $\sqrt{T/T_0}$. This square-root dependence can be demonstrated using equation (12):

$$n = \frac{\tau}{2R\sigma_0} \propto \Delta\nu \propto \sqrt{T} \quad (9)$$

In our experiments the change in temperature of excited species was significant for higher discharge powers, the whole variation ranging from 320 K to 410 K. This gives maximal difference of $\approx 5\%$ to the curve, calculated with average constant temperature (350 K). The corresponding results presented below are temperature-corrected. At our conditions the effect of temperature variation is weaker than that of different *cases* for spatial profiles.

2.4 Application of the method

The relevant excited states and the optical transition used are shown in figure 2a. Throughout our paper we use Paschen's notation to identify atomic energy levels. From the total of 30 lines of the 2p-1s transitions array (Table 1) we chose 10 lines and built up 6 ratios (some of the lines entering more than in 1 ratio). For the sake of completeness, we decided also to include transitions involving $1s_2$ and $1s_3$ levels.

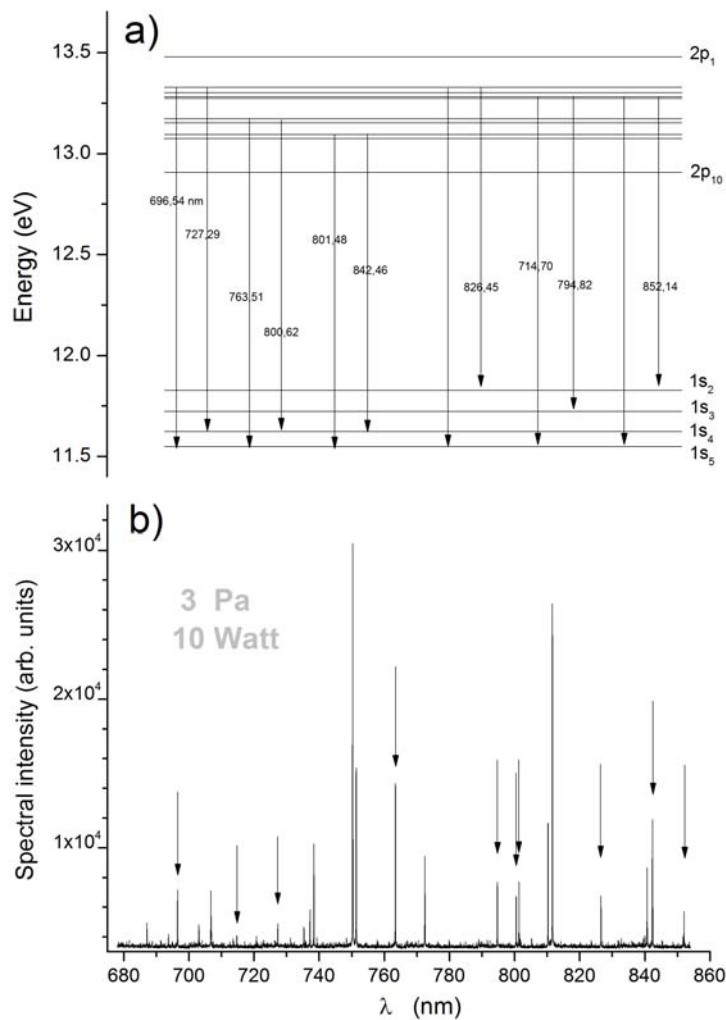


Fig. 2 The optical transitions of 1s - 2p array in argon: a) energy diagram of relevant atomic levels and the pairs of transitions used in the present study, and b) an example of the raw spectrum data, with arrows marking the lines.

Table 1 List of $1s - 2p$ transitions in argon atom. Data is taken from [20], for the line 857.81 nm from [21]. The **notes** column tells whether the line was used (+); if not, shortly describes the reason ('out' meaning out of our spectrograph's range, " $2p_i$ out" meaning that the potential pair line is out of range etc.).

wavelength λ , nm	states lower – upper	probability A , $10^7 s^{-1}$	stat. weight $g_l - g_u$	notes
667.73	$1s_4 - 2p_1$	0.236	3 – 1	out
696.54	$1s_5 - 2p_2$	0.639	5 – 3	+
706.72	$1s_5 - 2p_3$	0.38	5 – 5	unresolved
714.70	$1s_5 - 2p_4$	0.0625	5 – 3	+
727.29	$1s_4 - 2p_2$	0.183	3 – 3	+
738.40	$1s_4 - 2p_3$	0.847	3 – 5	used
747.12	$1s_4 - 2p_4$	0.0022	3 – 3	too weak
750.39	$1s_2 - 2p_1$	4.45	3 – 1	$2p_1$ out
751.47	$1s_4 - 2p_5$	4.02	3 – 1	no pair
763.51	$1s_5 - 2p_6$	2.45	5 – 5	+
772.38	$1s_5 - 2p_7$	0.518	5 – 3	unresolved
772.42	$1s_3 - 2p_2$	1.17	1 – 3	unresolved
794.82	$1s_3 - 2p_4$	1.86	1 – 3	+
800.62	$1s_4 - 2p_6$	0.49	3 – 5	+
801.48	$1s_5 - 2p_8$	0.928	5 – 5	+
810.37	$1s_4 - 2p_7$	2.5	3 – 3	$2p_7$ out
811.53	$1s_5 - 2p_9$	3.31	5 – 7	no pair
826.45	$1s_2 - 2p_2$	1.53	3 – 3	+
840.82	$1s_2 - 2p_3$	2.23	3 – 5	not used
842.46	$1s_4 - 2p_8$	2.15	3 – 5	+
852.14	$1s_2 - 2p_4$	1.39	3 – 3	+
857.81	$1s_4 - 2p_5$	<0.0001	3 – 1	too weak
866.79	$1s_3 - 2p_7$	0.243	1 – 3	out
912.30	$1s_5 - 2p_{10}$	1.89	5 – 3	out
922.45	$1s_2 - 2p_6$	0.503	3 – 5	out
935.42	$1s_2 - 2p_7$	0.106	3 – 3	out
965.78	$1s_4 - 2p_{10}$	0.543	3 – 3	out
978.45	$1s_2 - 2p_8$	0.147	3 – 5	out
1047.00	$1s_3 - 2p_{10}$	0.098	1 – 3	out
1148.80	$1s_2 - 2p_{10}$	0.019	3 – 3	out

In the end, there are 4 variables n_{1s_j} with j from 2 through 5, corresponding to the number densities of all $1s$ - excited states. The argument of θ -function is of the form $\tau = \sigma_0 2R n_{1s_j}$. The relation (2) tells that the corresponding ratios of θ -factors and line intensities are correlated through the C_{12} constant, which stands for all the effects of the spectrometric device itself. In order to circumvent it, we opt for an additional measurement under the conditions of extremely low opacity. In this case $\theta_{1,2} = 1$ and $I_2^0/I_1^0 = C_{12} A_1/A_2$. Deviding a line ratio I_1/I_2 from a regular measurement by I_1^0/I_2^0 , we directly arrive at the experimental value for the escape factors ratio

$$\frac{I_1/I_2}{I_1^0/I_2^0} = \frac{\theta_2}{\theta_1} . \quad (10)$$

A set of six θ -ratios corresponds to the set of the model functions ratios $\theta_2(\sigma_2 2R n_{1s_j})/\theta_1(\sigma_1 2R n_{1s_m})$ calculated with one of the expressions (5-8); that way by minimizing the sum

$$\sum_{k=1}^6 \left[\left(\frac{I_1/I_2}{I_1^0/I_2^0} \right)_k - \left(\frac{\theta_2(\sigma_2 2R n_{1s_j})}{\theta_1(\sigma_1 2R n_{1s_m})} \right)_k \right]^2 \quad (11)$$

the values of the four variables n_{1s_j} are determined.

In order to reduce the population of the lower excited states and thus providing conditions of low opacity we added some oxygen to the argon gas. Oxygen like other molecular impurities acts as an effective quenching-agent for the excited states involved. By a gradual increase of the oxygen influx the line ratios were observed to stabilize typically at 3-4 sccm of the oxygen flow (by 20 sccm of argon), remaining fairly stable during the course of its further increasing. Such a behavior evidently marks the regime of the low opacity, and this "saturation" value was taken as I_1^0/I_2^0 . All measurements have been carried out with the same spectrograph settings to ensure that C_{12} remains unchanged.

The optical cross-section is taken in the form

$$\sigma_0 = \frac{1}{8\pi} \lambda_0^2 A \frac{g_u}{g_l} \frac{1}{\sqrt{\pi} \Delta\nu}, \quad (12)$$

where λ_0 is the transition wavelength, g_u and g_l is the degeneracy of corresponding level, and $\Delta\nu$ is the Doppler linewidth given by $\Delta\nu = \nu_0 \sqrt{2k_b T / m_a c^2}$.

A representative sample of the argon-discharge emission spectra is shown in figure 2b with arrows pointing at the relevant lines.

3 Experiment

The experiments were performed in the PULVA reactor [10, 22], see figure 3. It's main part is a vacuum chamber of 40 cm diameter. The capacitively-coupled discharge was driven at 13.56 MHz by a radio frequency (rf-generator) connected to the bottom electrode by a matching network. The bottom electrode has a diameter of 13 cm and is situated near the center of the chamber; the chamber wall serves as the other electrode.

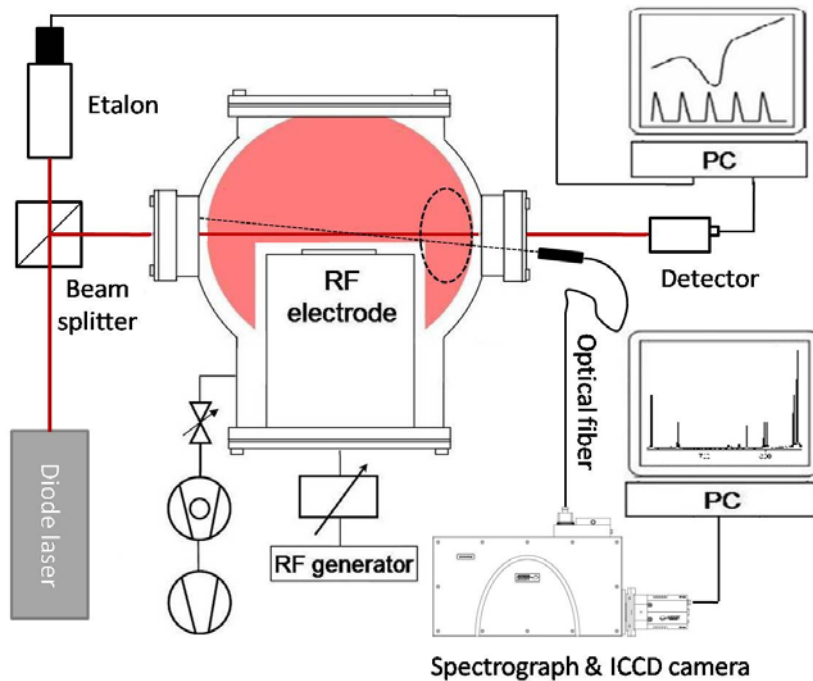


Fig. 3 Experimental setup.

The optical emission spectroscopy (OES) system makes use of the Shamrock-500 spectrograph with Andor Istar ICCD camera. The emission lines were collected by optical fiber with line of sight perpendicular to the laser beam and at a height of 2.5 ± 0.5 cm which is the same as for the diode laser. The collection solid angle $\Delta\Omega$ is based on the opening angle of $0.6/11.5 \approx 0.05$ radian.

The absorption coefficient $k(\nu)$ was measured with standard application of the TDLAS technique [10], and then the line-of-sight average density n_a and temperature T are calculated by fitting the data with Gauss absorption line. Here we use the $1s_5 - 2p_9$ and $1s_4 - 2p_7$ transitions to measure respectively the metastable and the resonant state densities. An experimentally acquired absorption line with a corresponding Doppler-broadened fit is given in figure 4.

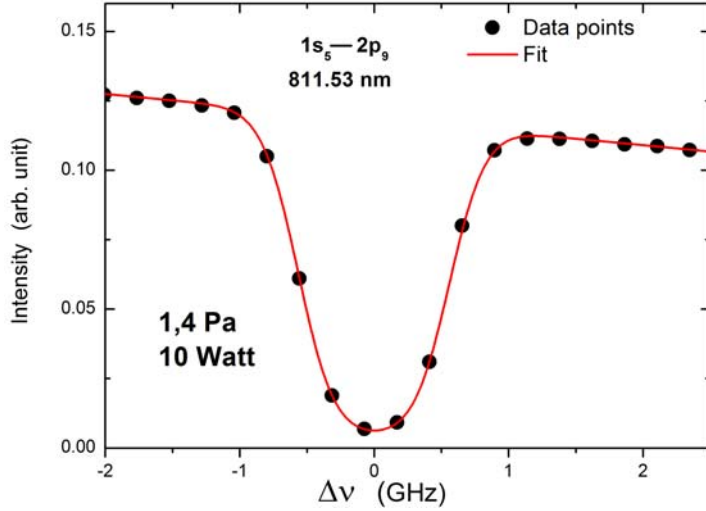


Fig. 4 An example of the TDLAS-measured data points and the fit for the 811.53 nm line, used to determine the metastables' number density.

We also checked that the laser saturation does not distort the results. By the dominant Doppler line-broadening, the apparent absorption coefficient $\tilde{k}(\nu)$ is related to the laser intensity I_L as following [23]:

$$\tilde{k}(\nu) = \frac{k(\nu)}{\sqrt{1 + I_L/I_L^S}}, \quad \tilde{k}(\nu)^{-2} = k(\nu)^{-2}(1 + I_L/I_L^S) \quad (13)$$

where I_L^S is the so-called *saturation intensity*. The metastable and resonant densities shown later in this work have been measured by TDLAS at $I_L \leq 0.1 I_L^S$. The measured k , therefore, has an error smaller than 5%.

4 Results and Discussions

We performed our measurements at different discharge powers and pressures. In figure 5 we compare pressure dependencies for metastable $1s_5$ (a) and resonant $1s_4$ (b) states, obtained with OES (four lines with symbols, corresponding to $\theta_1, \dots, \theta_4$) and TDLAS (solid line) techniques. A good agreement for both states is observed. For *case 3* the agreement at lower pressures (up to ~ 10 Pa) is excellent, whereas at higher pressures the TDLAS curves show a tendency of bending downwards while the OES results do not, giving rise to discrepancy by a factor of 2 at pressure ≥ 20 Pa.

Some discrepancies can be explained by impact of the assumed *case* for the spatial distributions. The comparison of the results is suggestive of profiles' variation with pressure. At lower pressures the assumption of equal shapes (*case 3*) works good. With increasing pressure the distributions are changing at different speeds, so that other *cases* now match better. Though *case 2* renders fine results for the metastable density, it completely fails for the resonance state. This numerical artefact is obviously due to the fact that expression (6) for θ_2 does not tend to zero and thus does not cover the whole range of necessary θ -values.

Since there is no reference data for comparison, results for the other two excited species $1s_2$ and $1s_3$ are not included in the figure. The number density of the $1s_3$ level is ≈ 7 times smaller than that of the $1s_5$ -state which seems reasonable as $1s_3$ -state has a five time smaller statistical weight. The density of the resonant $1s_2$ -state is 2-3 times lower than that of $1s_4$ -state. They have the same degeneracy, and the lifetime of $1s_2$ is 4 times shorter.

Power-dependent number densities are presented in figure 5(c,d). For both excited species the best agreement is achieved with the equal profiles assumption, *case 3*. At lower power the agreement is particularly good, while

at higher power the values here are somewhat lower than the reference data. This may be explained by the distribution of the upper level becoming relatively broader. However, it's hard to judge for certain.

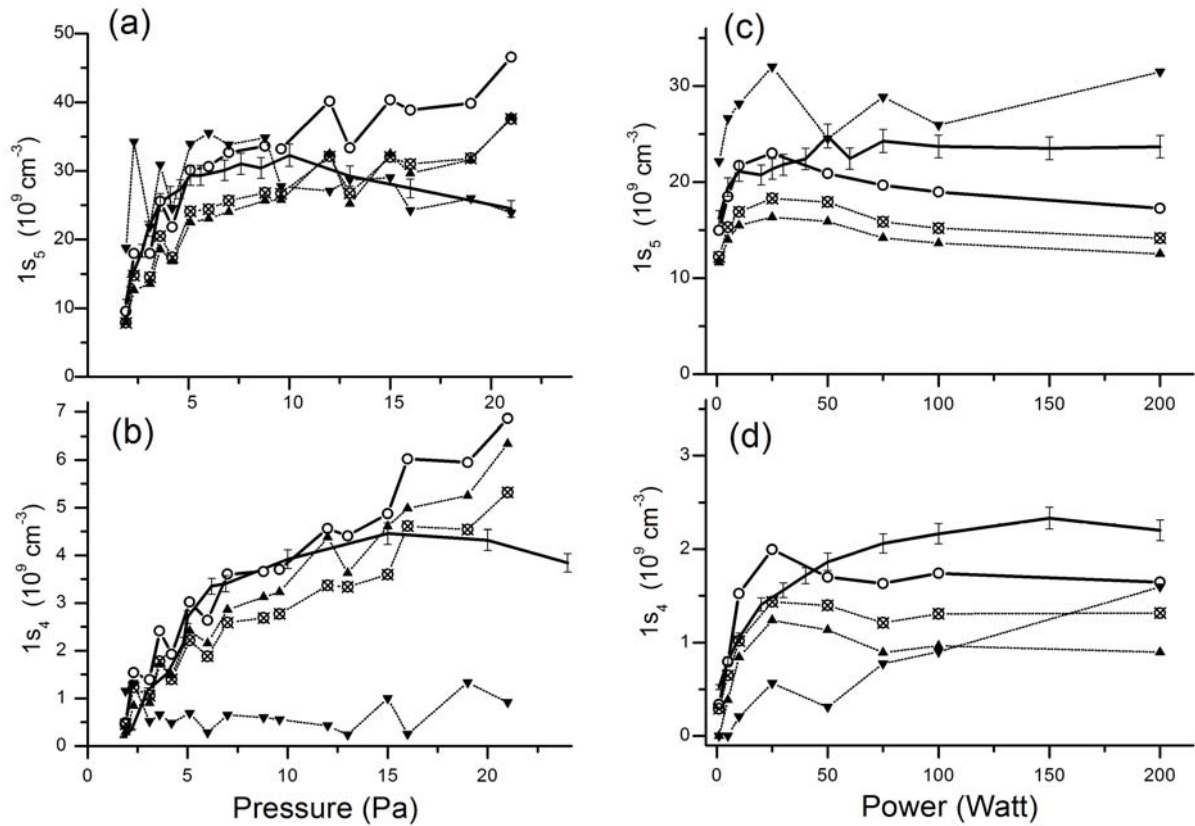


Fig. 5 Number density of excited species vs. pressure (a,b) at a constant power of 10 W and vs. power (c,d) at a pressure of 3 Pa. Plots (a) and (c) show results for $1s_5$ -state, (b) and (d) - for $1s_4$ -state. Solid line with error bars represents TDLAS data; open circles \circ stand for case 3 (Eq. 7), triangles \blacktriangle - case 1 (Eq. 5), \blacktriangledown - case 2 (Eq. 6) and \otimes plots (Eq. 8).

All in all, the application of escape factor in the form (7) reproduce the reference data for both species with better than 30% accuracy. To be noted, the agreement with θ_4 is not quite as good but still reasonably well. The values for $1s_3$ metastable state density are 5–6 times smaller than for $1s_5$ -state. The $1s_2$ concentration is closer to the $1s_4$ data than in the case of pressure dependence.

5 Conclusions

We have shown in this work, that the escape factor method can be used to determine the number densities of some excited species, which are the lower levels of the corresponding optical transitions, from emission spectra. We have compared densities of $1s_4$ and $1s_5$ states in the argon radio-frequency discharge with those obtained by TDLAS technique. Different assumptions on spatial distribution of excited species have been tested. It was shown that the assumption of equal profiles shape gives generally good agreement, especially at lower discharge powers and pressures. Formula (8) also yields reasonable results.

This method is more flexible and cheaper as compared with TDLAS, and readily applicable to various other species. It is anyway a good option when no TDLAS device is available.

Appendix: calculation of the escape factor

In this Appendix we are going to prove formulas (5) (6) and (7) by proper averaging the transmission factor $T(r)$.

We take here different zero point as in the main article. The detector is on a plasma boundary $r_d = 0$ (this does not restrict the generality of the result), the axis of cylindrical symmetry is at $r = R$, and the other plasma boundary is at $r = 2R$. The detector collects light perpendicular to the axis from the solid angle Ω , which is small enough to neglect the axial variation of the plasma properties within the volume spanned by this angle.

As an elementary volume we consider a circular segment of the observation cone, with cross-sectional area $S = \Omega r^2$ and thickness dr . The photon flux from this volume is $I(r)dV = An_u(r)\Omega r^2 dr$. The flux, which reaches the unit detector area, must be reduced by the factor $\frac{1}{r^2}$. As a result, the contribution of the elementary volume to the total intensity will be $An_u(r)\Omega dr$. Then we have to calculate the following relation:

$$\theta = \frac{\int_0^{2R} An_u(r)\Omega T(r)dr}{\int_0^{2R} An_u(r)\Omega dr} = \frac{\int_0^{2R} n_u(r)T(r)dr}{\int_0^{2R} n_u(r)dr} = \int_0^{2R} n_u^n(r)T(r)dr. \quad (14)$$

We take the radial profiles of the levels involved in the form: $n_i(r) = \bar{n}_i \cdot 2R \cdot n_i^n(r)$, where index i marks u (upper level) or l (lower level), $n_i^n(r)$ is the normalized profile with $\int_0^{2R} n_i^n(r)dr = 1$ and $\bar{n}_i = \frac{\int_0^{2R} n_i(r)dr}{2R}$ is the line-of-sight average of the corresponding level density. With $k_0 = \bar{n}_l\sigma_0$, the transmission factor is:

$$T(r) = \frac{1}{\sqrt{\pi}k_0 2R \int_0^r n_l^n(r')dr'} \int_0^{k_0 2R \int_0^r n_l^n(r')dr'} \frac{\exp(-y)dy}{\sqrt{\ln(k_0 2R \int_0^r n_l^n(r')dr') - \ln(y)}}. \quad (15)$$

In the following we consider three different assumptions concerning the profiles.

(i) If $n_u^n(r) = \delta(r - R)$ and $n_l^n(r) = \text{const} = R/2$, then from the last term in (14) we immediately arrive at expression (5).

(ii) In the opposite limiting case with $n_u^n(r) = \text{const} = 1/2R$ and $n_l^n(r) = \delta(r - R)$, one has to calculate $\theta = \frac{1}{2R} \int_0^{2R} T(r)dr$. Since $T(r) = 1$ for $0 < r < R$ and $T(r) = T(2k_0R)$ for $2R > r > R$, then

$$\frac{1}{2R} \int_0^{2R} T(r)dr = \frac{1}{2R}(R + RT(2k_0R)) = \frac{1}{2}(1 + T(2k_0R)).$$

(iii) In our last case under consideration, we assume that $n_u^n(r) = n_l^n(r) \equiv n(r)$. Then combination of expressions (14) and (15) yields the double integral to be evaluated:

$$\theta = \frac{1}{\sqrt{\pi}} \int_{r=0}^{2R} \frac{n(r)}{2k_0R \int_0^r n(r')dr'} \int_{y=0}^{k_0 2R \int_0^r n(r')dr'} \frac{\exp(-y)dy}{\sqrt{\ln(k_0 2R \int_0^r n(r')dr') - \ln(y)}} dr.$$

Noticing that $n(r)dr = d(\int_0^r n(r')dr')$ and introducing the new variable $u = 2k_0R(\int_0^r n(r')dr')$, we get:

$$\theta = \frac{1}{\sqrt{\pi}2k_0R} \int_{u=0}^{2k_0R} \int_{y=0}^u \frac{\exp(-y)dy du}{u\sqrt{\ln u - \ln y}} = \frac{1}{\sqrt{\pi}2k_0R} \int_{y=0}^{2k_0R} \int_{u=y}^{2k_0R} \frac{\exp(-y) d(\ln u) dy}{\sqrt{\ln u - \ln y}}.$$

Here after the second equality sign the order of integration was changed, taking also into account the boundaries of integration domain. Now the inner integration can be accomplished, and setting $s = \ln u$ we bring our proof

to the end:

$$\begin{aligned}
 \frac{1}{\sqrt{\pi} 2k_0 R} \int_{y=0}^{2k_0 R} \int_{s=\ln y}^{\ln 2k_0 R} \frac{\exp(-y) ds dy}{\sqrt{s - \ln y}} &= \\
 &= \frac{1}{\sqrt{\pi} k_0 R} \int_{y=0}^{2k_0 R} \exp(-y) dy \sqrt{s - \ln y} \Big|_{s=\ln y}^{s=\ln 2k_0 R} \\
 &= \frac{1}{\sqrt{\pi} k_0 R} \int_0^{2k_0 R} \exp(-y) \sqrt{\ln(2k_0 R) - \ln y} dy,
 \end{aligned}$$

where the last term is equivalent to expression (7).

Acknowledgements This work was supported by the Deutsche Forschungsgemeinschaft through SFB/TR 24 and by the National Foundation for Science and Technology Development (NAFOSTED), Vietnam, under project number 103.05-2012.20.

References

- [1] R. Ladenburg and S. Levy, *Zeitschrift für Physik* **65**, 189-206 (1930).
- [2] T. Holstein, *Phys. Rev.* **72**, 1212 (1947).
- [3] L.M. Biberman, *Zh. Eksp. Teor. Fiz.* **17**, 416-32 (1947).
- [4] C. Van Trigt, *Phys. Rev.* **181**, 97-114 (1969); *Phys. Rev. A* **1**, 1298-1314 (1970); *Phys. Rev. A* **4**, 1303-1316 (1971); *Phys. Rev. A* **13**, 726-733 (1975).
- [5] J.P. Apruzese, J. Davis, D. Duston, and K.G. Whitney, *J. Quant. Spectrosc. Radiat. Transfer* **23**, 479-487 (1980).
- [6] J.P. Apruzese, *J. Quant. Spectrosc. Radiat. Transfer* **25**, 419-425 (1981).
- [7] J.P. Apruzese, *J. Quant. Spectrosc. Radiat. Transfer* **34**, 447-452 (1985).
- [8] S.F. Irons, *J. Quant. Spectrosc. Radiat. Transfer* **22**, 1-20 (1979); *ibid.* **22**, 21-36; *ibid.* **22**, 37-44.
- [9] A.F. Molisch and B.P. Oehry: *Radiation Trapping in Atomic Vapours* (Oxford: Clarendon Press 1998).
- [10] H.T. Do, V. Sushkov, and R. Hippler, *New J. Phys.* **11**, 033020 (2009).
- [11] Z. Gavare, D. Gött, A.V. Pipa, J. Röpcke, and A. Skudra, *Plasma Sources Sci. Technol.* **15**, 391-395 (2006).
- [12] B.K. McMillin and M.R. Zachariah, *J. Appl. Phys.* **77**, 5538 (1995).
- [13] M. Tadokoro, H. Hirata, N. Nakano, Z.L. Petrović, and T. Makabe, *Phys. Rev. E* **58**, 7823 (1998).
- [14] D. Mariotti, Y. Shimizu, T. Sasaki, and N. Koshizaki, *Appl. Phys. Letters* **89**, 201502 (2006).
- [15] M. Schulze, A. Yanguas-Gil, A. von Keudell, and P. Awakowicz, *J. Phys. D: Appl. Phys.* **41**, 065206 (2008).
- [16] J.B. Boffard, R.O. Jung, C.C. Lin, and A.E. Wendt, *Plasma Sources Sci. Technol.* **18**, 035017 (2009).
- [17] C. Scharwitz and T. Makabe, *J. Appl. Phys.* **106**, 113304 (2009).
- [18] N.N. Bezuglov, A.N. Klucharev, A.F. Molisch, M. Allegrini, F. Fusco, and T. Stacewicz, *Phys. Rev. E* **55**, 3333-3350 (1997).
- [19] R. Mewe, *Brit. J. Appl. Phys.* **18**, 107 (1967).
- [20] Yu. Ralchenko, A.E. Kramida, J. Reader, and NIST ASD Team (2010). NIST Atomic Spectra Database (version 4.0), [Online]. Available: <http://physics.nist.gov/asd> [Tuesday, 17-May-2011 08:45:37 EDT]. National Institute of Standards and Technology, Gaithersburg, MD.
- [21] W.L. Wiese, J.W. Brault, K. Danzmann, V. Helbig, and M. Kock, *Phys. Rev. A* **39**, 2461 (1989).
- [22] H.T. Do, H. Kersten, and R. Hippler, *New J. Phys.* **10**, 053010 (2008).
- [23] W. Demtröder: *Laserspektroskopie* (Berlin: Springer 2000).

3.3 Fast video recording of a dust particle in a RF sheath

3.3.1 Sheath simulations

The simulations were based on the formulas and equations of Sec.2.2.2 and have been done in the Mathcad environment.

Levitating above the electrode, bigger particles have their equilibrium position deeper in the sheath, smaller are closer to the sheath-plasma boundary. By observation the smallest particles we estimated the thickness of our sheath to be $d = 1.1$ cm. For the electrons density we adopted $n_e(0) = 2 \cdot 10^9 \text{ cm}^{-3}$ and for their temperature $kT_e = 3$ eV. In our experiment the negative bias voltage was observed to be -300 V, the value $V_{dc} = -315$ V which we used was slightly higher in magnitude because in the model it refers to the plasma bulk, not to the ground potential. The electric field was assumed to be a linear function of x (the relevance of parabolic sheath potential was shown, for example, in [53]).

At the pressure of 3.5 Pa the free path of argon ions is $\lambda_i \approx 0.15$ cm what makes the sheath to be collisional $d/\lambda_i \sim 7$, although not highly collisional. This is why we have to resort Exp.2.15. The simulated curves of $n_e(x)$ and $n_i(x)$ are shown in Fig.3.3 a). In the collisionless ballistic limit the energy of ions arriving at the cathode would be $m_i u_i^{\lambda_i=\infty}(d)^2/2 = eV_{dc} = 315$ eV. Due to the effect of collisions the average energy of the ions is reduced to $m_i u_i(d)^2/2 \approx 20$ eV.

The effect of the secondary electrons is visualized in Fig.3.3 b) which shows the floating potentials calculated with/without including the corresponding term. The inclusion of the secondaries makes the potential observably weaker. Starting from a marginal difference of less than 5% at the sheath-presheath boundary, it gradually increases up to the difference of factor two at the cathode surface.

The presented sheath model was essentially used in **Article III** and **Article IV** at explaining the particle's behavior. In parallel to it **Article II** includes also the results of an other ccp-discharge model. This model have been realized by my co-authors and used the PIC-MCC code for kinetic treatment of all plasma particles. It gave detailed information on plasma components, its accuracy being limited only by some fine points associated with 1D modeling of the asymmetric discharge. It provided a good cross-reference check for my model described in the present work.

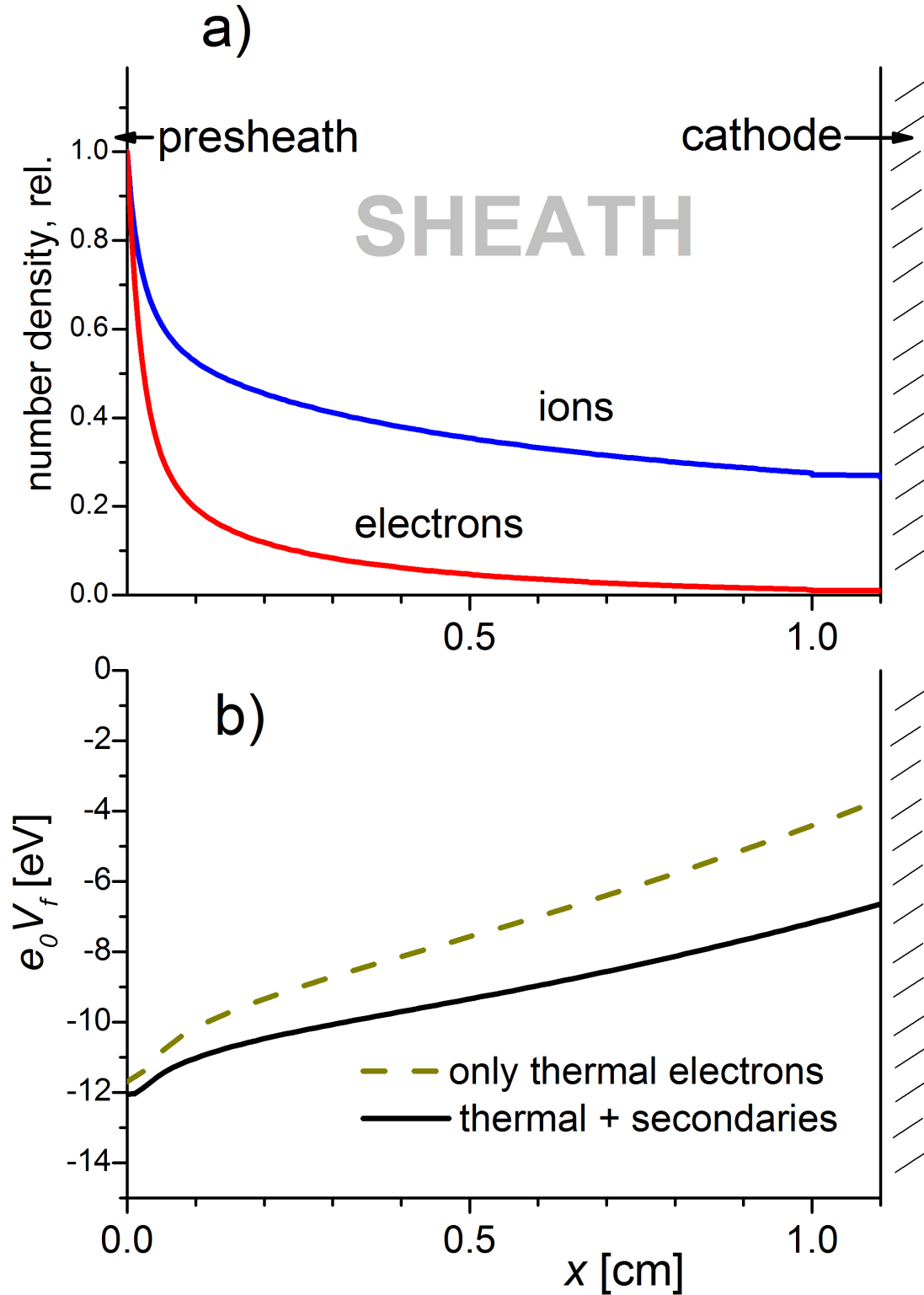


Figure 3.3: Simulated quantities in the sheath:

- a) spatial profiles of electron $n_e(x)/n_e(0)$ and ion $n_i(x)/n_i(0)$ densities, normalized to the boundary value, and
- b) the floating potential $V_f(x)$.

Article III

Behavior of a porous particle in a radiofrequency
plasma under pulsed argon ion beam bombardment

Behavior of a porous particle in a radiofrequency plasma under pulsed argon ion beam bombardment

Ruben Wiese^{1,2}, Vladimir Sushkov¹, Holger Kersten³,
Venkata R Ikkurthi¹, Ralf Schneider⁴ and Rainer Hippler^{1,5}

¹ Institut für Physik, Ernst-Moritz-Arndt-Universität Greifswald,
Felix-Hausdorff-Strasse 6, 17489 Greifswald, Germany

² Institut für Plasmaforschung und Technologie, Felix-Hausdorff-Strasse 2,
17489 Greifswald, Germany

³ Institut für Experimentelle und Angewandte Physik, Universität Kiel, Kiel,
Germany

⁴ Max-Planck-Institut für Plasmaphysik, EURATOM Association,
Wendelsteinstrasse 1, 17491 Greifswald, Germany

E-mail: hippler@physik.uni-greifswald.de

New Journal of Physics **12** (2010) 033036 (19pp)

Received 14 September 2009

Published 23 March 2010

Online at <http://www.njp.org/>

doi:10.1088/1367-2630/12/3/033036

Abstract. The behavior of a single porous particle with a diameter of $250\ \mu\text{m}$ levitating in a radiofrequency (RF) plasma under pulsed argon ion beam bombardment was investigated. The motion of the particle under the action of the ion beam was observed to be an oscillatory motion. The Fourier-analyzed motion is dominated by the excitation frequency of the pulsed ion beam and odd higher harmonics, which peak near the resonance frequency. The appearance of even harmonics is explained by a variation of the particles' charge depending on its position in the plasma sheath. The Fourier analysis also allows a discussion of neutral and ion forces. The particle's charge was derived and compared with theoretical estimates based on the orbital motion-limited (OML) model using also a numerical simulation of the RF discharge. The derived particle's charge is about 7–15 times larger than predicted by the theoretical models. This difference is attributed to the porous structure of the particle.

⁵ Author to whom any correspondence should be addressed.

Contents

1. Introduction	2
2. Experimental setup	3
3. RF plasma simulation	5
4. Results and discussion	7
4.1. Particle's charge	9
4.2. Neutral drag force	12
4.3. Ion drag force	12
4.4. Particle de-charging	13
4.5. Fourier frequency spectrum	14
5. Conclusion	17
Acknowledgments	18
References	18

1. Introduction

During the last decade, interest in so-called *dusty (complex) plasmas* has increased enormously [1]–[3]. Particles are systematically generated in process plasmas for special applications in materials research, metallurgy, and medicine, or their properties are changed in the plasma [4]. Particles are also used to determine plasma parameters, like electric field strength, energy transport or the density of charge carriers. The background of many of these applications is the specific behavior of powder particles in a radiofrequency (RF) plasma. When particles are inserted into a plasma, they become negatively charged due to the larger mobility of electrons compared to ions. For particles with a diameter of several $10\ \mu\text{m}$, this charge can become as large as several 100 000 elementary charges [6]. Because of their charge, the particles are sensitive to electric fields. While the gravitational force acting on a sufficiently massive particle tends to pull the particle out of the plasma, the electric field in the plasma sheath above a negatively self-biased RF electrode repels the negatively charged particle and thus acts in the opposite direction. Under certain conditions, i.e. for particles with diameters in the μm regime, the particle encounters a balance between upward (electric) and downward (gravitation) forces and levitates in the sheath region above the electrode. A detailed description of the interaction of these and other forces can be found elsewhere [4, 5], [7]–[9].

So far, particles levitating in a plasma sheath have been manipulated, e.g., with an electric probe [10], with the help of laser beams [11], by time-varying electric fields of an adaptive electrode [12] and by periodic variation of the bias voltage [13]. Once the motion parameters like resonance frequency of the particles or their relative position with respect to the sheath are known, several plasma properties, like sheath thickness and the shape and strength of the electric field in the sheath, and/or particle properties like charge or mass can be determined [14].

In the present experiment, we investigate the interaction of an external ion beam with a particle levitating in an RF plasma sheath. The interaction of an ion compared to a laser beam offers the advantage that at the same beam power a larger momentum can be transferred to the particle [15]. For that purpose, a particle trapped in the sheath was exposed to a pulsed ion beam with known intensity and energy and was thereby excited to an oscillatory motion. A detailed

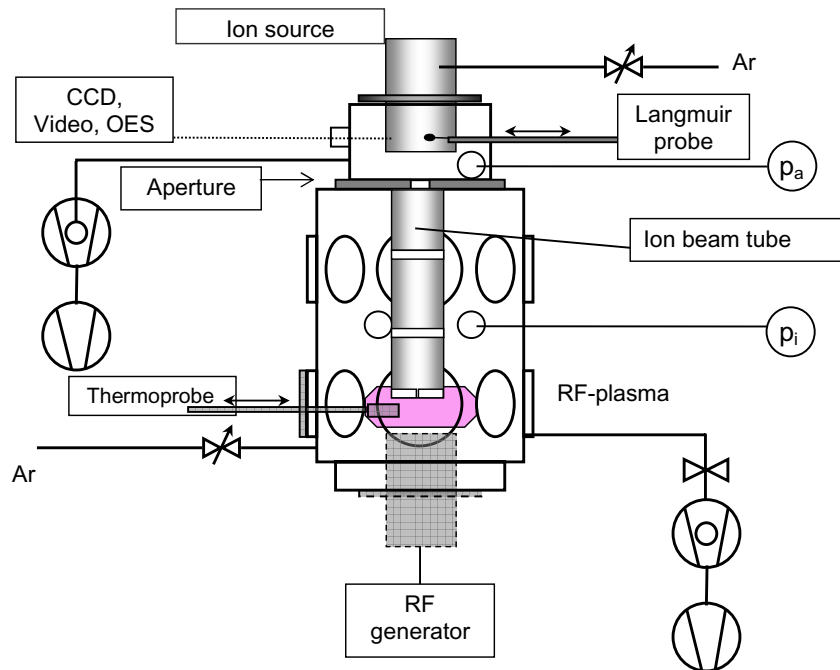


Figure 1. Schematic setup of the PULVA II reactor [15].

analysis of the particle's motion was carried out from which the Fourier frequency spectrum was obtained, which allowed for a discussion of neutral and ion drag forces. The use of a non-spherical porous particle is of interest for a number of applications including technological environments [16], flaking of wall materials in fusion devices [17] and other irregularly shaped objects like spacecraft [18].

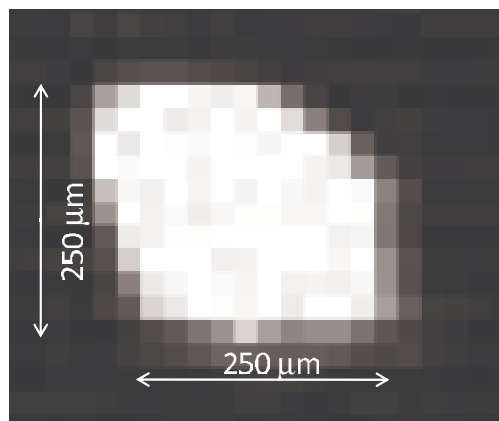
2. Experimental setup

The experiments are carried out in the PULVA II reactor [15]. It consists of a cylindrical reactor with a diameter of 400 mm (figure 1) and pumped with the help of a 500 l s^{-1} turbomolecular pump to a residual gas pressure of less than 10^{-4} Pa. The effective pumping speed is varied by an adjustable butterfly valve. Argon gas has been admitted by a gas flow controller (MKS) with a flow rate of 30 sccm, yielding a typical operation pressure of 3.5 Pa. An RF discharge is maintained inside the chamber with the help of a planar electrode (diameter 130 mm) located at the bottom of the reactor chamber and driven via a matching network (Dressler VM700) by an RF generator (Dressler Cesar 1310) at 13.56 MHz and with a power of 10 W. Typical plasma parameters are given in table 1.

A vertically expanded laser beam (wavelength 532 nm and power 2 W) is employed for particle illumination. The particle position is recorded through a glass window at 90° with respect to the ion beam and through a narrow filter (530 nm). Two cameras, a reflex camera (Nikon D70) with a focal length of 24–120 mm and a high-speed camera (Nikon FastCam PCI R2) with a frame rate of 125 pictures per second, have been employed. The recorded video sequences are analyzed with a self-written program that calculates the particle's coordinates as a function of time and transfers the particle's positions in chronological order to a spreadsheet.

Table 1. Selected experimental parameters.

Plasma density	$1.5 \times 10^{15} \text{ m}^{-3}$
Plasma potential	+15 V
Electron temperature	3 eV
Self-bias potential	−300 V
Ion beam energy	800 eV
Ion beam flux density	$75 \mu\text{A cm}^{-2}$
Particle diameter	$250 \mu\text{m}$
Particle mass	$6.9 \mu\text{g}$

**Figure 2.** Recorded particle image (1 pixel corresponds to $23 \mu\text{m}$).

Particles are introduced into the plasma with the help of a sieve that is manipulated from the outside. We used SiO_2 powder particles (density 2.2 g cm^{-3}) with a diameter of $0.8 \mu\text{m}$. In addition, the powder contained large agglomerates with sizes of up to about $300 \mu\text{m}$. After several attempts, one lone particle was located in the sheath and its motion was recorded by the camera. The isolated particle displayed in figure 2 was used for the measurements reported below. The particle size of the used agglomerate was estimated at a (mean) diameter of $25 \mu\text{m}$.

In order to estimate the particle's mass m , we performed a series of *ex situ* measurements employing a set of 40 different particles. Particle sizes were measured with a Keyence VHX-100 K digital microscope equipped with a VH-Z100 objective (magnification $\times 100 - 1000$), employing a digital camera with 2.11×10^6 pixels. The particle mass was measured with a Sartorius SC2 microbalance with a capacity of 2.1 g and a resolution of $0.1 \mu\text{g}$. Figure 3 displays mass versus mean radius r of the 40 investigated particles. The results closely follow a power law $m = 1.5 \times 10^{-5} r^{2.7}$, where m and r are given in μg and μm , respectively. For a mean particle radius of $125 \mu\text{m}$, we get $m = 6.9 \mu\text{g}$, which will be used in the following. It corresponds to a packing density of 38%, which is about half of the maximum close packing density of a face-centered cubic crystal (74%) [19]. The result shows that the particle has a porous structure.

In order to investigate the particle's behavior under the influence of an ion beam, an ion source, EC/A 125 (IOM Leipzig), located at a vacuum port opposite to the RF electrode, is

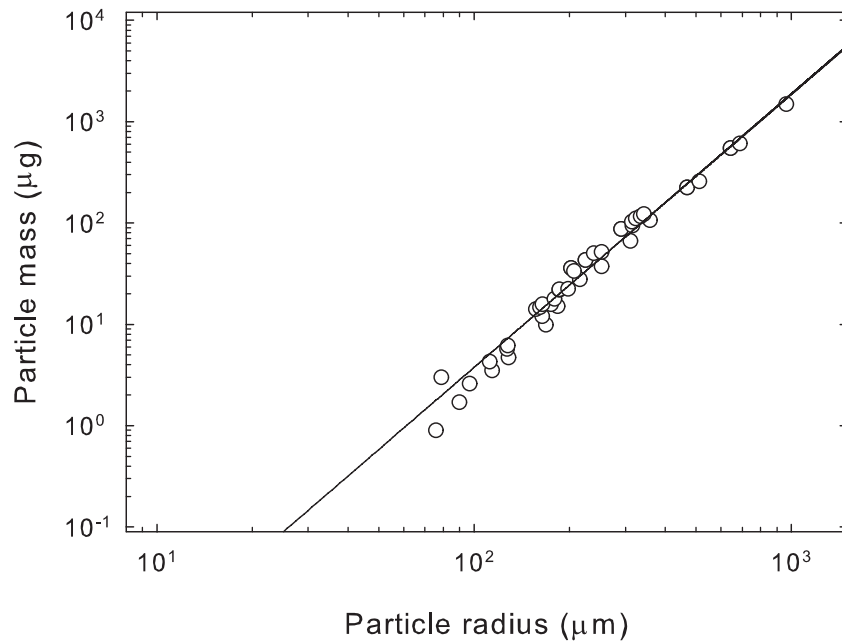


Figure 3. Particle mass m versus mean particle radius r . The solid line corresponds to $m = 1.5 \times 10^{-5} r^{2.7}$.

directed downward to the agglomerated particle that is confined in the sheath in front of the RF electrode. The ion beam is guided by a stainless steel tube with an inner diameter of 7.5 cm and leaving the tube through a grounded plate with a center orifice of 0.5 cm (see figure 1). The ion source is operated with a gas flow of 8 sccm argon at a pressure of 0.06 Pa, maintained by a separate turbo pump (Leybold) with a pumping speed of 1500 l s^{-1} . For pulsed operation, the ion source is driven with a square wave voltage in the frequency range 0.1–8 Hz and with a duty cycle of 1:1.

3. RF plasma simulation

We have performed a numerical simulation of the RF discharge in order to model the discharge characteristics. A one-dimensional (1D) model of the RF discharge is used, which is expected to provide rather realistic plasma parameters of the RF plasma sheath as long as the dust particle is placed close to the central axial discharge region and still is computationally treatable on a single CPU on a standard PC. By using the experimentally known time-dependent bias voltages, the model represents quite well the dynamics of the potential, densities and velocities of all species [20, 21]. The simulation yields discharge parameters such as temperature, plasma potential, velocity and density of plasma species (Ar^+ , e^-) at various positions in the discharge including the dust particle location. The computational tool uses a particle-in-cell with Monte Carlo collisions (PIC-MCC) code and allows for a kinetic treatment of all plasma particles [22]–[25]. The kinetics of ‘super particles’ representing many real particles moving in self-consistent fields discretized on a grid are followed. The collisions between particles are modeled using a binary Coulomb collision model described in [23, 25], and MCC models are used for other types of collisions. The PIC code allows us to self-consistently resolve the whole plasma including the electrostatic sheath in front of the material wall.

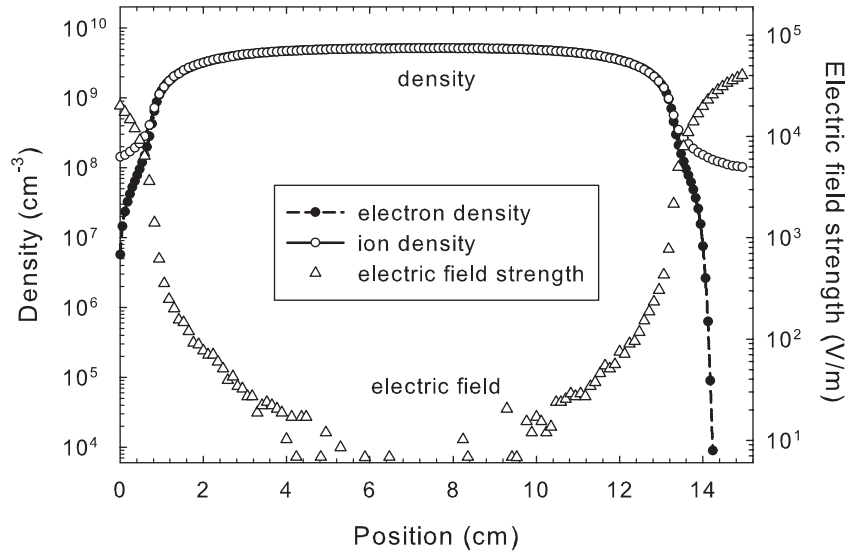


Figure 4. Simulated electron (●) and ion (○) density versus position. The figure also shows the outward directed electric field strength $|E|$. Note that the electric field strength \vec{E} crosses zero and changes sign near the plasma center.

The parameters of the simulation were chosen to reasonably resemble the essential features of the experiment. In the simulation, a parallel plate reactor with a separation of 15 cm between the electrodes was employed. The powered electrode was placed at a position $z = 15$ cm with the grounded electrode at $z = 0$ cm. The RF voltage applied to the powered electrode is given by $U_{\text{RF}} = U_{\text{bias}} + U_0 \sin(\omega t)$, where $U_{\text{bias}} = -300$ V and $U_0 \approx 315$ V. This means that the simulations take into account the asymmetric behavior of the discharge. The collisions included for the current study are Coulomb, elastic and inelastic collisions between the various plasma species [24].

The calculated discharge characteristics are typical for a collisionless RF discharge. Figures 4 and 5 display the calculated (electron and ion) densities and the corresponding energies, respectively, in the axial direction between the electrodes. Obviously, electron and ion densities are equal in the discharge center but strongly deviate in the sheath regions near the electrodes.

The simulated time-averaged plasma potential and the derived electric field strength are displayed in figure 6. The plasma potential is zero at the grounded electrode (at $z = 0$ cm) and drops to -300 V at the powered electrode (at $z = 15$ cm); it attains a large positive value of $\approx +90$ V in the plasma center. The latter value deviates from the experimental plasma potential of $+15$ V.

The computed sheath width at the powered and the grounded electrode is 1.8 and 0.8 cm, respectively. The simulated electric field strength as derived from the variation of the plasma potential is also shown in figure 6. It yields an outward (towards the electrodes) directed electric field \vec{E} which is zero near the plasma center, where it changes sign. The electric field in the sheath region accelerates ions towards the electrodes while electrons are repelled. This is reflected in the energy distribution of both ions (which become supersonic in the sheath) and electrons (figure 5).

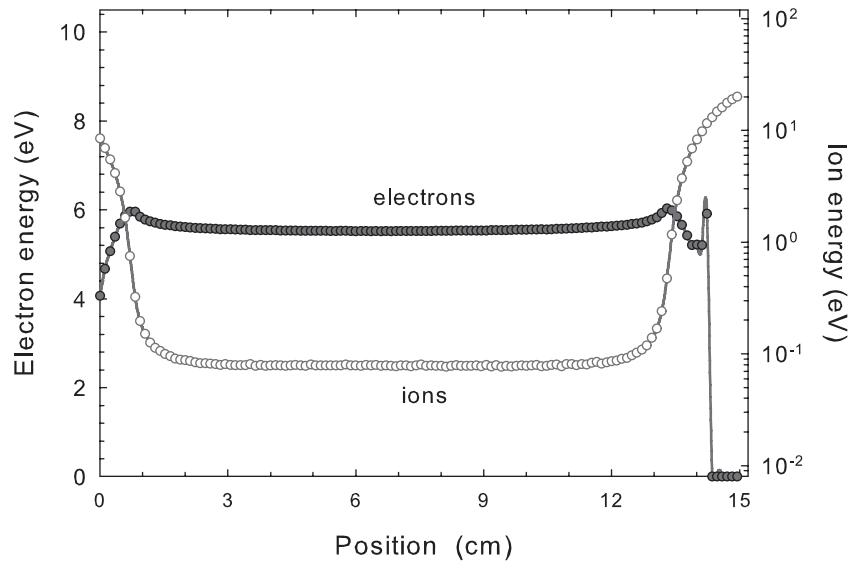


Figure 5. Simulated electron (●) and ion (○) energy versus position.

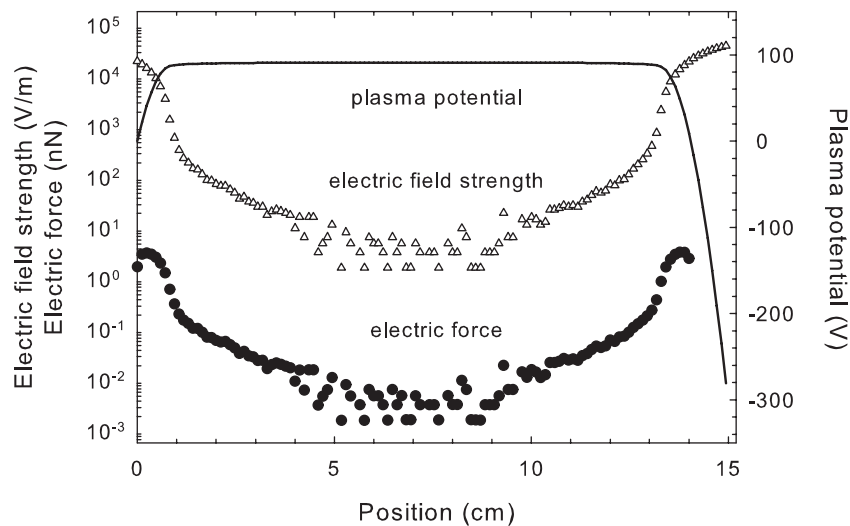


Figure 6. Simulated plasma potential (solid line), electric field strength (Δ) and electric force acting on the particle (●) versus position.

4. Results and discussion

The particle motion under the influence of a square wave-modulated ion beam with a beam energy of 800 eV and a modulation frequency of 0.5 Hz is displayed in figure 7. By interaction with the ion beam (*on* period), the trapped particles are displaced from their original position and start to oscillate around a new equilibrium position. During the ion beam *off* period, the particle resumes to its initial equilibrium position where it continues to oscillate. At this low excitation frequency, the particle oscillates with a frequency close to its eigen or resonance frequency superimposed on the modulation frequency of the ion beam.

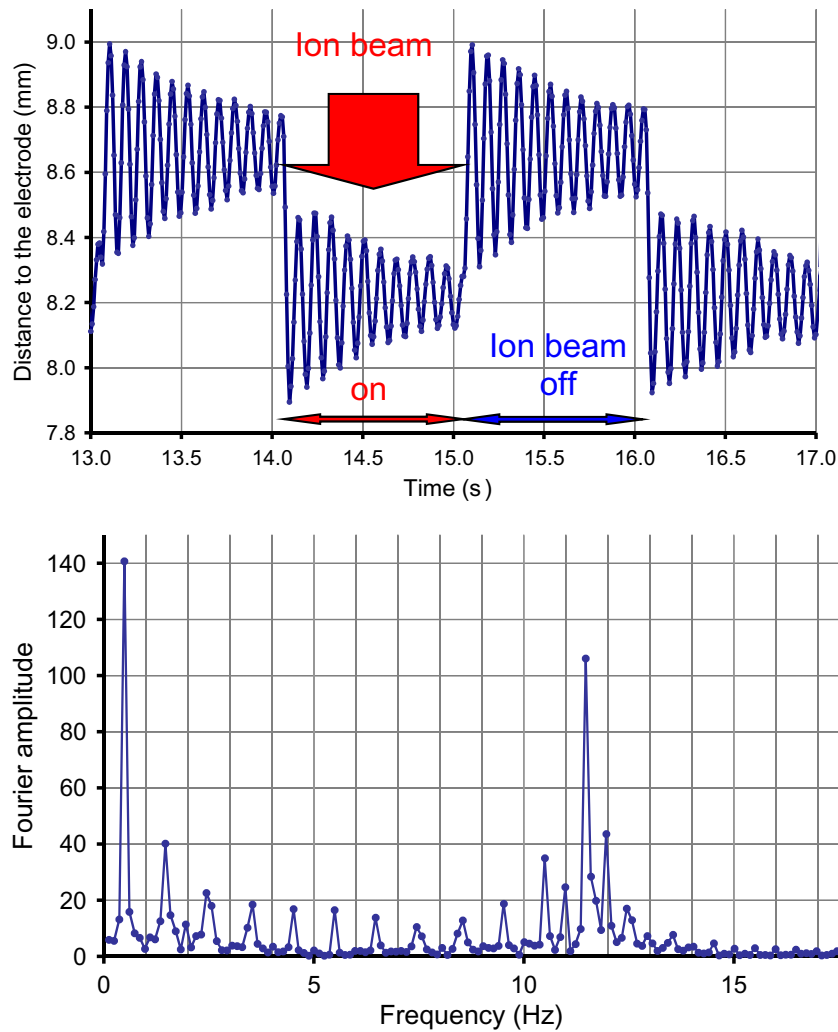


Figure 7. Top: particle position following ion beam excitation at 0.5 Hz. Bottom: experimental Fourier coefficients derived from the particle's movement.

The chronological course of the particle's movement was evaluated and a Fourier analysis was carried out in order to determine the particle's frequency spectrum. The deduced frequency spectrum (figure 7) shows two major components: the excitation frequency ($\nu_a = 0.5$ Hz) of the ion beam and an enhancement in the Fourier spectrum at the resonance frequency $\nu_r \approx 11.3$ Hz of the particle in the plasma. The Fourier spectrum also contains odd higher harmonics, while even harmonics, except in the neighborhood of the resonance frequency, are suppressed. For the particle oscillation, the back driving force is the difference between the field force, generated by the electric field in the sheath, and the gravitation force on the particle. Since the electric field has an almost linear dependence with distance, the particle's motion resembles that of a linear oscillator. The approximate linearity of the electric field, based on the parabolic shape of the potential, has been asserted, e.g., by Tomme *et al.*, who carried out investigations with oscillating particles and showed that over a distance of 20% of the sheath thickness, the divergence from a parabolic potential is small [26].

In the following, we assume that the particle is trapped in the plasma sheath at an equilibrium position z_{eq} above the RF electrode, where the electrostatic force $F_e = QE$ due to the electric field E in the plasma sheath is balanced by the gravitational force $F_g = mg$ acting on the particle's mass m , i.e. $F_e(z_{\text{eq}}) = F_g$, where $g = 9.81 \text{ m s}^{-2}$ is the gravitational acceleration, Q is the electric charge on the particle and $E = E(z)$ is the electric field strength. Furthermore, we assume that the restoring force $F_R = F_e - F_g$ in the neighborhood of z_{eq} varies linearly with particle height z above the electrode, i.e.

$$F_R = -\kappa(z - z_{\text{eq}}). \quad (1)$$

Following Tomme *et al* [26], we then express the equation of motion as

$$m\ddot{z} + 2\gamma\dot{z} + \kappa(z - z_{\text{eq}}) = F(t), \quad (2)$$

where 2γ is the damping constant, κ the restoring constant and $F(t)$ an external force acting on the particle. For the simple damped harmonic oscillator (equation (2) with $F = 0$), we obtain [26]

$$\kappa = m\omega_r^2 + \frac{\gamma^2}{m} \approx m\omega_r^2 \quad (3)$$

with ν_r being the eigenfrequency, and $\omega_r = 2\pi\nu_r$ and $m\omega_r^2 \gg \gamma^2/m$ are the conditions considered here.

4.1. Particle's charge

The accumulated negative charge at the particle can be estimated from its equilibrium position $z_{\text{eq}} = 0.87 \text{ cm}$ with the ion beam *off*. We assume a linear variation of the electric force with particle height z above the electrode, i.e.

$$E(z) = 2\frac{\Delta V}{d_s} \left(1 - \frac{z}{d_s}\right), \quad (4)$$

with $\Delta V = V_{\text{bias}} - V_{\text{pl}}$. Here, d_s is the position of the sheath edge, $V_{\text{bias}} = -300 \text{ V}$ is the electrode self-bias potential and $V_{\text{pl}} = 15 \text{ V}$ is the plasma potential. The position of the sheath edge is estimated from the position of the smaller (diameter of $0.8 \mu\text{m}$) and thus considerably lighter particles that are trapped at $z = 1.05 \text{ cm}$; this position approximately corresponds to the sheath edge. Using $F_e(z_{\text{eq}}) = QE(z_{\text{eq}}) = F_g$, we obtain $Q = -4.1 \times 10^7$ elementary charges.

Likewise, we can calculate the particle's charge from the restoring constant $\kappa \approx m\omega_r^2 = 3.5 \times 10^{-5} \text{ kg s}^{-2}$ (equation (3)), which we obtain with the deduced resonance frequency $\nu_r = 11.3 \text{ Hz}$ and a particle mass $m = 6.9 \mu\text{g}$. Expressing the restoring constant κ as the gradient of the restoring force,

$$\kappa = \frac{\partial F}{\partial z} = Q \frac{\partial E}{\partial z} + E \frac{\partial Q}{\partial z}, \quad (5)$$

we obtain, for a constant Q and with $\partial E/\partial z = -5.7 \times 10^6 \text{ V m}^{-2}$ (equation (4)), $Q = -3.8 \times 10^7$ elementary charges, in fair agreement with the previous estimate.

For a theoretical estimate of the particle's charge, we consider the ion and electron currents flowing to the particle. For the electron current density j_e and the ion current density j_i , we use the orbital motion-limited (OML) currents [27]

$$j_e = e_0 n_e \sqrt{\frac{kT_e}{2\pi m_e}} \exp\left(\frac{e_0 \phi}{kT_e}\right), \quad (6)$$

and

$$j_i = e_0 n_i \sqrt{\frac{kT_i}{2\pi m_i}} \left(1 - \frac{e_0 \phi}{kT_i}\right), \quad (7)$$

where the surface potential ϕ of the particle is connected to the particle's charge Q via

$$Q = 4\pi\epsilon_0 r \left(1 + \frac{r}{\lambda_d}\right) \phi, \quad (8)$$

and where

$$\lambda_d = \sqrt{\frac{\epsilon_0 k}{e_0^2 (n_e/T_e + n_i/T_i)}} \quad (9)$$

is the Debye screening length. T_e and T_i are electron and ion temperatures, m_e and m_i are electron and ion masses, e_0 is the elementary charge and k is the Boltzmann constant. Likewise, since the particle resides outside the plasma in the sheath region, we may use the Bohm ion flux

$$j_i = 0.6e_0 n_i \sqrt{\frac{kT_e}{m_i}} \quad (10)$$

instead of equation (7).

Under equilibrium conditions, the sum of the electron and ion currents to the particle disappears. Further assuming quasi-neutrality ($n_e = n_i$) and combining equations (10) and (6), we obtain

$$\phi = \frac{kT_e}{2e_0} \ln\left(\frac{0.72\pi m_e}{m_i}\right). \quad (11)$$

On the basis of the Bohm ion flux (equation (10)) and using $T_e = 3$ eV and $n_e = 1.5 \times 10^{15} \text{ m}^{-3}$ [28], we obtain $\phi = -15.6$ V and $Q = -6.1 \times 10^6$ elementary charges. This value is almost 7 times smaller than the measured charge on the particle. An even smaller value of $Q = -2.9 \times 10^6 e_0$ is obtained when using the OML (equation (7)) rather than the Bohm (equation (10)) ion flux. Kindly note that a non-Maxwellian electron energy distribution function displaying a high-energy tail should not influence these results significantly. As is obvious from equation (11), the particle's charge depends linearly on the electron temperature T_e and thus a drastic temperature variation would be required to explain the measured charge.

We also mention the alternative approach of Bronold *et al* [29] that is based on a balance between inflowing and outflowing electrons. Accordingly, the particle's charge is given by

$$Q = 4\pi r^2 \frac{e_0 h}{kT_p} \exp\left(\frac{W_e}{kT_p}\right) j_e, \quad (12)$$

where h is Planck's constant, T_p the particle temperature and j_e the OML electron flux (equation (6)) to the particle, while the ion flux to the particle is neglected. The electron binding energy W_e is expressed as

$$W_e = \frac{R(\epsilon - 1)^2}{16(\epsilon + 1)^2}, \quad (13)$$

where R is the Rydberg energy and ϵ is the relative dielectric constant of the particle ($\epsilon \approx 4.5$ for SiO_2 [30]). This yields an electron binding energy $W_e = 0.344$ eV, much smaller than the photon energy of the illuminating laser (2.34 eV). Thus, a significant electron detachment by the

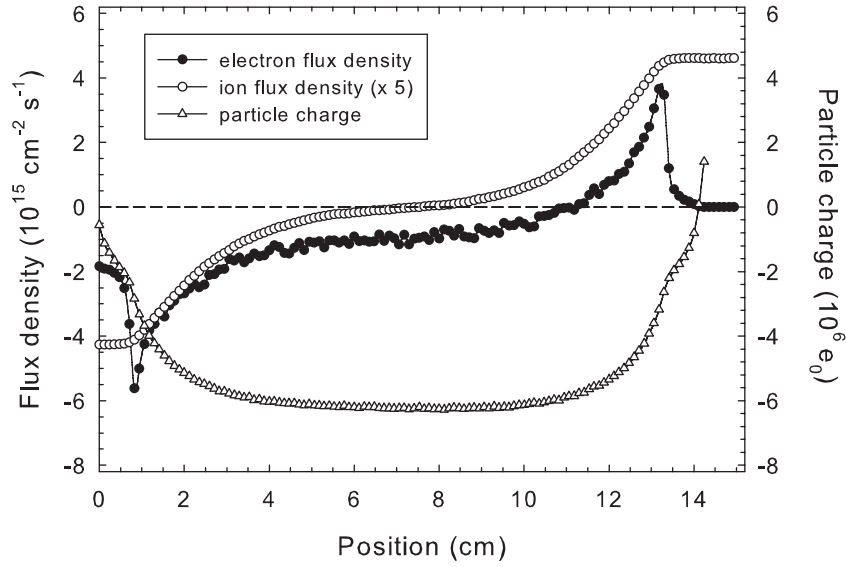


Figure 8. Simulated electron (●) and ion (○) flux density versus position. The resulting particle charge (Δ) is also shown.

laser light should occur. This should reduce the particle's charge, which has not been observed, however. Even without this additional complication, the model is insufficient to explain the measured charge on the particle.

The electron and ion fluxes from the PIC simulation of the RF plasma and the resulting charge on the particle are shown in figure 8. The plasma parameters together with analytical models like OML or the Khrapak model are used to compute the dust charge in the RF discharge [27, 31]. The predicted charge at the particle if placed inside the plasma bulk amounts to about -6.3×10^6 elementary charges, which is in reasonable agreement with the charge obtained from the analytical analysis (see above).

The inward (into the plasma) directed electric force $|Q\vec{E}|$ acting on the particle is displayed in figure 6. The force shows pronounced maxima in the sheath regions in front of the grounded and powered electrodes at positions $z \approx 0.23$ and 13.8 cm, respectively. The latter value is close to the actual particle position at $z \approx 14.1$ cm. The calculated electric field force is insufficient to compensate for the gravitation force, which exceeds the electric field force by more than one order of magnitude.

Thus, the simulation does not improve the analytical results, and other reasons for the apparent discrepancy have to be sought. One possible reason is the porous structure of the particle. A simple estimate shows that the particle's inner surface is about two orders of magnitude larger than its outer surface, and this could give rise to a much larger charge than calculated with the spherical condenser model (equation (8)).

Other possible reasons are (i) the non-spherical shape, (ii) the non-conducting (insulating) material and (iii) the size of the particle which affects the electrostatic force acting on it. According to Daugherty *et al* [32], we have to replace the electric field strength E by an effective field E_{eff} and the electrostatic force F_e by

$$F_e = Q \left[E \left(1 + \frac{(r/\lambda_d)^2}{3(1+r/\lambda_d)} \right) \right]. \quad (14)$$

An estimation shows that under the conditions considered here this effect accounts for a factor of 1.2, which is again insufficient to explain the deviation.

Upper limits for the particle charge have been discussed, e.g., by Trottenberg *et al* [33]. Accordingly, the electric charge on a particle is limited by electron field emission and by field-induced evaporation. The electric field strength E_p on the surface of a spherical particle with radius r is related to its specific charge Q/m :

$$E_p = \frac{r\rho}{3\epsilon} \frac{Q}{m} \quad (15)$$

with ρ being the particle density. Taking $Q = 4 \times 10^7$ elementary charges and $m = 6.9 \mu\text{g}$, we obtain $E_p \approx 10^7 \text{ V m}^{-1}$. The value is significantly lower than the limits set by electron field emission ($|E_p| > 10^9 \text{ V m}^{-1}$) and by field desorption ($|E_p| > 10^{10} \text{ V m}^{-1}$).

4.2. Neutral drag force

The decay constant

$$\tau = m/\gamma \quad (16)$$

is related to the neutral drag and, hence, the viscosity η the particle experiences in the surrounding gas. Making use of Stokes' law [34], we express the damping constant γ by the viscosity η as

$$\gamma = 3\pi\eta r, \quad (17)$$

from which we obtain $\eta = 5.8 \mu\text{Pa s}$ for $\tau = 1 \text{ s}$ (see figure 7). This value is significantly lower than the standard value for argon of $\eta = 22.4 \mu\text{Pa s}$ [35]. It is well known, however, that equation (17) does not hold for small particle sizes of the order of the mean free path λ . Applying Cunningham's correction [36, 37], we obtain an effective viscosity

$$\eta_{\text{eff}} = \eta \frac{r}{r + A\lambda}, \quad (18)$$

where r is the particle radius,

$$A = \alpha + \beta \exp(-\xi r/\lambda), \quad (19)$$

and with the parameters $\alpha = 1.227$, $\beta = 0.42$ and $\xi = 0.85$ taken from [35]. The calculated correction is rather large and yields $\eta_{\text{eff}} = 0.89 \mu\text{Pa s}$ at a pressure of 3.5 Pa. A similar value of $0.85 \mu\text{Pa s}$ is obtained making use of Epstein's expression [38, 39]. Both values are significantly smaller than the experimental value of $5.8 \mu\text{Pa s}$ (see above). However, considering a likely roughness of the particle's surface and its porosity, the difference does not appear unrealistic.

4.3. Ion drag force

For sufficiently high energies and a sufficiently large particle, the ion drag force exerted by the external ion beam may be calculated from the momentum transfer $m_b v_b$ multiplied by the ion flux density $n_b v_b$ and the particle's cross-sectional area,

$$F_i = \pi r^2 n_b m_b v_b^2, \quad (20)$$

where n_b is the ion beam density, v_b the ion velocity and m_b the ion mass. The ion velocity is calculated from the ion energy as extracted from the ion source by the source potential U_s :

$$v_b = \sqrt{\frac{2e_0 U_s}{m_b}}, \quad (21)$$

whereas the ion density was obtained from the energy influx of $0.06 \text{ J cm}^{-2} \text{ s}^{-1}$ measured by a thermal probe [15, 40]. For an ion beam energy $e_0 U_s = 800 \text{ eV}$, we thus obtain $F_i = 9.5 \times 10^{-10} \text{ N}$. We can compare this number with the force $\Delta F = \kappa \overline{\Delta z} = 1.6 \times 10^{-8} \text{ N}$ required for a mean particle displacement of $\overline{\Delta z} = 4.5 \times 10^{-4} \text{ m}$ during its interaction with the ion beam (figure 7). Comparing the two forces we note that the estimated ion drag force, only accounts for 6% of the calculated ΔF .

4.4. Particle de-charging

The difference between the two forces is attributed to the particle's de-charging by the action of the ion beam. In order to estimate the de-charging effect, we again consider the ion (equation (7) or (10)) and electron (equation (6)) currents to the particle to which we add the contribution from the ion beam

$$j_i^{\text{beam}} = e_0 n_b v_b (1 + \delta) \quad (22)$$

and where secondary electron emission by the impact of energetic ions is accounted for by the $1 + \delta$ term, with δ being the secondary electron emission coefficient for energetic ion impact. Typically, $\delta \approx 0.1$ for secondary emission of electrons bound to solids [41] and as such it is not expected to provide a significant additional contribution.

Under equilibrium conditions the total current to the particle disappears. Assuming quasi-neutrality ($n_e = n_i$) and combining equations (10) and (22) with equation (6), we obtain

$$\exp\left(\frac{e\phi}{kT_e}\right) = \frac{0.6n_i\sqrt{kT_e/m_i} + n_b v_b (1 + \delta)}{n_e \sqrt{kT_e/2\pi m_e}} \quad (23)$$

and, hence,

$$\Delta\phi = \frac{kT_e}{e_0} \ln\left(1 + \frac{n_b v_b (1 + \delta)}{0.6n_i \sqrt{kT_e/m_i}}\right), \quad (24)$$

where $\Delta\phi \equiv \phi - \phi_0$, ϕ_0 is the surface potential without ion beam ($n_b = 0$) and

$$\frac{\Delta Q}{Q} = \frac{\Delta\phi}{\phi_0} = 2 \frac{\ln\left(1 + \frac{n_b v_b (1 + \delta)}{2.4n_i \sqrt{kT_e/m_i}}\right)}{\ln\left(0.72\pi \frac{m_e}{m_i}\right)} \quad (25)$$

in connection with equation (8). Furthermore, making use of

$$\frac{\partial F}{\partial z} = Q \frac{\partial E}{\partial z} + E \frac{\partial Q}{\partial z},$$

we obtain

$$\frac{\Delta Q}{Q} = \frac{\Delta F}{F} - \frac{\Delta E}{E} \approx 0.94 \times \frac{\Delta F}{F},$$

as we attribute 6% of ΔF to the ion drag force and the remaining 94% to the particle's de-charging by the ion beam (see section 4.3). With $\Delta F = 1.6 \times 10^{-8}$ N and $F = F_g = 6.8 \times 10^{-8}$ N, we obtain $\Delta Q/Q \approx 22.1\%$.

From our theoretical analysis based on the Bohm ion flux (equation (25)) using $T_e = 3$ eV and $n_e = 1.5 \times 10^{15} \text{ m}^{-3}$ [28], we obtain $\Delta Q/Q \approx 16.4\%$, which is in fair agreement with experiment. The value of $\Delta Q/Q \approx 3.0\%$ is much smaller, which we obtain if we use the OML (equation (7)) rather than the Bohm (equation (10)) ion flux. One explanation for this discrepancy may be due to an overestimation of the ion current in the sheath region as predicted by the OML model. As ions become considerably accelerated when leaving the plasma, their energy in the plasma sheath drastically differs from their initial energy within the plasma. This has the consequence that the $1 - e_0\phi/kT_i$ term in equation (7), which accounts for an enhanced ion collection by the particle, becomes too large if the initial (thermal) T_i is used. A modification of this term making use of, e.g., $T_i = T_e/2$ as follows from the Bohm theory [42] will thus lead to a significantly larger value of $\Delta Q/Q \approx 9.0\%$ compared with the previous value.

4.5. Fourier frequency spectrum

For the square wave-modulated ion beam that we used for interaction with the particle, we can express the external force $F(t)$ as a Fourier series,

$$F(t) = \frac{F_0}{2} \left(1 - \frac{4}{\pi} \sum_{n=1}^m f_n \sin(\omega_n t) \right), \quad (26)$$

where $\omega_n = 2\pi(2n-1)\nu_a$, with ν_a being the square wave modulation (excitation) frequency of the ion beam, and where the Fourier coefficients f_n are given by

$$f_n = \frac{1}{2n-1}. \quad (27)$$

The solution of $z(t)$ is obtained as

$$z(t) = \frac{F_0}{m} \left(\frac{1}{2\omega_r^2} + \frac{2}{\pi} \sum_{n=1}^m a_n f_n \sin(\omega_n t - \varphi_n) \right), \quad (28)$$

where

$$a_n = \frac{1}{\sqrt{(\omega_r^2 - \omega_n^2)^2 + (2\gamma\omega_n)^2}}, \quad (29)$$

$$\varphi_n = \arctan \left(\frac{2\gamma\omega_n}{m(\omega_r^2 - \omega_n^2)} \right), \quad (30)$$

and $0 \leq \varphi_n \leq \pi$.

As a consequence, the theoretical frequency spectrum only contains odd harmonics. The experimental results for $\nu_a = 0.5$ Hz rather well follow this prediction (figure 9). Deviations appear in the vicinity of the resonance frequency where even side bands develop. The origin of these may be traced back to the before-mentioned de-charging due to the incident ion beam.

A closer inspection of figure 7 reveals significantly different oscillation frequencies for the cases with ion beam *off* and *on*. Figure 10 shows a separate Fourier analysis of the experimental

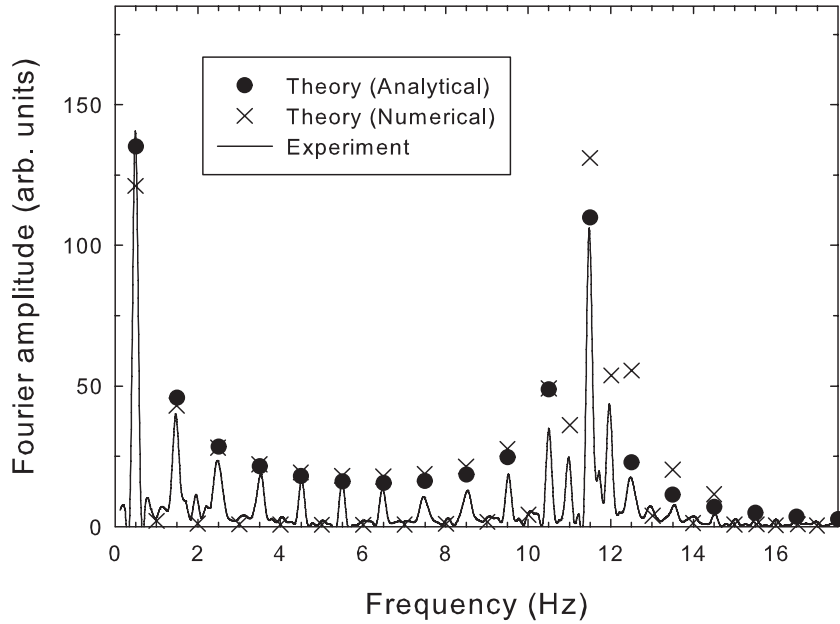


Figure 9. Comparison of experimental and theoretical Fourier coefficients following ion beam excitation at 0.5 Hz.

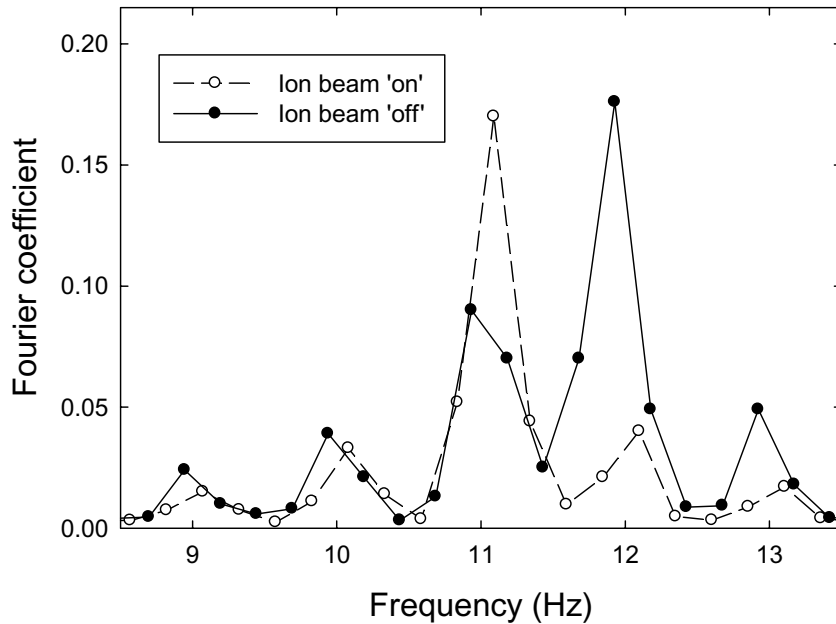


Figure 10. Separate Fourier analysis for the cases at ion beam *on* and *off* following ion beam excitation with 0.5 Hz.

data for the two cases with ion beam *off* and *on*. Apparently, the two cases have slightly different resonance frequencies, which can be explained by a different restoring force due to differing particle charges at the two positions. The relative frequency difference $\Delta \nu_r / \nu_r$ amounts to about 7%; as the restoring force and, hence, the particle's charge depend quadratically on the resonance frequency, this corresponds to a relative charge difference $\Delta Q / Q \approx 2 \times 7\% = 14\%$,

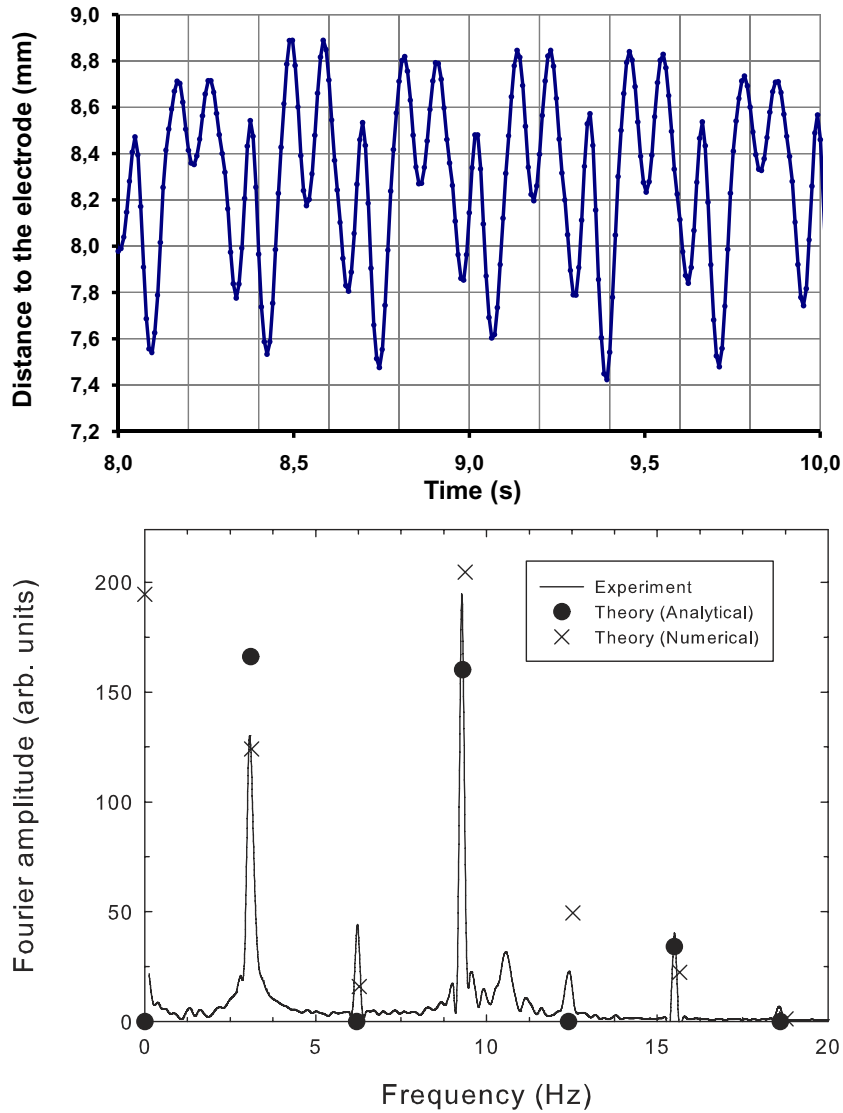


Figure 11. Particle position following ion beam excitation at 3.1 Hz (top) and the corresponding frequency spectrum obtained by Fourier analysis (bottom).

i.e. about twice the frequency difference. The result thus provides further confirmation of the particle's de-charging as derived in section 4.4.

The particle's de-charging in the plasma sheath leads to a deviation from a harmonic potential and to a restoring force F_R that is no longer linearly depending on the particle's position z (equation (1)). Rather, we approximate F_R by

$$F_R = \kappa(z - z_{eq}) \times \left(1 + 2 \frac{\Delta\omega_r}{\omega_r} \frac{(z - z_{eq})}{\Delta z} \right) \quad (31)$$

and we arrive at the numerical solutions shown in figure 9, which reproduces the experimental finding.

At an excitation frequency $\nu_a = 3.1$ Hz, the particle motion is largely governed by a combination of the fundamental frequency and the third harmonic at 9.3 Hz (figure 11).

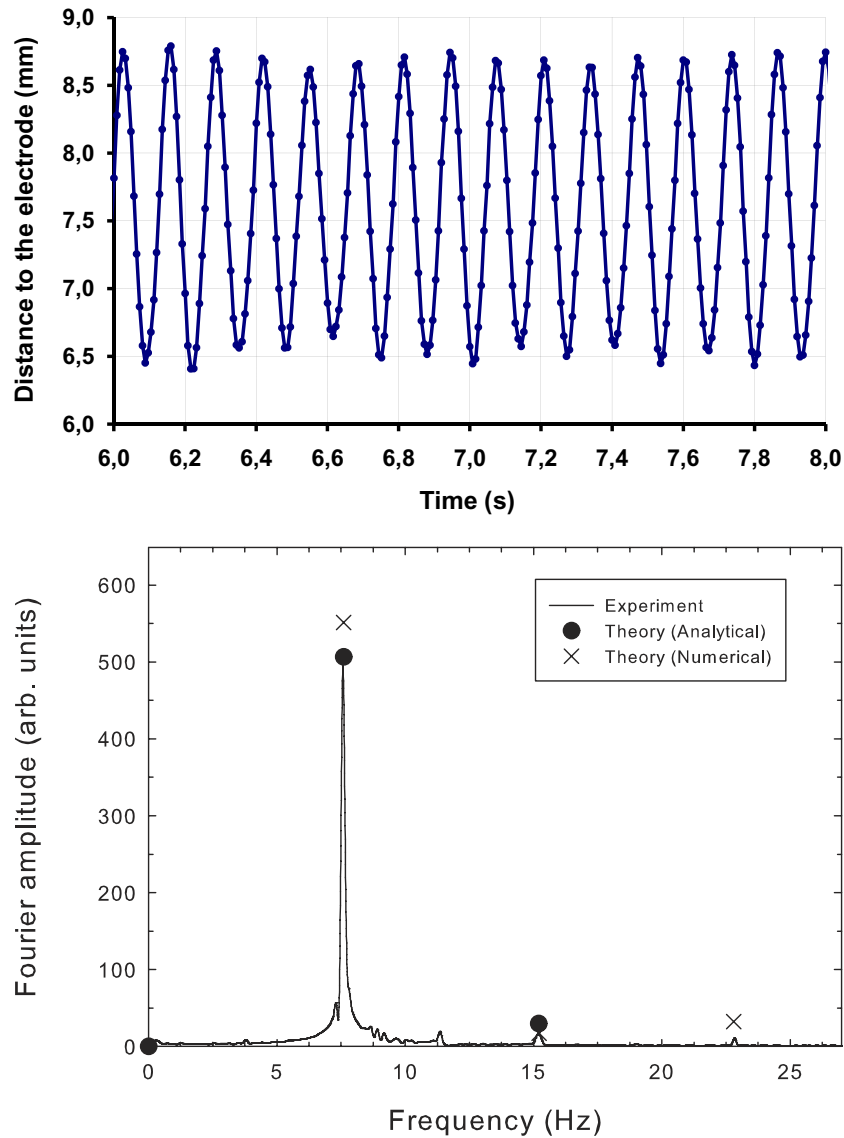


Figure 12. Particle position following ion beam excitation at 7.6 Hz (top) and corresponding frequency spectrum obtained by Fourier analysis (bottom).

However, other frequencies corresponding to the even second and fourth harmonics also occur. The result is in fair agreement with the theoretical analysis.

At an excitation frequency $\nu_a = 7.6$ Hz, the particle motion is dominated by the first harmonic (figure 12). The particle motion almost fully follows the excitation frequency and higher harmonics do not play a significant role. The experimental results are in excellent agreement with the theoretical prediction.

5. Conclusion

The accumulated charge of about 4×10^7 elementary charges on a levitating porous particle with a diameter of $250 \mu\text{m}$ in an RF plasma was found to be about one order of magnitude

larger than predicted by theoretical models. The difference is attributed to the porous structure of the particle. This is experimentally supported by the scaling of the particle mass versus mean particle radius. The particle motion under the action of the pulsed ion beam displays an oscillatory motion. The Fourier-analyzed motion is dominated by the excitation frequency and odd higher harmonics that peak near the resonance frequency. The appearance of even harmonics is explained by a variation of the particle's charge depending on its position in the plasma sheath. Furthermore, the results of this study demonstrate that particle oscillations due to the action of an external ion beam can be used for the probing of complex plasma environments.

Acknowledgments

This work was supported by the Deutsche Forschungsgemeinschaft (DFG) through Sonderforschungsbereich/Transregio TRR24 'Fundamentals of Complex Plasmas'. One of us (RS) acknowledges funding of this work by the Initiative and Networking Fund of the Helmholtz Association.

References

- [1] Vladimirov S V, Ostrikov K and Samarian A A 2005 *Physics and Applications of Complex Plasmas* (London: Imperial College Press)
- [2] Mendonça J T, Resendes D P and Shukla P K (ed) 2008 *Multifacets of Dusty Plasmas* (AIP Conf. Proc. vol 1041)
- [3] Shukla P K and Eliasson B 2009 *Rev. Mod. Phys.* **81** 25
- [4] Hippler R and Kersten H 2008 Applications of dusty plasmas *Low Temperature Plasmas* vol 2 ed R Hippler, H Kersten, M Schmidt and K H Schoenbach (Berlin: Wiley) pp 787
- [5] Barnes M S, Keller J H, Forster J C, O'Neill J A and Coultas D K 1992 *Phys. Rev. Lett.* **68** 313
- [6] Tomme E B, Law D A, Annaratone B M and Allen J E 2000 *Phys. Rev. Lett.* **85** 2518
- [7] Melzer A and Goree J 2008 Fundamentals of dusty plasmas *Low Temperature Plasmas* vol 1 ed R Hippler, H Kersten, M Schmidt and K H Schoenbach (New York: Wiley) pp 129
- [8] Bouchoule A (ed) 1999 *Dusty Plasmas* (New York: Wiley) pp 27ff
- [9] Piel A, Arp O, Block D, Pilch I, Trottenberg T, Käding S, Melzer A, Baumgartner H, Henning C and Bonitz M 2008 *Plasma Phys. Control. Fusion* **50** 124003
- [10] Konopka U, Morfill G E and Ratke L 2000 *Phys. Rev. Lett.* **84** 891
- [11] Melzer A 2001 *Phys. Scr. T* **89** 33
- [12] Basner R, Sigeneger F, Loffhagen D, Schubert G, Fehske H and Kersten H 2009 *New J. Phys.* **11** 013041
- [13] Kortshagen U and Mümken G 1996 *Phys. Lett. A* **217** 126
- [14] Samarian A A and James B W 2005 *Plasma Phys. Control. Fusion* **47** B629
- [15] Kersten H, Wiese R, Neumann H and Hippler R 2006 *Plasma Phys. Control. Fusion* **48** B105
- [16] Garscadden A, Ganguly B N, Haaland P D and Williams J 1994 *Plasma Sources Sci. Technol.* **3** 239
- [17] Winter J 1998 *Plasma Phys. Control. Fusion* **40** 1201
- [18] Whipple E C 1981 *Rep. Prog. Phys.* **44** 1197
- [19] Kittel C 1995 *Introduction to Solid State Physics* 7th edn (New York: Wiley)
- [20] Bronold F X, Matyash K, Tskhakaya D, Schneider R and Fehske H 2007 *J. Phys. D: Appl. Phys.* **40** 6583–92
- [21] Matyash K, Schneider R, Dittmann K, Meichsner J, Bronold F X and Tskhakaya D 2007 *J. Phys. D: Appl. Phys.* **40** 6601–7
- [22] Matyash K and Schneider R 2006 *J. Plasma Phys.* **72** 809
- [23] Matyash K, Schneider R, Tacogna F, Hatayama A, Longo S, Capitelli M, Tskhakaya D and Bronold F X 2007 *Contrib. Plasma Phys.* **47** 595

- [24] Ikkurthi V R, Matyash K, Melzer A and Schneider R 2008 *Phys. Plasmas* **15** 123704
- [25] Takizuka T and Abe H 1977 *J. Comput. Phys.* **25** 205–19
- [26] Tomme E B, Annaratone B M and Allen J E 2000 *Plasma Sources Sci. Technol.* **9** 87
- [27] Allen J E 1992 *Phys. Scr.* **45** 497
Allen J E, Annaratone B M and de Angelis U 2000 *J. Plasma Phys.* **63** 299
- [28] Kersten H, Stoffels E, Stoffels W W, Otte M, Csambal C, Deutsch H and Hippler R 2000 *J. Appl. Phys.* **87** 3637
- [29] Bronold F X, Fehske H, Kersten H and Deutsch H 2008 *Phys. Rev. Lett.* **101** 175002
- [30] www.asiainstruments.com/technical.aspx
- [31] Khrapak S A *et al* 2005 *Phys. Rev. E* **72** 016406
- [32] Daugherty J E, Porteous R K and Graves D B 1993 *J. Appl. Phys.* **73** 1617
- [33] Trottenberg Th, Kersten H and Neumann H 2008 *New J. Phys.* **10** 063012
- [34] Demtröder W 2006 *Experimentalphysik, Band 1: Mechanik und Wärme* 4th edn chapter 8 (Berlin: Springer)
- [35] Rader D J 1990 *J. Aerosol. Sci.* **21** 161
- [36] Cunningham E 1910 *Proc. R. Soc. A* **83** 357
- [37] Millikan R A 1911 *Phys. Rev.* **32** 366
- [38] Epstein P S 1924 *Phys. Rev.* **23** 710–33
- [39] Nitter T 1996 *Plasma Sources Sci. Technol.* **5** 93–111
- [40] Kersten H, Deutsch H, Steffen H, Kroesen G M W and Hippler R 2001 *Vacuum* **63** 385
- [41] Hippler R 2008 Elementary processes of plasma surface interactions *Low Temperature Plasmas* vol 1 ed R Hippler, H Kersten, M Schmidt and K H Schoenbach (Berlin: Wiley) pp 71
- [42] Riemann K-U 1991 *J. Phys.D: Appl. Phys.* **24** 493

Article IV

Fourier Analysis of Particle Motion in a Radio Frequency Plasma Under Pulsed Argon Ion Beam Bombardment

Fourier Analysis of Particle Motion in a Radio Frequency Plasma Under Pulsed Argon Ion Beam Bombardment

Ruben Wiese, Vladimir Sushkov, Holger Kersten, and Rainer Hippler

Abstract—The behavior of a single powder particle with a diameter of 250 μm in a radio frequency plasma under pulsed argon ion beam bombardment was investigated. The motion of the powder particle under the action of the ion beam was investigated and Fourier-analyzed. The experimental results are in fair agreement with the theoretical considerations.

Index Terms—Dusty plasma, Fourier series, ion beam applications, plasma measurements.

I. INTRODUCTION

DURING THE last decade, the importance of the “dusty plasmas” has increased enormously. On one hand, particles are systematically generated in the plasma for special applications in materials research, metallurgy, and medicine, or their properties are changed in the plasma [1]. On the other hand, particles are used to determine plasma parameters, like electric field strength, energy transport, or the density of charged carriers [2]. The background of many of these applications is the specific behavior of powder particles in a radio frequency (RF) plasma. When particles are inserted into a plasma, they become negatively charged due to the larger mobility of electrons compared to ions. For particles with a diameter of several 10 μm , this charge can become as large as several 100 000 elementary charges [3]. While the gravitational force acting on a sufficiently massive particle tends to pull the particle out of the plasma, the electric field in the plasma sheath above a negatively self-biased RF electrode repels the negatively charged particle and thus acts into the opposite direction. Under certain conditions, i.e., for particles with diameters in the micrometer regime, the particle encounters a balance between upward (electric) and downward (gravitation) forces and becomes trapped in the sheath region above the electrode (Fig. 1). A detailed description of the interaction of these and

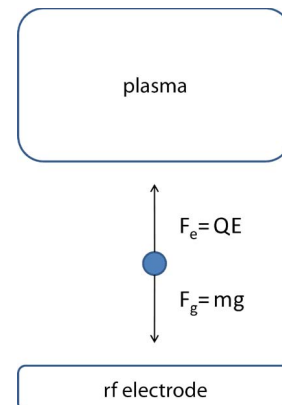


Fig. 1. Particle trapped in the sheath region between the plasma and RF electrode by the combined action of upward-directed electromagnetic ($F_e = QE$) and downward-directed gravitational ($F_g = mg$) forces (schematic).

other forces may be found elsewhere [4]–[6]. In the present experiment, we investigate the interaction of an external ion beam with a particle levitated in an RF plasma sheath. For that purpose, a particle trapped in the sheath was exposed to a pulsed ion beam with known intensity and energy and thereby excited to an oscillatory motion. A detailed analysis of the particle’s motion was carried out from which the Fourier frequency spectrum was derived.

II. EXPERIMENTAL SETUP

The experiments are carried out in the PULVA-II reactor [7]. It consists of a cylindrical reactor with a diameter of 400 mm (Fig. 2) and pumped with the help of a 500-l/s turbomolecular pump to a residual gas pressure of less than 10^{-4} Pa. The effective pumping speed is varied by an adjustable butterfly valve. Gas has been admitted by a gas flow controller (MKS) with a flow rate of 30 sccm argon, yielding a typical operation pressure of 3.5 Pa. An RF discharge is maintained inside the chamber with the help of a planar electrode (diameter 130 mm) located at the bottom of the reactor chamber and driven via a matching network (Dressler VM700) by an RF generator (Dressler Cesar 1310) at 13.56 MHz and with a power of 10 W. It results in an electrode self-bias potential of -300 V and a plasma potential of $+15$ V.

A vertically expanded laser beam (wavelength of 532 nm and total power of 2 W) is employed for particle illumination. The particle position is recorded through a glass window at 90° with respect to the ion beam and through a narrow

Manuscript received June 17, 2009; revised September 29, 2009 and November 2, 2009. First published February 25, 2010; current version published April 9, 2010. This work was supported by the Deutsche Forschungsgemeinschaft (DFG) through Sonderforschungsbereich/Transregio TRR24 Fundamentals of complex plasmas.

R. Wiese is with the Institut für Plasmaforschung und Technologie, 17489 Greifswald, Germany.

V. Sushkov and R. Hippler are with the Institut für Physik, Ernst-Moritz-Arndt-Universität Greifswald, 17489 Greifswald, Germany (e-mail: Hippler@physik.uni-greifswald.de).

H. Kersten is with the Institut für Experimentelle und Angewandte Physik, Christian-Albrechts-Universität zu Kiel, 24098 Kiel, Germany.

Color versions of one or more of the figures in this paper are available online at <http://ieeexplore.ieee.org>.

Digital Object Identifier 10.1109/TPS.2010.2041461

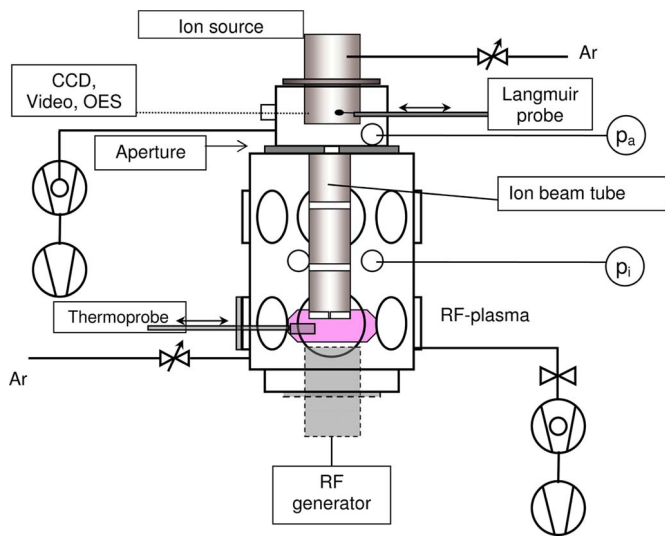
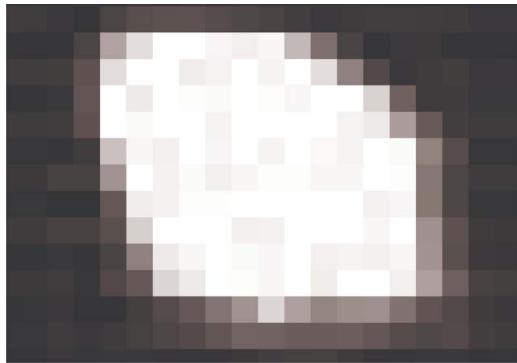


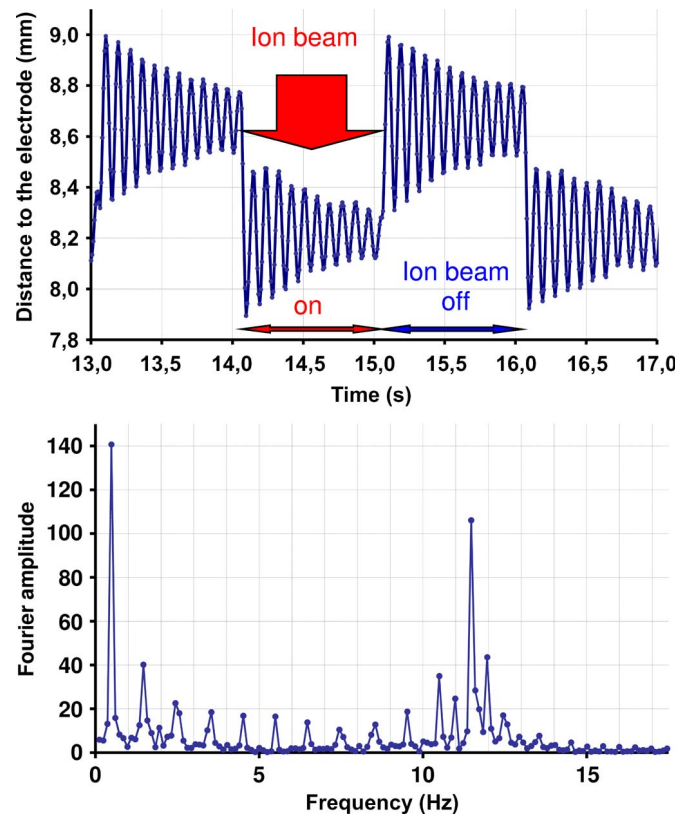
Fig. 2. Schematic setup of the PULVA-II reactor [7].

Fig. 3. Recorded particle image (1 pixel corresponds to 23 μm).

filter (530 nm). Two cameras, a reflex camera (Nikon D70) with a focal length of 24–120 mm and a high speed camera (Nikon FastCam PCI R2) with a frame rate of 125 pictures per second, have been employed. The recorded video sequences are analyzed with a self-written program which calculates the particle's coordinates as a function of time and transfers the particle's positions in chronological order to a spread sheet.

Particles are introduced into the plasma with the help of a sieve that is manipulated from the outside. We used SiO_2 powder particles (density of 2.2 g/cm^3) with a diameter of 0.8 μm . In addition, the powder contained large agglomerates with sizes of up to about 300 μm . After several attempts, it was achieved that only one particle was located in the sheath whose motion was recorded by the camera. The isolated particle displayed in Fig. 3 was used for the measurements reported in the following.

In order to investigate the particle's behavior under the influence of an ion beam, an ion source EC/A 125 (IOM Leipzig) located at a vacuum port opposite to the RF electrode is directed downward to the particle cloud. It is operated with a gas flow of 8 sccm argon at a pressure of 0.06 Pa, maintained by a separate turbo pump (Leybold) with a pumping speed of 1500 l/s. For pulsed operation, the ion source is driven with a square-wave voltage in the frequency range 0.1–8 Hz and with a duty cycle of 1 : 1.

Fig. 4. Top figure: particle position *versus* the following ion beam excitation with 0.5 Hz. Bottom figure: experimental Fourier coefficients derived from the particle's movement.

III. RESULTS AND DISCUSSIONS

The particle motion under the influence of a square-wave-modulated ion beam with a beam energy of 800 eV and a modulation frequency of 0.5 Hz is displayed in Fig. 4. By interaction with the ion beam (*on* period), the trapped particles are displaced from their original position and start to oscillate around a new equilibrium position. During the ion beam *off* period, the particle resumes to its initial equilibrium position where it continues to oscillate. At this low excitation frequency, the particle oscillates with a frequency close to its eigen or resonance frequency superimposed on the modulation frequency of the ion beam.

The chronological course of the particle's movement was evaluated, and a Fourier analysis was carried out in order to determine the particle's frequency spectrum. The deduced frequency spectrum (Fig. 4) shows two major components, namely, the excitation frequency ($\nu_a = 0.5$ Hz) of the ion beam and an enhancement in the Fourier spectrum at the resonance frequency $\nu_r \approx 11.3$ Hz of the particle in the plasma. The Fourier spectrum also contains odd higher harmonics, while even harmonics, except in the neighborhood of the resonance frequency, are suppressed. For the particle oscillation, the back driving force is the difference between the field force, generated by the electric field in the sheath, and the gravitation force on the particle. Since the electric field has an almost linear dependence with distance, the particle's motion resembles that of a linear oscillator. The approximate linearity of the electric field, based on the parabolic shape of the potential, has been asserted, e.g., by Tomme *et al.* who carried out investigations

with oscillating particles, thereby showing that, over a distance of 20% of the sheath thickness, the divergence from a parabolic potential is small [8].

In the following, we assume that the particle is trapped in the plasma sheath at an equilibrium position z_{eq} above the RF electrode where the electrostatic force $F_e = QE$ due to the electric field E in the plasma sheath is balanced by the gravitational force $F_g = mg$ acting on the particle's mass m , i.e., $F_e(z_{eq}) = F_g$, where $g = 9.81 \text{ m/s}^2$ is the gravitational acceleration, Q is the electric charge on the particle, and $E = E(z)$ is the electric field strength. Furthermore, we assume that the restoring force $F_R = F_e - F_g$ in the neighborhood of z_{eq} varies linearly with particle height z above the electrode, i.e.,

$$F_R = -\kappa(z - z_{eq}). \quad (1)$$

Following Tomme *et al.* [8], we then express the equation of motion as

$$m\ddot{z} + 2\gamma\dot{z} + \kappa(z - z_{eq}) = F(t) \quad (2)$$

where m is the particle mass, 2γ is the damping constant, κ is the restoring constant, and $F(t)$ is an external force acting on the particle. For the simple damped harmonic oscillator [(2) with $F = 0$], we get [8]

$$\kappa = m\omega_R^2 + \frac{\gamma^2}{m} \approx m\omega_R^2 \quad (3)$$

with ν_r as the eigenfrequency, $\omega_r = 2\pi\nu_r$, and $m\omega_r^2 \gg \gamma^2/m$ for the here considered conditions.

For a square-wave-modulated ion beam which we used for interaction with the particle, we can express the external force $F(t)$ as a Fourier series

$$F(t) = \frac{F_0}{2} \left(1 - \frac{4}{\pi} \sum_{n=1}^m f_n \sin(\omega_n t) \right) \quad (4)$$

where $\omega_n = 2\pi(2n-1)\nu_a$, ν_a is the square-wave-modulation (excitation) frequency of the ion beam, and the Fourier coefficients f_n are given as

$$f_n = \frac{1}{2n-1}. \quad (5)$$

The solution of $z(t)$ is obtained as

$$z(t) = \frac{F_0}{m} \left(\frac{1}{2\omega_R^2} + \frac{2}{\pi} \sum_{n=1}^m a_n f_n \sin(\omega_n t - \varphi_n) \right) \quad (6)$$

where

$$a_n = \frac{1}{\sqrt{(\omega_R^2 - \omega_n^2)^2 + (2\gamma\omega_n)^2}} \quad (7)$$

$$\varphi_n = \arctan \left(\frac{2\gamma\omega_n}{m(\omega_R^2 - \omega_n^2)} \right) \quad (8)$$

and $0 \leq \varphi_n \leq \pi$. It should be emphasized that both equations contain the damping constant γ and that damping is thus accounted for.

As a consequence, the theoretical frequency spectrum (calculated with a resonance frequency $\nu_r = 11.3 \text{ Hz}$) only contains

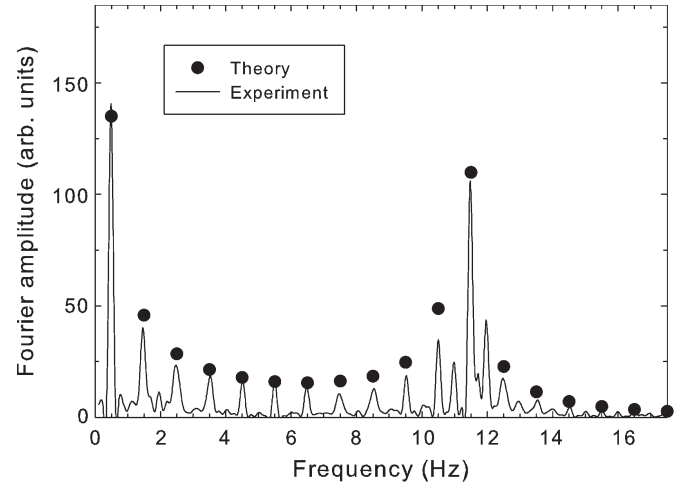


Fig. 5. Comparison of the experimental and theoretical Fourier coefficients following ion beam excitation with 0.5 Hz.

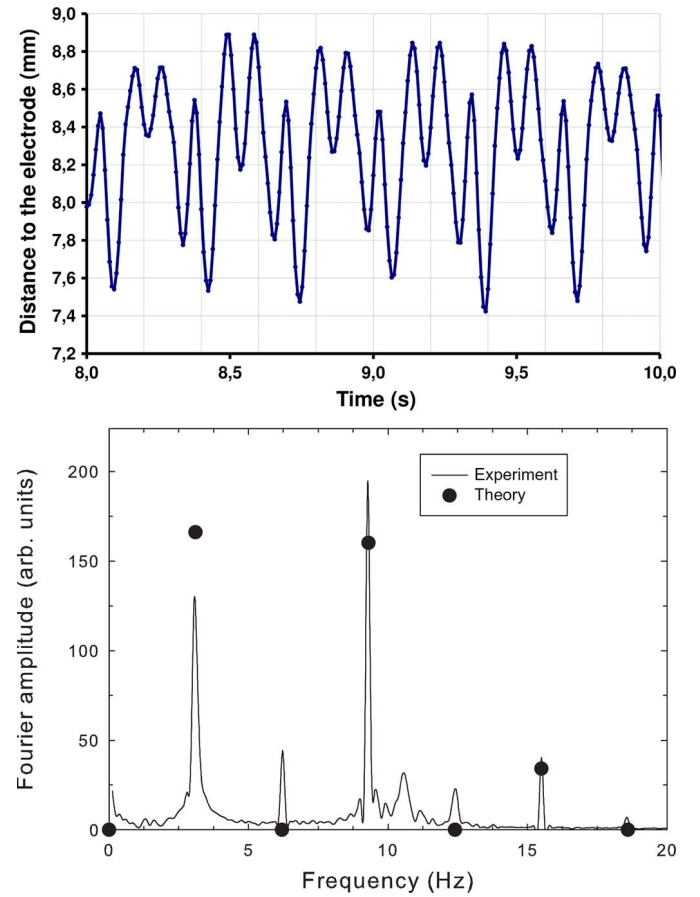


Fig. 6. (Top) Particle position following ion beam excitation with 3.1 Hz and (bottom) corresponding frequency spectrum obtained by Fourier analysis.

odd harmonics. The experimental results for $\nu_a = 0.5 \text{ Hz}$ rather follow well this prediction (Fig. 5). Deviations appear in the vicinity of the resonance frequency where even side bands develop. The origin of these may be traced back to a nonlinearity of the restoring force caused by a position dependence of the particle's charge and a decharging of the particle by the incident ion beam. This is further evidenced by the slightly different oscillation frequencies which differ by about 7% for the ion beam *on* and *off* situations (see Fig. 4). As the restoring

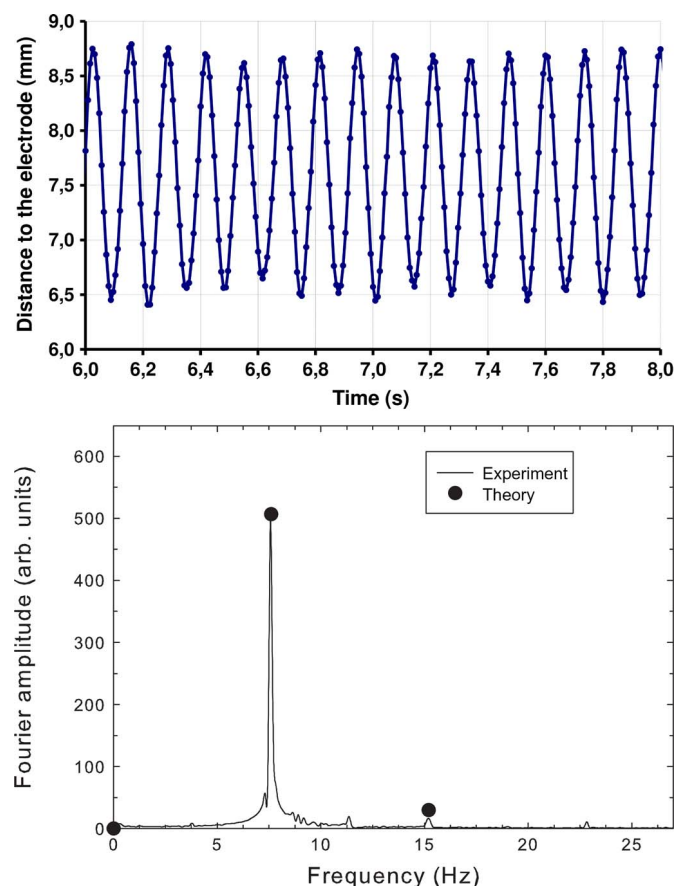


Fig. 7. (Top) Particle position following ion beam excitation with 7.6 Hz and (bottom) corresponding frequency spectrum obtained by Fourier analysis.

force and, hence, the particle's charge depend quadratically on the resonance frequency, this corresponds to a relative charge difference $\Delta Q/Q \approx 2 \times 7\% = 14\%$, i.e., about twice of the relative frequency difference.

At an excitation frequency $\nu_a = 3.1$ Hz, the particle motion is largely governed by a combination of the fundamental frequency and the third harmonics at 9.3 Hz (Fig. 6). However, other frequencies corresponding to the even 2nd and 4th harmonics also occur. The result is in fair agreement with the theoretical analysis.

At an excitation frequency $\nu_a = 7.6$ Hz, the particle motion is dominated by the first harmonics (Fig. 7). The particle motion almost fully follows the excitation frequency, and higher harmonics do not play a significant role. The experimental results are in excellent agreement with the theoretical prediction.

IV. CONCLUSION

The particle motion under the action of the pulsed ion beam is dominated by the excitation frequency and odd higher harmonics which peak near the resonance frequency. The appearance of even harmonics is explained by a variation of the particle's charge in dependence of its position in the plasma sheath.

REFERENCES

- [1] S. V. Vladimirov, K. Ostrikov, and A. A. Samarian, *Physics and Applications of Complex Plasmas*. London, U.K.: Imperial College Press, 2005.
- [2] M. S. Barnes, J. H. Keller, J. C. Forster, J. A. O'Neill, and D. K. Coultas, "Transport of dust particles in glow-discharge plasmas," *Phys. Rev. Lett.*, vol. 68, no. 3, pp. 313–316, Jun. 1992.

- [3] E. B. Tomme, D. A. Law, B. M. Annaratone, and J. E. Allen, "Parabolic plasma sheath potentials and their implications for the charge on levitated dust particles," *Phys. Rev. Lett.*, vol. 85, no. 12, pp. 2518–2521, Sep. 2000.
- [4] A. Melzer and J. Goree, "Fundamentals of dusty plasmas," in *Low Temperature Plasmas*, R. Hippler, H. Kersten, M. Schmidt, and K. H. Schoenbach, Eds. Berlin, Germany: Wiley-VCH, 2008, p. 129.
- [5] R. Hippler and H. Kersten, "Applications of dusty plasmas," in *Low Temperature Plasmas*, R. Hippler, H. Kersten, M. Schmidt, and K. H. Schoenbach, Eds. Berlin, Germany: Wiley-VCH, 2008, p. 787.
- [6] A. Bouchoule, Ed., *Dusty Plasmas*. New York: Wiley, 1999, p. 27.
- [7] H. Kersten, R. Wiese, H. Neumann, and R. Hippler, "Interaction of ion beams with dusty plasmas," *Plasma Phys. Control. Fusion*, vol. 48, no. 12B, pp. B105–B113, Nov. 2006.
- [8] E. B. Tomme, B. M. Annaratone, and J. E. Allen, "Damped dust oscillations as a plasma sheath diagnostic," *Plasma Sources Sci. Technol.*, vol. 9, no. 2, pp. 87–96, May 2000.



Ruben Wiese received the master degree from the Technical University Chemnitz, Chemnitz, Germany, in 1974 and the Ph.D. degree from the Ernst-Moritz-Arndt-Universität Greifswald, Greifswald, Germany, in 2007.

Since 2003, he has been a Research Scientist with the Leibniz Institute for Plasma Technology and Research, Greifswald, Germany. His research interests include plasma diagnostics and technological applications of plasmas.



Vladimir Sushkov received the master degree in physics from St. Petersburg State University, St. Petersburg, Russia, in 2003.

Since 2005, he has been a Scientific Researcher with the Ernst-Moritz-Arndt-Universität Greifswald, Greifswald, Germany. His research interests include plasma spectroscopy, plasma chemical reactions, and complex (dusty) plasmas.



Holger Kersten received the Ph.D. degree from the Ernst-Moritz-Arndt-Universität Greifswald, Greifswald, Germany, in 1990.

In 1996 and 1997, he was a Postdoctoral Researcher with the University of Eindhoven, Eindhoven, The Netherlands. From 2003 to 2006, he was the Head of the Department for Plasma Process Technology, Institute for Low-Temperature Plasma Physics (INP), Greifswald, Germany. Since 2006, he has been a Professor with the Christian-Albrechts-Universität zu Kiel, Kiel, Germany. His research

interests include plasma-surface interaction for technological applications, plasma diagnostics, and complex (dusty) plasmas.



Rainer Hippler received the Ph.D. degree from the Justus-Liebig-Universität Gießen, Gießen, Germany, in 1973.

In 1975, he became a Research Associate with the Universität Bielefeld, Bielefeld, Germany. In 1984 and 1985, he was a Research Scientist with Oak Ridge National Laboratory. In 1992–1994, he was a Visiting Research Associate with the University of Western Australia, Perth, Australia. Since 1995, he has been a Full Professor in experimental physics with the Ernst-Moritz-Arndt-Universität Greifswald, Greifswald, Germany. His research interests include electronic and atomic collision processes, plasma-surface interactions, thin-film deposition, plasma chemistry, complex (dusty) plasmas, and space weather.

Bibliography

- [1] F.M. Penning. Die glimmentladung bei niedrigem druck zwischen koaxialen zylindern in einem axialen magnetfeld. *Physica*, 3(9):873 – 894, 1936.
- [2] F.M. Penning. 1939. U.S. Patent 2146025: 'COATING BY CATHODE DISINTEGRATION (OCR)'.
- [3] P. A. Redhead. The townsend discharge in a coaxial diode with axial magnetic field. *Can J Phys*, 36(3):255–270, 1958. Wn208 Times Cited:80 Cited References Count:10.
- [4] R. L. Jepsen. Magnetically confined cold-cathode gas discharges at low pressures. *Journal of Applied Physics*, 32(12):2619–2626, 1961.
- [5] Eric Kay. Magnetic field effects on an abnormal truncated glow discharge and their relation to sputtered thin-film growth. *Journal of Applied Physics*, 34(4):760–768, 1963.
- [6] W. D. Gill and Eric Kay. Efficient low pressure sputtering in a large inverted magnetron suitable for film synthesis. *Review of Scientific Instruments*, 36(3):277–282, 1965.
- [7] Kiyotaka Wasa and Shigeru Hayakawa. Low pressure sputtering system of the magnetron type. *Review of Scientific Instruments*, 40(5):693–697, 1969.
- [8] W.D. Westwood. Glow discharge sputtering. *Progress in Surface Science*, 7(2):71 – 111, 1976.
- [9] John A. Thornton. Influence of apparatus geometry and deposition conditions on the structure and topography of thick sputtered coatings. *Journal of Vacuum Science and Technology*, 11(4):666–670, 1974.
- [10] John A. Thornton. Magnetron sputtering: basic physics and application to cylindrical magnetrons. *Journal of Vacuum Science and Technology*, 15(2):171–177, 1978.
- [11] J. S. Chapin. The planar magnetron. *Research Development*, 25(1):37–40, 1974.

- [12] P. S. McLeod and L. D. Hartsough. High-rate sputtering of aluminum for metallization of integrated circuits. *Journal of Vacuum Science and Technology*, 14(1):263–265, 1977.
- [13] Robert K. Waits. Planar magnetron sputtering. *Journal of Vacuum Science and Technology*, 15(2):179–187, 1978.
- [14] B. Window and N. Savvides. Charged particle fluxes from planar magnetron sputtering sources. *Journal of Vacuum Science Technology A: Vacuum, Surfaces, and Films*, 4(2):196–202, 1986.
- [15] B. Window and N. Savvides. Unbalanced dc magnetrons as sources of high ion fluxes. *Journal of Vacuum Science Technology A: Vacuum, Surfaces, and Films*, 4(3):453–456, 1986.
- [16] N. Savvides and B. Window. Unbalanced magnetron ion-assisted deposition and property modification of thin films. *Journal of Vacuum Science Technology A: Vacuum, Surfaces, and Films*, 4(3):504–508, 1986.
- [17] P. J. Kelly and J. W. Bradley. Pulsed magnetron sputtering - process overview and applications. *J Optoelectron Adv M*, 11(9):1101–1107, 2009.
- [18] J. T. Gudmundsson, N. Brenning, D. Lundin, and U. Helmersson. High power impulse magnetron sputtering discharge. *Journal of Vacuum Science and Technology A: Vacuum, Surfaces, and Films*, 30(3):030801, 2012.
- [19] Vladimir Kouznetsov, Karol Mack, Jochen M. Schneider, Ulf Helmersson, and Ivan Petrov. A novel pulsed magnetron sputter technique utilizing very high target power densities. *Surface and Coatings Technology*, 122(23):290 – 293, 1999.
- [20] J. K. Robertson and C. W. Clapp. Removal of metallic deposits by high-frequency currents. *Nature*, 132(334):479 – 480, 1933.
- [21] R. H. Hay. The removal of wall deposits by high frequency discharges. *Canadian Journal of Research*, 16a(10):191–205, 1938.
- [22] J. I. Lodge and R. W. Stewart. Studies in high frequency discharges. *Canadian Journal of Research*, 26a(4):205–229, 1948.
- [23] G. K. Wehner. Sputtering by ion bombardment. *Adv. Electron. Electron Phys.*, VII:239 – 298, 1955.
- [24] P. A. Sturrock. Microwave laboratory report no. 638; w.w. hansen laboratories of physics, stanford university, stanford, california, usa. 1958.
- [25] G. S. Anderson, Wm. N. Mayer, and G. K. Wehner. Sputtering of dielectrics by high-frequency fields. *Journal of Applied Physics*, 33(10):2991–2992, 1962.

- [26] H. S. Butler and G. S. Kino. Plasma sheath formation by radio-frequency fields. *Physics of Fluids*, 6(9):1346–1355, 1963.
- [27] Jr. P. J. Hargis, K. E. Greenberg, P. A. Miller, J. B. Gerardo, J. R. Torczynski, M. E. Riley, G. A. Hebner, J. R. Roberts, J. K. Olthoff, J. R. Whetstone, R. J. Van Brunt, M. A. Sobolewski, H. M. Anderson, M. P. Splichal, J. L. Mock, P. Bletzinger, A. Garscadden, R. A. Gottscho, G. Selwyn, M. Dalvie, J. E. Heidenreich, Jeffery W. Butterbaugh, M. L. Brake, M. L. Passow, J. Pender, A. Lujan, M. E. Elta, D. B. Graves, H. H. Sawin, M. J. Kushner, J. T. Verdeyen, R. Horwath, and T. R. Turner. The gaseous electronics conference radio-frequency reference cell: A defined parallel-plate radio-frequency system for experimental and theoretical studies of plasma-processing discharges. *Review of Scientific Instruments*, 65(1):140–154, 1994.
- [28] Michael R. Winchester and Richard Payling. Radio-frequency glow discharge spectrometry:: A critical review. *Spectrochimica Acta Part B: Atomic Spectroscopy*, 59(5):607 – 666, 2004.
- [29] M. A. Lieberman and A. J. Lichtenberg. *Principles of Plasma Discharges and Material Processing*. JOHN WILEY & SONS, INC., 1994.
- [30] V Sushkov, H T Do, M Čada, Z Hubička, and R Hippler. Time-resolved tunable diode laser absorption spectroscopy of excited argon and ground-state titanium atoms in pulsed magnetron discharges. *Plasma Sources Science and Technology*, 22(1):1–10, 2013.
- [31] C.K. Goertz and G. Morfill. A model for the formation of spokes in saturn’s ring. *Icarus*, 53(2):219 – 229, 1983.
- [32] Kenneth G. Spears, Timothy J. Robinson, and Richard M. Roth. Particle distributions and laser-particle interactions in an rf discharge of silane. *Plasma Science, IEEE Transactions on*, 14(2):179–187, 1986.
- [33] G. S. Selwyn, J. Singh, and R. S. Bennett. Insitu laser diagnostic studies of plasma-generated particulate contamination. *Journal of Vacuum Science and Technology A*, 7(4), 1989.
- [34] H. Thomas, G. E. Morfill, V. Demmel, J. Goree, B. Feuerbacher, and D. Möhlmann. Plasma crystal: Coulomb crystallization in a dusty plasma. *Phys. Rev. Lett.*, 73:652–655, Aug 1994.
- [35] P. K. Shukla and B. Eliasson. *Colloquium* : Fundamentals of dust-plasma interactions. *Rev. Mod. Phys.*, 81:25–44, Jan 2009.
- [36] K Tachibana, H Harima, and Y Urano. Measurements of collisional broadening and the shift of argon spectral lines using a tunable diode laser. *Journal of Physics B: Atomic and Molecular Physics*, 15(18):3169, 1982.

- [37] Annemie Bogaerts, Renaat Gijbels, and Jaroslav Vlcek. Collisional-radiative model for an argon glow discharge. *Journal of Applied Physics*, 84(1):121–136, 1998.
- [38] K. Bartschat and V. Zeman. Electron-impact excitation from the $(3p^5 4s)$ metastable states of argon. *Phys. Rev. A*, 59:R2552–R2554, Apr 1999.
- [39] M A Khakoo, P Vandeventer, J G Childers, I Kanik, C J Fontes, K Bartschat, V Zeman, D H Madison, S Saxena, R Srivastava, and A D Stauffer. Electron impact excitation of the argon $3p^5 4s$ configuration: differential cross-sections and cross-section ratios. *Journal of Physics B: Atomic, Molecular and Optical Physics*, 37(1):247, 2004.
- [40] M. Asgar Ali and P.M. Stone. Electron impact ionization of metastable rare gases: He, ne and ar. *International Journal of Mass Spectrometry*, 271(13):51 – 57, 2008.
- [41] N B Kolokolov and A B Blagoev. Ionization and quenching of excited atoms with the production of fast electrons. *Physics-Usp ekhi*, 36(3):152, 1993.
- [42] L. A. Riseberg, W. F. Parks, and L. D. Schearer. Penning ionization of zn and cd by noble-gas metastable atoms. *Phys. Rev. A*, 8:1962–1968, Oct 1973.
- [43] J. Hopwood and F. Qian. Mechanisms for highly ionized magnetron sputtering. *Journal of Applied Physics*, 78(2):758–765, 1995.
- [44] H. A. Hyman. Electron-impact excitation of metastable argon and krypton. *Phys. Rev. A*, 18:441–446, Aug 1978.
- [45] L M Biberman, V S Vorobjev, and Yakubov I T. *Kinetics of Nonequilibrium Low-temperature Plasmas*. Plenum, New York, 1987.
- [46] T. C. Killian, M. J. Lim, S. Kulin, R. Dumke, S. D. Bergeson, and S. L. Rolston. Formation of rydberg atoms in an expanding ultracold neutral plasma. *Phys. Rev. Lett.*, 86:3759–3762, Apr 2001.
- [47] Yusuf Celik, Tsanko V. Tsankov, Mitsutoshi Aramaki, Shinji Yoshimura, Dirk Luggenhölscher, and Uwe Czarnetzki. Recombination and enhanced metastable repopulation in the argon afterglow. *Phys. Rev. E*, 85:056401, May 2012.
- [48] Karla Börnig. Modeling a collisional, capacitive sheath for surface modification applications in radio-frequency discharges. *Applied Physics Letters*, 60(13):1553–1555, 1992.
- [49] A V Phelps and Z Lj Petrovic. Cold-cathode discharges and breakdown in argon: surface and gas phase production of secondary electrons. *Plasma Sources Science and Technology*, 8(3):R21, 1999.

- [50] Martin Čada, Zdeněk Hubička, Petr Adámek, Jan Klusoň, and Lubomír Jastrabík. Time-resolved plasma parameters in the hipims discharge with ti target in ar/o₂ atmosphere. *Surface and Coatings Technology*, 205, Supplement 2(0):317 – 321, 2011.
- [51] J. T. Gudmundsson, P. Sigurjonsson, P. Larsson, D. Lundin, and U. Helmersson. On the electron energy in the high power impulse magnetron sputtering discharge. *Journal of Applied Physics*, 105(12):123302, 2009.
- [52] P.J. Linstrom and W.G. Mallard(Eds.). *NIST Chemistry WebBook, NIST Standard Reference Database Number 69*. National Institute of Standards and Technology, Gaithersburg MD, 20899, <http://webbook.nist.gov>, (retrieved June 6, 2013).
- [53] E. B. Tomme, D. A. Law, B. M. Annaratone, and J. E. Allen. Parabolic plasma sheath potentials and their implications for the charge on levitated dust particles. *Phys. Rev. Lett.*, 85:2518–2521, Sep 2000.

Summary

The thesis describes experimental results based on optical diagnostics of low-pressure discharges. Further, models are developed and simulations are done which are necessary for the interpretation of the experimental data.

Three types of optical diagnostics are used in the thesis: (i) absorption spectroscopy, (ii) optical emission spectroscopy and (iii) fast video recording. The low-pressure discharges were of (a) pulsed magnetron and (b) capacitively coupled radio frequency (rf) types. Specifically, the thesis considers three experimental realizations:

1. Tunable diode laser absorption spectroscopy of a pulsed magnetron discharge
2. Optical emission- and laser absorption spectroscopy of a rf discharge
3. fast video recording of a rf discharge.

1. The densities and temperatures of the metastable and resonance states of argon, and the ground state of titanium have been determined by time-resolved laser absorption spectroscopy in pulsed magnetron discharges with a Ti target [V. Sushkov et al., PSST 22 (2013)]. The temporal behavior of the densities and temperatures within the active phase and during the afterglow is explained on the basis of numerous processes involving inelastic collisions with electrons. Further, the much longer afterglow of *high power impuls magnetron* enables such processes like three-body recombination and diffusion to manifest themselves. This was shown by solving the non-stationary balance equations for the afterglow, which reproduce the time-course of the densities, including the "recombination peak".

2. A recent technique based on OES data employs the self-absorption phenomenon and utilizes the concept of the *escape factor* [Sushkov et al., CPP 53, (2013)]. The measurements were done in an argon rf discharge for the densities of the four lowest-lying metastable and resonance states. The problem of the spatial profile assumed for the excited species have been treated analytically and simple expressions for the escape factor have been obtained for the case of a Gaussian lineshape. The range of applicability of the expressions have been discussed from theoretical and experimental perspectives. These results have been benchmarked by the TDLAS measurements.

3. The behavior of a relatively large (comparable to the Debye length) particle in the sheath of an rf discharge was registered by a fast camera [R. Wiese, V. Sushkov et al., New J. Phys. 12 (2010); R. Wiese, V. Sushkov et al., IEEE Trans. Plasma Sci. 38 (2010)]. The particle's oscillation was driven by two different influences - the periodic action of an ion source and the quasi-harmonic restoring force about an equilibrium position. Fourier-analysis of the particle's trace combined with a sheath model yielded comprehensive information on particle's charge and its variation due to oscillations and ion bombardment. It was shown that the particle's charge was anomalously large apparently due to its porous structure. This study pertains to the field of complex plasmas.

Erklärung

Prozentualer Arbeitsanteil an der Publikationen:

- **Article I** - V Sushkov, H T Do, M Cada, Z Hubicka and R Hippler

Time-resolved tunable diode laser absorption spectroscopy of excited argon and ground-state titanium atoms in pulsed magnetron discharges

Plasma Sources Sci. Technol. **22** (2013) 015002

40%

- **Article II** - V. P. Sushkov, H. T. Do, and R. Hippler

Application of the escape factor method for determination of excited states densities in a low-pressure argon radio-frequency discharge

Contrib. Plasma Phys. **53**(7), 549 (2013)

70%

- **Article III** - Ruben Wiese, Vladimir Sushkov, Holger Kersten, and Rainer Hippler

Fourier Analysis of Particle Motion in a Radio Frequency Plasma Under Pulsed Argon Ion Beam Bombardment

IEEE Transac. on Plasma Sci. **38**(4), 810 (2010)

35%

- **Article IV** - Ruben Wiese, Vladimir Sushkov, Holger Kersten, Venkata R Ikkurthi, Ralf Schneider and Rainer Hippler

Behavior of a porous particle in a radiofrequency plasma under pulsed argon ion beam bombardment

New J. Phys. **12**, 033036 (2010)

25%

Obige Angaben werden bestätigt:

Greifswald, den 19.12.2013

Unterschrift des Betreuers der Dissertation

Unterschrift des Promovierenden

Selbständigkeitserklärung

Hiermit erkläre ich, dass diese Arbeit bisher von mir weder an der Mathematisch-Naturwissenschaftlichen Fakultät der Ernst-Moritz-Arndt-Universität Greifswald noch einer anderen wissenschaftlichen Einrichtung zum Zwecke der Promotion eingereicht wurde.

Ferner erkläre ich, dass ich diese Arbeit selbständig verfasst und keine anderen als die darin angegebenen Hilfsmittel und Hilfen benutzt und keine Textabschnitte eines Dritten ohne Kennzeichnung übernommen habe.

Greifswald, den 19.12.2013

Vladimir Sushkov

LEBENS LAUF

(gekürzt)

VLADIMIR SUSHKOV

PERSÖNLICHE DATEN

Name: Sushkov

Vorname: Vladimir

Geboren: in St. Petersburg (Russland)

AKADEMISCHER WERDEGANG

1996–2005 Physikalische Fakultät, Lehrstuhl für Optik,
Staatliche Universität St. Petersburg.

1996–2000 **Bachelorstudium.**

2000–2003 **Masterstudium.**

2005–2013 Mathematisch-Naturwissenschaftliche Fakultät,
Institut für Physik, EMAU Greifswald.

Wissenschaftlicher Mitarbeiter,

Promotionstudium.

Spezialisierung: Plasma Physik, Optik, Modellierung and
Simulierung.

Publications

My publications

- H.C. Thejaswini, Sandra Peglow, Ulrike Martens, Vladimir Sushkov, and Rainer Hippler *Comparative Plasma Chemical Reaction Studies of CH_4/Ar and $\text{C}_2\text{H}_m/\text{Ar}$ ($m=2,4,6$) Gas Mixtures in a Dielectric Barrier Discharge* Contrib. Plasma Phys. **54**, DOI 10.1002/ctpp.201300035 *in print* (2014)
- V. P. Sushkov, H. T. Do, and R. Hippler *Application of the escape factor method for determination of excited states densities in a low-pressure argon radio-frequency discharge* Contrib. Plasma Phys. **53**(7), 549 (2013)
- V Sushkov, H T Do, M Cada, Z Hubicka and R Hippler *Time-resolved tunable diode laser absorption spectroscopy of excited argon and ground-state titanium atoms in pulsed magnetron discharges* Plasma Sources Sci. Technol. **22**, 015002 (2013)
- Ruben Wiese, Vladimir Sushkov, Holger Kersten, and Rainer Hippler *Fourier Analysis of Particle Motion in a Radio Frequency Plasma Under Pulsed Argon Ion Beam Bombardment* IEEE Transaction on Plasma Science **38**(4), 810 (2010)
- Ruben Wiese, Vladimir Sushkov, Holger Kersten, Venkata R Ikkurthi, Ralf Schneider and Rainer Hippler *Behavior of a porous particle in a radiofrequency plasma under pulsed argon ion beam bombardment* New J. Phys. **12**, 033036 (2010)
- Hoang Tung Do, Vladimir Sushkov and Rainer Hippler *Tunable diode laser absorption spectroscopy of argon metastable atoms in $\text{Ar}/\text{C}_2\text{H}_2$ dusty plasmas* New J. Phys. **11**, 033020 (2009)
- Yu B Golubovskii, I A Porokhova, V P Sushkov, M Holík, P Kudrna and M Tichý *Electron kinetics in cylindrical discharges of magnetron congurations* Plasma Sources Sci. Technol. **15**, 228 (2006)
- Yu B Golubovskii, H Lange, V A Maiorov, I A Porokhova and V P Sushkov *On the decay of metastable and resonance Xe atoms in the afterglow of a constricted discharge* J. Phys. D: Appl. Phys. **36**, 694 (2003)

Contributions

POSTERS

- Hoang Tung Do, Martin Cada, Vladimir Sushkov, Zdenek Hubicka, and Rainer Hippler, *Time resolved laser absorption spectroscopy for Ar* density and temperature in pulsed magnetron discharge*. DPG Frhjahrstagung, 28th - 31st of March 2011, Kiel, Germany.
- Vladimir Sushkov, Hoang Tung Do, and Rainer Hippler, *Determination of argon metastable and resonant state densities from emission spectrum*. DPG Frhjahrstagung, 28th - 31st of March 2011, Kiel, Germany.
- Vladimir Sushkov, Hoang Tung Do, and Rainer Hippler, *Radiation trapping and the measurement of metastable density by optical emission spectroscopy*. DPG Frhjahrstagung, 8th - 12th of March 2010, Hannover, Germany.
- Vladimir Sushkov, Mario Hannemann, Jürgen Röpcke and Rainer Hippler, *Hydrocarbon consumption in a radiofrequency discharge investigated by means of tuneable Infrared diode laser absorption spectroscopy*. 1st International Workshop on Infrared Plasma Spectroscopy, 14th - 16th of June 2006, Greifswald, Germany
- Yu. B. Golubovskii, I. A. Porokhova, V. P. Sushkov, M. Holík, P. Kudrna, and M.Tichý, *Comparison of the EDFs and macroscopic properties in the cylindrical magnetron discharges of direct and inverted designs*. 17th International Symposium on Plasma Chemistry (ISPC), 7th - 12th of August 2005, Toronto, Canada
- Yu. B. Golubovskii, I. A. Porokhova, V. P. Sushkov, M. Holík, P. Kudrna, and M.Tichý, *Effect of ionization models on the EDF in cylindrical magnetron discharges of direct and inverted designs*. XXVIIth International Conference on Phenomena in Ionized Gases (ICPIG), 18th - 22th of July 2005, Eindhoven, the Netherlands.
- Yu. B. Golubovskii, H. Lange, V. A. Maiorov, I. A. Porokhova and V. P. Sushkov, *On the decay of metastable and resonance Xe atoms in the afterglow of a constricted discharg*. XXVIth ICPIG, 15th - 20th of July 2003, Greifswald, Germany

TALKS

- Vladimir Sushkov *Optical emission and absorption spectroscopy of excited argon atoms in a rf discharge*, Lecture at the 2nd Graduate Summer institute "Complex Plasmas", 4th - 13th of August 2010, Greifswald, Germany.
- V. P. Sushkov, H. T. Do, and R. Hippler, *Radiation trapping and the measurement of metastable density by optical emission spectroscopy*. XVIII International Conference on Gas Discharges and Their Applications, 5th - 10th September 2010, Greifswald, Germany.
- Vladimir Sushkov, Ruben Wiese, Holger Kersten, and Rainer Hippler, *Oscillation of a big particle driven by an ion beam in RF plasma sheath*. Workshop, 2th - 4th of September 2009, Kiel, Germany.
- Vladimir Sushkov, Ruben Wiese, Holger Kersten, and Rainer Hippler, *Oscillation of a big particle in a rf sheath*. SFB TR6 Young researcher Workshop, 18th - 19th of September 2008, Mainz, Germany.

Acknowledgements

First of all, it's my pleasure to express sincere gratitude to Prof. Dr. Rainer Hippler for the possibility to write a Ph.D. work in his group, for his valuable hints and advices, and for his understanding in a broad sense.

I also express my thanks to Dr. Hoang Tung Do for the time of our collaborative work full of fruitful research and exciting communication.

The technical support from Axel Knuth and Robert Mrotzek was also welcome.

I appreciated a lot the atmosphere in the working group, which was somewhat eclectic, unique and enjoyable. I give my thanks to all the permanent and temporary members of the group, and at this point I want to name especially Ann-Pierra H., Steffen D., Angelin E. J., Vasile V., Vit S., Robert B..

And of course my warmest gratitude is addressed to my parents, who wanted this thesis to be done probably no less than me myself.

My work was supported by the Deutsche Forschungsgemeinschaft (DFG) through Sonderforschungsbereich SFB/TR24 „ComplexPlasmas“.